Film Thickness Measurements in Falling Annular Films

A Thesis

Submitted to the College of Graduate Studies and Research in

Partial Fulfilment of the Requirements

for the degree of

Master of Science

in the

Department of Mechanical Engineering

University of Saskatchewan

Saskatoon

By

Anand Padmanaban

Permission to use

In presenting this thesis in partial fulfilment of the requirements for a post-graduate degree from the University of Saskatchewan, I agree that the libraries of this University may make it freely available for inspection. I further agree that permission for copying of the thesis in any manner, in whole or in part, for scholarly purposes may be granted by Professor J.D. Bugg or, in his absence, by the Head of the Department of Mechanical Engineering or the Dean of the College of Engineering. It is understood that any copying or publication or use of this thesis or parts thereof for financial gain shall not be allowed without my permission. It is also understood that due recognition shall be given to me and to the University of Saskatchewan in any scholarly use which may be made of any material in my thesis.

Requests for permission to copy or make any other use of material in this thesis in whole or in part should be addressed to:

Head of Department of Mechanical Engineering
57 Campus Drive
University of Saskatchewan
Saskatoon, Saskatchewan, Canada
S7N 5A9

Acknowledgements

I would like to express my sincere thanks and appreciation to my supervisor, Dr. J. D. Bugg. I would like to thank him for his thoughtful insights, guidance, support, and understanding throughout my Master's program and thesis preparation. I would like to thank my advisory committee members, Dr. D. Sumner and Dr. D. Torvi, for their useful suggestions. My special thanks to Mr. Dave Deutscher for his technical support and assistance in the Experimental Fluid Mechanics laboratory. My appreciation also goes to Mr. Henry Berg and Mr. Keith Palibroda of the Engineering Shops for their design support.

It is my pleasure to acknowledge the encouragement and constant support received from my parents and my brother who helped me in many ways to make this program a success. I would also like to thank my fellow colleagues and friends at the University for their motivation and moral support.

Finally, this acknowledgement would be incomplete without thanking God for his abundant grace in my life.

Abstract

Liquid films falling under the influence of gravity are widely encountered in a variety of industrial two-phase flow applications (distillation columns, nuclear reactor cores, etc.). In addition, the falling annular film represents a fundamental limiting case of the annular flow regime of two-phase gas-liquid flows. The literature on annular falling films is dominated by studies concerning the average film thickness. Information on more detailed characteristics of the film thickness variations and information on the velocity profile within the film and wall shear stress are much less common. The statistical description of the film thickness is complicated by the fact that practically all flows of interest occur in the turbulent regime. Due to the complex and unsteady nature of the turbulent annular falling film, no complete theories or models have yet been developed on the subject. Experimental studies are needed to gain insight into the basic mechanisms that govern this complex flow.

The primary purpose of this thesis research was to characterise the film thickness of falling annular films at high and very high Reynolds numbers using non-intrusive imaging techniques. Another objective was to develop ray-tracing techniques to reduce optical distortion and obtain high-quality experimental data.

Instantaneous film thickness measurements of falling annular films were extracted at five different Reynolds numbers in the range Re = 1000 ~ 6000 for the fully developed turbulent regime using an automated optical measurement technique. From visual observation of the images obtained it was found that waves were not axisymmetric, i.e., there was substantial azimuthal variation in film thickness. The turbulent waves appeared to be similar in appearance to very large breaking ocean waves driven by strong winds. The random nature of these falling annular films was subjected to statistical analysis.

Statistical characteristics of film thickness were studied at Reynolds numbers in the range Re = 1000 ~ 6000. A correlation for dimensionless mean film thickness $\overline{\delta}^{+}$ was

obtained in the turbulent flow regime. The dimensionless mean film thickness $\overline{\delta}^{+}$ obtained here was found to be in reasonable agreement with the other established experimental and theoretical studies. It was shown that the Reynolds number *Re* influences the statistical characteristics of film thickness such as standard deviation *s* and coefficient of variation $s/\overline{\delta}$. The additional data obtained here shows that the standard deviation continues to increase in proportion to the mean film thickness in the turbulent regime. In other words, in the lower turbulent zones the films are thin and less wavy, whereas in the higher turbulent zones the films are thicker and extremely wavy in nature.

The probability density distributions $P(\delta)$ were also obtained. It was found that the measured probability density distributions $P(\delta)$ were asymmetric. They all had a maximum peak and were skewed to the right hand side with a long tail that stretched to over six times the peak value. The maximum peak could be considered to represent the modal value of the film thickness or the substrate film thickness. The increase in skewness and the decrease in the height of the peak with liquid Reynolds number could be attributed to the presence of large disturbance waves which ride on the substrate film. This enhances the waviness of the film.

A common problem in imaging flows in cylindrical tubes is the optical distortion caused by the wall curvature. To minimise this problem the cylindrical tube was surrounded by an optical correction box with flat walls filled with water. In addition, an advanced ray tracing model was employed to reduce optical distortion effects in the cylindrical tube. This technique increased the accuracy of the imaging technique and enabled quantitative measurements of film thickness to be made.

Table of Contents

List of Figures

List of Tables

Nomenclature

English symbols:

D	diameter of the vertical tube (m)
f	f-stop
g	acceleration due to gravity (m/s^2)
H_i	height of object in the image plane (pixels)
L_a	distance between optical correction box and pin hole (mm)
L_i	distance between pinhole and image plane (mm)
L_w	distance between outside of tube and optical correction box (mm)
m	slope of a line
$\dot{m}_\mathrm{l}$	liquid film mass flow rate (kg/s)
N	total the number of measurements
n	refractive index of a medium
P	probability density function
p	pressure (Pa)
Q	volume flow rate (m^3/s)
R_0	outer tube radius (mm)
R_w	internal tube or wall radius (mm)
Re	Reynolds number
r_i	radius of the gas-liquid interface (mm)
r, θ, z	cylindrical coordinates
s	standard deviation in film thickness (mm)
s^2	variance in film thickness (mm^2)
T	time (s)
t_c	calculated *t* for t-test
t_t	tabulated *t* from t-chart
u_l	superficial liquid velocity (m/s)
u_z	liquid film velocity (m/s)

u^*	friction velocity (m/s)
W	thickness of the optical correction box wall (mm)
z	longitudinal distance from liquid inlet (m)

Greek symbols:

α	angle between a ray and normal to a surface (degrees)
β	contact angle (degrees)
$\delta(T)$	instantaneous film thickness at observation time T (mm)
$\overline{\delta}$	mean film thickness (mm)
$\overline{\delta}^+ = u^*\delta_i/\upsilon$	dimensionless mean film thickness
$\overline{\delta'}$	substrate film thickness (mm)
μ	dynamic viscosity (kg/ms)
ν	kinematic viscosity (cS)
ρ	density (kg/m^3)
σ	surface tension (N/m)
τ_w	wall shear stress (kg/ms^2)

Abbreviations:

A	air
Ac	acrylic
LCD	Liquid Crystal Display
LDA	laser Doppler anemometer
LDV	laser Doppler velocimetry
r.m.s	root-mean-square
S	point source
SLR	Single Lens Reflex
TTL	through-the-lens
W	water

CHAPTER 1
INTRODUCTION

1.1 General

Thin liquid films falling under the influence of gravity are widely encountered in a variety of industrial applications that involve gas-liquid two-phase flow. Flow in nuclear reactor cores, steam condensers, water tube boilers, cooling towers, distillation columns, and vertical tube evaporators are some of the practical examples of this flow configuration. In order to design these systems with greater efficiency and lower cost, a basic understanding of the physical processes occurring in falling films is needed.

1.2 Background

In this section, the basic flow patterns observed in vertical gas-liquid two-phase flows will be briefly discussed. Following this, the special case of falling annular films will be introduced. Also, the significance of Reynolds number in film flow will be considered here.

1.2.1 Flow patterns in vertical gas-liquid two phase flows

A flow regime is a geometrical configuration taken up by the gas and liquid in a two-phase flow. For conditions of technological interest, there are a few major types of flow regimes observed for gas-liquid flow in pipes. Characteristics of these flow regimes, and the conditions under which these flow patterns exist, depend on (among other things) the orientation of the pipe with respect to gravity. Usually the transitions between regimes are not distinct and this leads to variability in the

literature regarding the regime boundaries and regime names. Figure 1.1 shows the flow patterns that are observed in vertical downward gas-liquid flows.

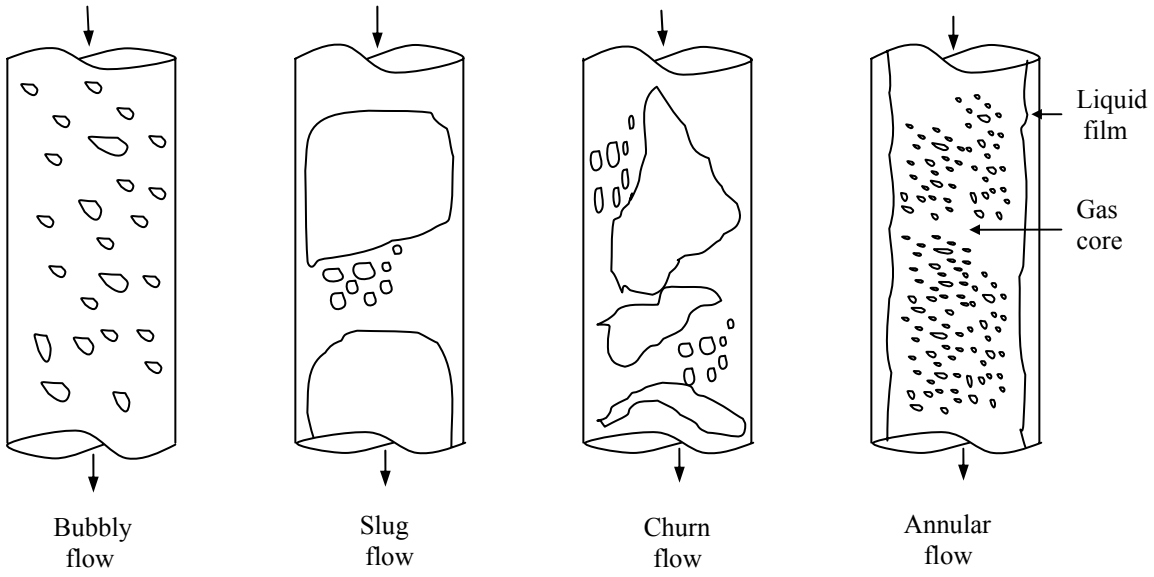

Figure 1.1: Flow patterns observed in vertical downward two phase flow regimes

At low gas flow rates a bubbly flow pattern, in which small gas bubbles spherical or nearly spherical in nature are uniformly distributed in the liquid, is obtained. Increasing the gas flow rate leads to slug flow. This flow pattern is characterised by large bullet-shaped gas bubbles separated by liquid slugs filling the entire cross-section of the tube. At even higher gas flow rates, a highly agitated churn flow is observed. It could be viewed as a transition between slug and annular flows. This flow regime is usually very small or absent in vertical downward flows. Increasing the gas flow rate further leads to the annular flow regime in which the liquid moves along the pipe wall as a thin, wavy film and the gas flows in the core region as shown in figure 1.1. Here, most of the liquid is present in the film and the liquid film may or may not contain gas bubbles. Also, the gas core may or may not contain entrained liquid droplets. This flow pattern is very important in two-phase heat transfer applications because it immediately precedes the “dry out condition” where there is breakdown of the liquid film on the wall.

The falling annular film represents a fundamental limiting case of the annular flow regime of two-phase gas-liquid flows. The liquid film descends on the walls and there is no net flow of gas in the pipe. This means that the gas core is a constant pressure region. As for other flows, falling films can be broadly classified into laminar and turbulent film flows. The most important flow, which is of greater practical interest, is the turbulent film flow where there are random fluctuations in the velocity field. The flow is more complicated due to the presence of waves on the gas-liquid interface and is considered to be unsteady and non-uniform. The presence of waves enhances the macroscopic transport properties of the system. As a consequence, simple energy transfer rate equations fail to describe the flow process accurately.

A dimensional analysis of film flow has shown the Reynolds number to be important. The Reynolds number (*Re*) used in this thesis is defined as follows (note that in the present case, the superficial gas velocity is zero),

$$Re = \frac{\rho u_l D}{4\mu} = \frac{\dot{m}_l}{\pi D \mu} \ . \qquad (1.1)$$

where ρ is the density (kg/m^3), μ is the liquid dynamic viscosity (kg/ms), u_l is the superficial liquid velocity (m/s), D is the diameter of the vertical tube (m), and $\dot{m}_l$ is the liquid mass flow rate (kg/s). The superficial liquid velocity is the velocity that the liquid would have if it flowed through the total cross-sectional area available for the flow. Sometimes, a Reynolds number used by previous researchers in their studies was defined as follows

$$Re = \frac{\rho u_l D}{\mu} = \frac{4\dot{m}_l}{\pi D \mu} \ . \qquad (1.2)$$

All Reynolds numbers used in this thesis have been converted to be consistent with equation 1.1.

It is well known that below a certain critical value of Reynolds number the flow will be mainly laminar in nature, while above this value, turbulence plays an important role. The same is true for falling annular films. At all but the smallest of Reynolds

numbers (Re = 5), a liquid falling under the influence of gravity contains waves or ripples on the interface (Kapitza, 1965). Even at very low Reynolds numbers, the film is not smooth but the wave motion is periodic in character. The waves are widely spaced with long troughs between each large wave and with small waves of capillary size following the peaks. At somewhat higher flow rates, periodic motion exists only near the entry region of a vertical film. However, farther downstream the periodic motion is replaced with a greater frequency of large waves. The wave fronts of these large waves are steep followed by smaller waves which are no longer of capillary size. At the highest flow rates, the flow becomes very complex and random in nature. There are several reports in the literature of the critical Reynolds number at which turbulence commences in falling liquid films. These values are usually determined from discontinuities which appear in plots of film thickness, heat or mass transfer coefficients, etc., as the Reynolds number is increased. Several investigators have quoted a lower and upper critical value enclosing a transition region. Dukler and Bergelin (1952) and Zhivaikin and Volgin (1961) have pointed out that the transition to turbulence in a thin film is likely to be a gradual process, so that it is not reasonable to expect a single, sharply defined critical Reynolds number. Nevertheless, it is of value to subdivide film flow into laminar and turbulent regimes depending on whether the Reynolds number is greater or less than a critical Reynolds number. The bulk of the evidence seems to support a lower value of critical Reynolds number in the region 250-400, at which turbulence could be detected, and a less well-marked upper value of about 800, at which the flow became "fully turbulent" (Fulford, 1964). The turbulent regime is characterised by flows above a Reynolds number of 250 (Bird *et al*., 1960). Photographs presented by Dukler and Bergelin (1952) for the turbulent regime clearly show that no two waves are alike. On the basis of Dukler and Bergelin (1952) experimental data, the transition from laminar to turbulent film flow occurs at a Reynolds number of 270.

1.3 Motivation and objectives

1.3.1 Motivation

Falling liquid films are generally used due to their relatively high energy and mass transfer potentials at low liquid flow rates. A significant amount of research work both experimental and theoretical carried out over the last few decades suggests that the rates of momentum, heat and mass transfer are strongly influenced by the film thickness characteristics and especially the waviness of the gas-liquid interface. Although many attempts have been made in the past to describe the statistical characteristics of the film thickness in falling liquid films, and some of these results have been in good agreement with the available experimental observations, their applicability is restricted to small Reynolds numbers. A numerical simulation of the wavy film flow requires both the solution of the Navier-Stokes equations and the film shape, and is usually limited by the numerical instabilities arising from factors related to modelling the moving interface. As a result, convergence is difficult to obtain except at very low flow rates.

So, experimental investigations of the characteristics of falling annular films play a vital role in gaining a profound understanding of the nature of falling annular films. The major difficulty in measuring film thickness within falling liquid films is that the liquid films normally encountered are of the order of one millimetre thick. Some of the common film thickness measurement techniques used in the past, such as pressure probes, Pitot tubes, and hot-wire anemometers inevitably obstruct or disturb the films or suffer from limited spatial resolution, yielding somewhat inaccurate data. Most of the literature on annular falling films is dominated by studies concerning the average film thickness. Information on more detailed characteristics of the film thickness variations is much less common. The statistical description of the film thickness is complicated by the fact that practically all flows of interest occur in the turbulent flow regime.

1.3.2 Objectives

The objectives of this research are:

1. To use non-intrusive imaging techniques to extract quantitative instantaneous film thickness measurements in falling annular films. The measurement of instantaneous film thickness of the falling liquid film through flow visualisation studies might yield some information regarding the structure of turbulence which forms the basis for analysing the phenomena of heat and mass transfer in falling liquid films.
2. To employ a ray-tracing technique to reduce optical distortion effects in cylindrical tubes. Thus, quantitative measurements of film thickness will be made possible.
3. To characterise the film thickness of falling annular films at high and very high Reynolds numbers.

1.3.3 Scope

This research focuses on an experimental study of the characteristics of falling annular films using a non-intrusive imaging technique. The work was undertaken in a 4 m long vertical tube with an internal diameter of 25.48 mm at a Reynolds number ($Re = \rho u_l D / 4\mu$) in the range of 1000 to 6000 (where the characteristic velocity is the superficial liquid velocity, and the characteristic length is the diameter of the tube) for the fully-developed turbulent flow regime. The present research shows the highly localised film thickness measurements and also reveals some of the statistical and random characteristics of falling annular film flows at high and very high Reynolds numbers. Thus, the once formidable task of measuring the qualitative and quantitative instantaneous film thickness in falling liquid films at high and very high Reynolds numbers is no longer insurmountable.

1.4 General outline of thesis

The theoretical considerations for a smooth laminar film flow and a detailed literature review of falling liquid films are presented in Chapter 2. The apparatus,

instrumentation and measurement techniques employed in the present study are described in Chapter 3. The development of the ray tracing concepts along with image processing and extraction of quantitative measurements from two-dimensional images are also explained in more detail in the same chapter. In Chapter 4, some general qualitative observations and the results of the quantitative measurements of film thickness on falling annular films are presented. Also, a discussion of the statistical characteristics of the film thickness such as mean film thickness, standard deviation, coefficient of variation, and the probability density distribution is found in the same chapter. In Chapter 5, the conclusions and recommendations for future work are outlined. The Inspector® code written for the extraction of raw film thickness from the images is presented in Appendix A.

CHAPTER 2
LITERATURE REVIEW

2.1 Introduction

In this chapter, the Navier-Stokes equations are solved for a smooth laminar falling annular film flow. Also, the definitions of some of the important statistical characteristics such as the mean film thickness, standard deviation, and probability density distribution of film thickness are discussed briefly. The theoretical, modelling and experimental falling annular film literature are then reviewed in more detail. Finally, the turbulent film thickness correlations of previous researchers and some of the conditions used to obtain them are summarised briefly.

2.2 Theoretical considerations

2.2.1 General equations for smooth laminar film flow

Consider a liquid film of thickness δ flowing inside a vertical tube of internal radius R_w. The flow is assumed to be a steady, incompressible, fully developed, and laminar and flows in the z direction as shown in figure 2.1. It is driven by gravity and the pressure is assumed to be constant. The axial component of the Navier-Stokes equations in cylindrical coordinates is as follows:

$$\rho\left[\frac{\partial u_z}{\partial t} + u_r\frac{\partial u_z}{\partial r} + \frac{u_\theta}{r}\frac{\partial u_z}{\partial \theta} + u_z\frac{\partial u_z}{\partial z}\right] = -\frac{\partial p}{\partial z} + \rho g_z + \mu\left[\frac{1}{r}\frac{\partial}{\partial r}\left(r\frac{\partial u_z}{\partial r}\right) + \frac{1}{r^2}\frac{\partial^2 u_z}{\partial \theta^2} + \frac{\partial^2 u_z}{\partial z^2}\right] \tag{2.1}$$

In addition, the continuity equation is:

$$\frac{1}{r}\frac{\partial}{\partial r}(ru_r)+\frac{1}{r}\frac{\partial}{\partial \theta}(u_\theta)+\frac{\partial}{\partial z}(u_z)=0 \quad . \tag{2.2}$$

By assuming axisymmetric flow in the pipe ($u_\theta = 0, \quad \partial/\partial\theta = 0$), equation 2.1 reduces to the following:

$$\rho\left[\frac{\partial u_z}{\partial t}+u_r\frac{\partial u_z}{\partial r}+u_z\frac{\partial u_z}{\partial z}\right]=-\frac{\partial p}{\partial z}+\rho g_z+\mu\left[\frac{1}{r}\frac{\partial}{\partial r}\left(r\frac{\partial u_z}{\partial r}\right)+\frac{\partial^2 u_z}{\partial z^2}\right] . \tag{2.3}$$

where u_z is the axial velocity, r, θ and z are the cylindrical coordinates, t is the time, ρ and μ are the density and dynamic viscosity, p is the pressure, and g is the acceleration due to gravity.

Assume that the flow is fully developed and has a constant pressure, so

$$\frac{\partial}{\partial z}=0 \text{ and } \frac{\partial p}{\partial z}=0 .$$

With these assumptions the continuity equation demands that $u_r = 0$. The boundary conditions are

$$u_z = 0 \quad \text{at} \quad r = R_w \text{ (no slip at tube wall)}$$

$$\frac{\partial u_z}{\partial r}=0 \quad \text{at} \quad r = r_i \text{ (no shear at gas-liquid interface)}$$

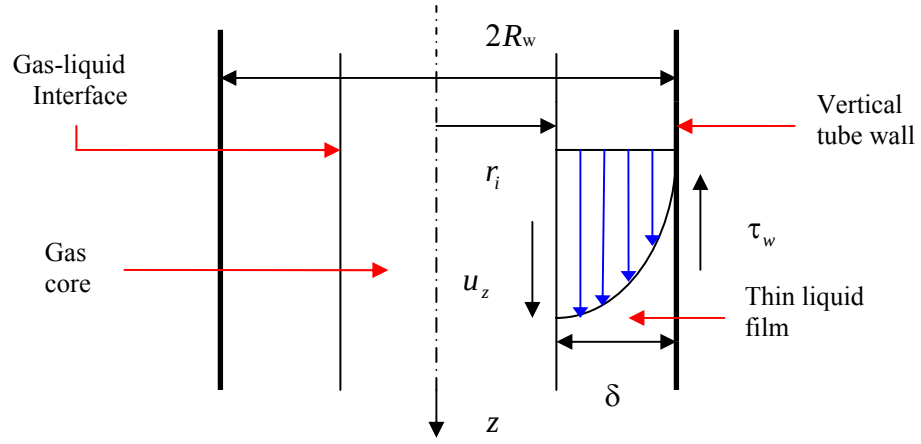

Figure 2.1: Velocity profile for a fully developed, laminar falling annular film

Recognising that u_z is now only a function of r, equation (2.3) reduces to the following:

$$\frac{1}{r}\frac{d}{dr}\left(r\frac{du_z}{dr}\right) = -\frac{\rho g_z}{\mu}. \qquad (2.4)$$

Integrating equation (2.4) with respect to r gives

$$r\frac{du_z}{dr} = \left(-\frac{\rho g_z}{\mu}\right)\frac{r^2}{2} + C_1. \qquad (2.5)$$

Now, applying the boundary conditions at $r = r_i$, $\frac{\partial u_z}{\partial r} = 0$ gives

$$C_1 = \left(\frac{\rho g_z}{\mu}\right)\frac{r_i^2}{2} \quad . \qquad (2.6)$$

Substituting this into (2.5) and integrating again gives

$$\mu u_z = -\frac{\rho g_z}{2}\left(\frac{r^2}{2} - (R_w - \delta)^2 \ln r\right) + C_2 \quad . \qquad (2.7)$$

Now, applying the no-slip condition for the liquid film at the wall ($u_z = 0, r = R_w$), gives

$$C_2 = \frac{\rho g_z}{2}\left(\frac{{R_w}^2}{2} - (R_w - \delta)^2 \ln R_w\right) \quad . \qquad (2.8)$$

This leads to an expression for the liquid film velocity as follows:

$$u_z = \frac{\rho g_z}{2\mu}\left((R_w - \delta)^2 \ln\frac{r}{R_w} + \left(\frac{{R_w}^2 - r^2}{2}\right)\right) \quad . \qquad (2.9)$$

This expression is similar to equation II-6 obtained by Brown (1965).

The wall shear stress is obtained by differentiating the liquid film velocity with respect to radius and evaluating the resulting expression at $r = R_w$. The final equation is given as follows:

$$\tau_w = \rho g_z\left(\delta - \frac{\delta^2}{R_w}\right) \approx \rho g_z \delta \qquad (2.10)$$

for $\delta << R_w$. Note that for the case of zero gas flow, the wall shear stress must

support the total weight of the film.

The mass flow rate of the liquid film can be obtained by integrating the liquid film velocity profile over the film cross section. Thus,

$$\dot{m}_l = \int_{r_i}^{R_w} \rho 2\pi r u_Z \, dr \quad . \tag{2.11}$$

Substituting equation (2.9) into (2.11) and integrating leads to,

$$\dot{m}_l = \frac{\pi \rho^2 g_z}{8\mu}\left(-4R_w{}^2 (R_w - \delta)^2 + R_w{}^4 - 4(R_w - \delta)^4 \ln\left(\frac{R_w - \delta}{R_w}\right) + 3(R_w - \delta)^4 \right) . \tag{2.12}$$

for given fluid physical properties ρ and μ, given pipe diameter ($2R_w$), and film thickness ($\delta = R_w - r_i$). Using this equation, the liquid film mass flow rate ($\dot{m}_l$) can be determined. By expanding the terms above in powers of (δ / R_w), it can be shown that the liquid film mass flow rate increases as a cubic power of film thickness.

2.2.2: Film thickness variation for a smooth laminar liquid film

A graph was plotted between flow rate and film thickness as shown in figure 2.2.

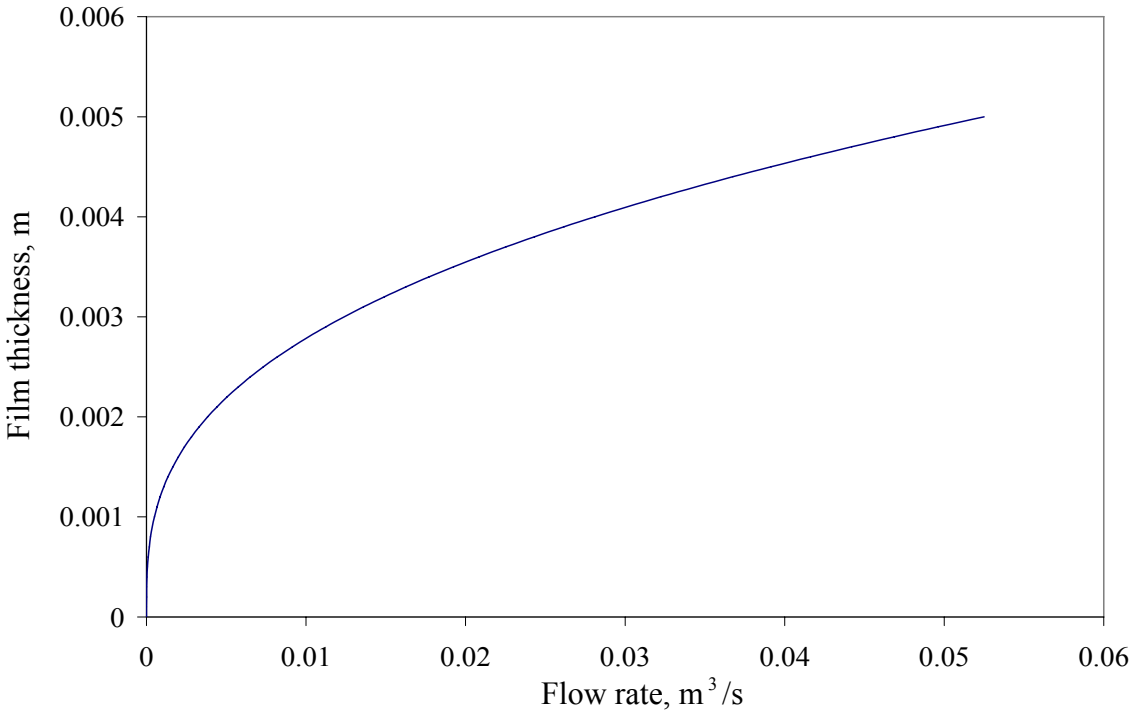

Figure 2.2: Parabolic profile of a smooth laminar falling liquid film

This curve was obtained by plotting equation 2.12. The inner tube radius was R_w = 12.74 mm and the working fluid used was water. Its physical properties at room temperature ($20 \pm 0.1\,^{\circ}$C) are dynamic viscosity $\mu = 0.001$ kg/ms, kinematic viscosity $\nu = 1$ cS, density $\rho = 998$ kg/m^3, and surface tension $\sigma = 72.8$ N/m. It was found that the liquid film mass flow rate increases as a cubic power of film thickness and a curve was obtained (as shown in figure 2.2) for the case of film thickness variation for a smooth laminar falling liquid film with no air flow. The formula does not restrict the flow, i.e., one could get the film thickness, δ could be larger than the inner tube radius, R_w.

2.3 Characteristic film thickness parameters

For a turbulent falling film, the instantaneous film thickness δ is considered to be a random fluctuating quantity. The definitions of mean film thickness $\overline{\delta}$, standard deviation, *s*, probability density function $P(\delta)$, as well as the combination of the above parameters such as the coefficient of variation $s/\overline{\delta}$ are discussed in more detail here.

2.3.1 Mean film thickness

Since waves and ripples are naturally present on most falling liquid films for all but the very lowest flow rates, the meaning of the phrase "liquid layer thickness" has to be carefully defined. There are three possibilities: (a) maximum layer height, (b) mean film thickness, (c) residual film thickness. The maximum layer height is the height of the highest wave crests; the residual film thickness represents the thinnest part of the film. The meaning of the mean film thickness seems obvious and it is the knowledge of the mean thickness of flowing liquid films which is of importance in a wide range of practical problems involving film flow. Such problems include the calculation of heat transfer in condensers and evaporators, and mass transfer in film-type equipments. As a result, much work has been carried out to determine the mean thickness of falling liquid films. The mean film thickness is defined as follows:

$$\bar{\delta} = \lim_{T\to\infty} \frac{1}{T} \int_0^T \delta(T) dT \quad . \tag{2.13}$$

where T is the time and $\delta(T)$ is the instantaneous film thickness in an observation time T.

2.3.2 Standard deviation

The root-mean-square (r.m.s.) of the fluctuations or standard deviation s, of a data sample is the positive square root of the second central moment, as defined below, and provides a measure of the "dispersion" of data about their mean value. The variance s^2 is defined as follows:

$$s^2 = \lim_{T\to\infty} \frac{1}{T} \int_0^T \left(\delta(T) - \bar{\delta}\right)^2 dT \quad . \tag{2.14}$$

The ratio of the standard deviation of film thickness fluctuations to the mean film thickness is the coefficient of variation $s/\bar{\delta}$. It is a very common indicator of wave growth.

2.3.3 Probability density function

The probability density function of the time series describes the probability that the data will assume a value within some defined range at any instant of time. Chu and Dukler (1974) defined "substrate film thickness" based on the characteristics of the probability density function of film thickness. Substrate film thickness was defined as the most probable film thickness and is indicated by a peak in the probability density function. The probability that $\delta(T)$ assumes a value within the range between δ and $(\delta + \Delta\delta)$ during an observation time T may be defined as follows (Bendat and Piersol 1971):

$$P(\delta) = \lim_{\Delta\delta\to 0} \frac{P\{\delta < \delta(T) < \delta + \Delta\delta\}}{\Delta\delta} \quad . \tag{2.15}$$

2.4 Literature Review

2.4.1 Classical theories and modelling studies

According to Fulford (1964), Nusselt proposed a theory for a smooth, laminar uniform, and two-dimensional flow on an infinitely wide plate in 1916. According to the theory, "the liquid film mass flow rate increases as a cubic power of film thickness and even a small difference in the film thickness results in a large difference in the liquid flow rate; especially for thick films obtained at high Reynolds numbers" (Refer to figure 2.2 in section 2.2). The equations, derivable from force balances on an element in the liquid film, were developed with the assumptions of viscous flow where no shear or wave motion existed at the liquid surface. This theory is very simple as it does not take into account the effects of even small waves on the falling liquid film. Nusselt's theory for a smooth laminar flow is as follows:

$$\bar{\delta} = \left(3\upsilon^2 Re/g\right)^{1/3}. \qquad (2.16)$$

Experimental observations of laminar falling liquid films indicated that the gas-liquid interface was not a constant flat surface, but exhibited a wavy structure at Reynolds number as low as $Re = 5$. Numerous theoretical attempts have been made to study the waves formed on free-falling liquid films. The research can be divided into three general groups with respect to Reynolds numbers. The first group refers to the wave evolution over laminar films flowing at low Reynolds numbers and it involves a number of different approaches. For smooth wavy laminar flow, the mean film thickness was given by Kapitza's (1965) theory which accounts for the effects of regular periodic waves and surface tension in a falling laminar film as follows:

$$\bar{\delta} = \left(2.4\upsilon^2 Re/g\right)^{1/3}. \qquad (2.17)$$

A parameter that had been identified to be important for characterising wavy laminar falling films besides Reynolds number was the Kapitza number, $\gamma = \sigma/\rho\nu^{4/3}g^{1/3}$, where σ is the surface tension and ν is the kinematic viscosity. Kapitza's (1965) theory appeared to account for the wavy nature of falling films only if the wavelength was less than 13.7 times the film thickness, which corresponds to a Reynolds number of $Re = 12$ for falling liquid films.

The second group of theoretical studies deals with films at higher Reynolds numbers. This is in a transition zone where fast-moving, large waves tend to overtake the small (capillary) waves resulting in a complicated wave structure. Numerical simulations of laminar wavy films at relatively high Reynolds numbers were conducted by several investigators (e.g., Wasden and Dukler (1989), Chang (1994), Yu *et al*. (1995) and Stuhltrager *et al*. (1995)), to predict the spatial variations in film thickness along with the velocity field inside the interacting waves. Wasden and Dukler (1989) examined wave structures of interacting waves in regions where the Navier-Stokes equations could be solved. Their model, based on flows with a Reynolds number of 220, predicted the existence of recirculation cells within large disturbance waves. In addition, the computational simulation depicted regions of acceleration in the wave fronts, and deceleration zones at the wave backs. This work was continued by Yu *et al*. (1995), examining the stability of the two-dimensional Navier-Stokes equations using non-linear wave evolution assumptions.

The third group of studies deals with even higher Reynolds numbers of $Re > 270$, which produce a turbulent film. The problem of turbulent flow in thin films is very complex and there are no theoretical treatments for wavy turbulent flow. A common approach is to neglect the surface waves and obtain solutions for the case of smooth turbulent flow. Nikuradse in 1933 developed the universal velocity distribution for circular tubes, which provided a means by which flows could be examined in terms of boundary layer analysis based on dimensionless parameters (Bird *et al*. (1960)). This theory was derived for fully-developed, single-phase, turbulent pipe flow. From the universal velocity profile equations developed by Nikuradse in 1933, Dukler and Bergelin (1952) derived a theoretical expression for dimensionless film thickness in the turbulent regime as follows:

$$\left(3.0 + 2.5 \ln \bar{\delta}^{+}\right)\bar{\delta}^{+} = Re + 64 \,. \qquad (2.18)$$

Equation 2.18 was obtained with the aid of the friction velocity u^{*}, evaluated from a force balance of wall friction and the gravity force as follows:

$$\rho g \; 2\pi R_w \delta dz = \tau_w \; 2\pi R_w dz \,. \qquad (2.19)$$

$$u^{*} = \sqrt{\tau_w / \rho} = \sqrt{g\delta} \,. \qquad (2.20)$$

The non–dimensional film thickness, $\overline{\delta}^{+}$, in equation 2.18 is defined as follows:

$$\overline{\delta}^{+} = u^{*}\delta \,/\upsilon . \qquad (2.21)$$

The falling film may become turbulent if the dimensionless film thickness $\overline{\delta}^{+}$, obtained from local film thickness δ, reaches a value of 30. Dukler and Bergelin (1952) also carried out an analysis in the laminar and transition zones and found that the transition from laminar to turbulent film flow occurs at a Reynolds number of 270.

A numerical study of turbulent wavy films for the fully developed region was carried out by prescribing a geometric shape for large waves by Brauner (1987). The proposed model could yield some useful information regarding the velocity distribution within large waves, including the effects of turbulence. Brauner (1987) showed that there are two basic characteristics of the wavy flow, namely the wave celerity and the average wavy film thickness. Wave celerity is the speed of propagation of the wave crest or trough. It is worth emphasising that these two parameters are the usual measured quantities that are of importance in modelling the momentum, heat and mass transfer, associated with wavy flow. Yet, the model was rather complex with different physical mechanisms controlling various zones along a large wave. Moreover, the employed shape of large waves – assumed to have a linear slope at both the front and the back of the waves – was oversimplified compared to experimental observations. An expression for the average film thickness was derived from energy and mass balances in stationary and moving coordinate systems. The average wavy film thicknesses for laminar and turbulent flows were obtained as follows:

$$\overline{\delta} = \left(\frac{3}{8}\upsilon^{2} Re/g\right)^{1/3} \quad \text{for laminar flow;} \qquad (2.22)$$

$$\overline{\delta} = 0.104\left(\upsilon^{2}/g\right)^{1/3} Re^{7/12} \quad \text{for turbulent flow.} \qquad (2.23)$$

The other available literature on theoretical developments range from classical works dealing with the stability of the film surface (e.g., Kapitza (1947); Benjamin (1957); Yih (1963); Bankoff (1971); Spindler (1981); Kokamustafaogullari (1985) to a

rigorous mathematical study of the behaviour of falling films (Alekseenko *et al*., 1994). A few studies used finite element solutions of the full Navier stokes equations (e.g., Bach and Villadsen (1984); Kheshgi and Scriven (1987); Salamon *et al*. (1994) assuming waves with finite amplitude or a stationary profile. Other efforts were based on simplified Navier - Stokes equations under various approximations or order-of-magnitude assumptions (e.g., Alekseenko *et al*. (1985); Nguyen and Balakotaiah (2000)). On the whole, these studies found waveforms that are only in fair agreement with experimental observations and only for small Reynolds numbers – usually below 75 – which are much lower than those encountered in many practical applications.

2.4.2 Experimental studies

Many techniques have been used for the measurement of mean film thickness and to study the statistical characteristics of film thickness. It is worth mentioning here that the mean film thickness obviously depends to a certain extent on the measurement being adopted. The results of the experimental studies and the details of the proposed experiments are reviewed in more detail in this section.

According to Fulford (1964), Brotz studied films of water and refrigerating oil inside tubes of various diameters with kinematic viscosities of 1.0-8.48 cS and $Re = 100 - 4300$ using a drainage technique in 1954. In this technique, the feed of liquid to the channel is shut off and the liquid film flowing from the channel is collected and measured. Knowing the wetted area of the channel, the mean film thickness can be determined from the volume of the liquid collected. Later it was realised by Portalski (1963) in his experiments with water films in vertical tubes that this type of apparatus suffers from certain disadvantages which preclude a thorough examination of the many phenomena relating to the hydrodynamics of film flow. In his experience, it is very unlikely to produce highly accurate and reproducible results unless the apparatus has an automatic device for stopping the feed and simultaneously collecting the drainage from a fairly large wetted area. This cannot be achieved easily, if at all, using small-bore tubes of moderate length and for high liquid flow rates. The main difficulty is to ensure fully instantaneous isolation of the section.

The critical Reynolds number at which turbulence was found to commence was 590. From dimensional considerations, Brotz showed that, in the turbulent regime, the mean film thickness is given as follows:

$$\bar{\delta} = 0.112\left(3\upsilon^2/g\right)^{1/3} Re^{2/3}. \qquad (2.24)$$

Jackson (1955) used a radio active emission technique to determine the film thickness in falling liquid films. In this technique, a radio active substance is dissolved in the flowing liquid. If a radioactive detector is brought up to the film, the amount of radiation detected depends on the film thickness. The radiation is, of course, partially attenuated by absorption in the liquid film. Jackson (1955) came up with the following expression for laminar liquid films:

$$\bar{\delta} = C\, A_c \ . \qquad (2.25)$$

where C is a constant and A_c is described as the corrected absorption activity of the liquid film (counts/sec). The constant C in the equation was evaluated by operating the vertical tube apparatus under conditions where the film thickness could be calculated from the flow rate using Nusselt's equation. That is, the value of the constant was determined by plotting corrected absorption activity A_c against the calculated film thickness $\bar{\delta}$. The problem with this technique is the fact that, even if this could be done for the region where the flow is truly viscous and waves are absent, this method automatically shifts the experimental film thickness results at low flow rates and pins them down on the theoretical line proposed by Nusselt in 1916. But Nusselt's theory fails to predict the film thickness correctly, even for steady laminar conditions of flow, that is, before the onset of wave motion (Portalski 1963). On examination of his results, Jackson (1955) states that "the data permits few conclusions concerning the inception of turbulence" and that "for water and the lighter liquids no significant departure from viscous behaviour is indicated up to Reynolds numbers of 1250 although scattering of the data is observed above *Re* = 500". In view of the above criticism, Jackson's (1955) results are not entirely surprising.

According to Fulford (1964), Brauer in 1956 carried out extensive experimental studies of film flow outside tubes of diameter 4.3 cm and length 130 cm for kinematic viscosities of 0.9-12.7 cS and at *Re* = 20-1800. He used the feeler-probe method which is a refined modification of the micrometer screw method. Here, a very fine needle is mounted on a micrometer and is adjusted to touch the liquid film, the contact being registered normally by an electronic counter. The objection to this method is quite obvious: by touching the surface of the film by a probe, or even worse, by introducing the probe into the film, however fine the probe may be, one interferes with the natural flow of the film. One measures, therefore, a disturbed condition which may not be closely related to the original undisturbed flow. The lower limit of critical Reynolds number was found to be equal to 400. For turbulent flow, the mean film thickness was well described by the following empirical formula:

$$\overline{\delta} = 0.302\left(3\upsilon^2/g\right)^{1/3} Re^{8/15} . \qquad (2.26)$$

Belkin *et al.* (1959) carried out photographic techniques at zero gas flow and at different Reynolds numbers in the lower and higher turbulent regimes. A direct lighting technique was used for water flowing down the outer surface of a vertical glass rod of diameter 25.48 mm for Reynolds numbers above 1258. High-speed photographs of the rod with water flow were compared with photographs of the dry rod, using a planimeter on enlarged photographs. There was evidence of discrete turbulent eddies at *Re* = 1258 which indicates the persistence of transitional flow. It was apparent that the data did not make it possible to fix the exact Reynolds number at which the advent of turbulence begins to affect the thickness parameter. The photographs presented at even higher Reynolds number showed that full turbulence had been obtained. Additional photographs indicated more intense turbulence but the same over-all type of flow at Reynolds numbers between 4000 and 7500. It showed the random distribution of shallow troughs and crests in the fully turbulent region and the turbulent waves took nearly a trochoidal form. A trochoid is the curve generated by a point on a circle which rolls along the underside of a straight line. Their pictures made it easy to visualise that a profile cutting across the indentation between adjacent crests might closely resemble such a form. According to Portalski (1963), it is extremely difficult to enlarge photographs to exactly the same length – especially if

two cameras are used for the purpose – unless the photographed portions are marked beforehand. In any case, the three-dimensional effect of the waves was quite obvious in the photographs submitted.

According to Fulford (1964), Fiend in 1960 used a drainage technique and measured the thickness of various films for kinematic viscosities from 1 to 19.7 cS flowing in vertical tubes ($2.0 - 5.0$ cm diameter). At low Reynolds numbers, the values of film thickness agreed well with Nusselt's predictions. Once the wavy flow commenced, the values deviated towards the Kapitza line (equation 2.17). At larger Reynolds numbers, there was a gradual transition back towards the Nusselt line (equation 2.16) which was finally crossed at $Re = 350$. In the turbulent zone, the experimental values fell above the Nusselt line. The lower and upper value of critical Reynolds number was found to be 400 and 800, respectively. For the turbulent regime, it was found that

$$\bar{\delta} = 0.369\left(3\upsilon^2/g\right)^{1/3} Re^{1/2}. \qquad (2.27)$$

According to Fulford (1964), Zhivaikin and Volgin in 1961 used an analogy with pipe flow and measured mean film thickness in a tube 2 cm in diameter and 98 cm long at $Re = 150 - 3500$ with water as the working fluid. The lower limit of critical Reynolds number was found to be 400, at which turbulence commenced, and an upper value of 1000, at which the flow became fully turbulent. For the turbulent regime, the mean film thickness was obtained as follows:

$$\bar{\delta} = 0.141\left(\upsilon^2/g\right)^{1/3} (4Re)^{7/12}. \qquad (2.28)$$

Neal and Bankoff (1963) and numerous other researchers measured liquid film thickness using a needle-contact probe. In principle, the point of the needle is brought upon the film and when the needle makes contact, the distance between the needle point and the solid boundary is noted. If the film is of uniform thickness with no waves, the first point of contact represents the film thickness. When there are waves on the film, however, contact is first made with the tips of the waves and a continuous contact does not occur until the troughs of the waves are being touched. The point of contact is determined by electric capacity methods. It gives results for contact frequency and relative contact time. This probe is accurate and easy to handle, but suffers from limited spatial resolution. Telles and Dukler (1970)

conducted electrical conductivity measurements in a 5.4 m long rectangular conduit made of Plexiglas. In this technique, it is necessary for the film to be conducting (e.g., by adding electrolytes) and for it to flow over the electrodes. Electrical connections to the selected length of film are then made by insertion of electrodes in the wall. Statistical characteristics of thin, vertical, wavy, liquid films were determined at Reynolds numbers in the range 225 to 1500 and showed the random nature of waves and their behaviour as a two wave system; large waves which carry the bulk of the liquid and the small waves which cover the substrate. The probability density distribution had a maximum peak and a long tail stretching from 5 to 12 times the minimum film thickness. A comparison of their mean experimental film thickness with the values predicted by Dukler and Bergelin (1952) theory showed significant deviations. It seems clear that the original development of Dukler and Bergelin (1952) does not produce the correct mean film thickness for a film with large waves. Webb and Hewitt (1975) carried out measurements in downward annular two phase flows in tubes of 3.18 and 3.28 cm bore. The film thickness data showed reasonable agreement with Telles and Dukler (1970) although there were slight discrepancies which could be attributed to the effect of wall curvature.

Later Chu and Dukler (1975) used conductivity probes to determine the statistical characteristics of thin wavy turbulent liquid films inside Plexiglas pipes of diameter 50 mm and length 4.27 m. In this technique, the probes are placed in close proximity to one another in the surface over which the film is flowing and flush with the wall. The conductance between the probes depends on the liquid film thickness and the specific conductivity of the liquid. Two classes of random waves were found to exist on falling films at flow rates of practical interest ($Re > 175$). In order to characterise the random large waves, it was necessary to measure their mean film thickness, standard deviation, and probability density distribution. The probability density distribution curve obtained was highly asymmetrical around the modal value. The maximum peak values decreased sharply with increasing liquid flow rate and the long tail existed which stretches to over six times the modal value. Such measurements confirm, in general, certain statistical characteristics of large waves as suggested by

Telles and Dukler (1970). Salazar and Marschall (1978) measured the interfacial characteristics using light scattering and hot-film probes, but these did not easily yield the absolute film height. Blass (1979) did an extensive study of falling liquid films in vertical tubes for Reynolds numbers up to 2000 and found that the mean film thickness appeared to be the same for vertical flat plates and for flow outside or inside a vertical tube, provided the ratio of film thickness to tube radius is small (i.e., less than 0.2). The effect of the film curvature cannot be neglected for falling annular films on and in narrow tubes, or on wires or fibres, when the ratio of the film thickness to tube radius is greater than 0.2.

Figure 2.3 shows a sample of the earlier non-dimensional film thickness data plotted against the Reynolds number (Refer to Fulford, G.D., 1964). Takahama and Kato (1980) carried out flow measurements using needle contact and electric capacity methods along the outer wall of a circular tube (44.92± 0.02 mm in diameter and 2

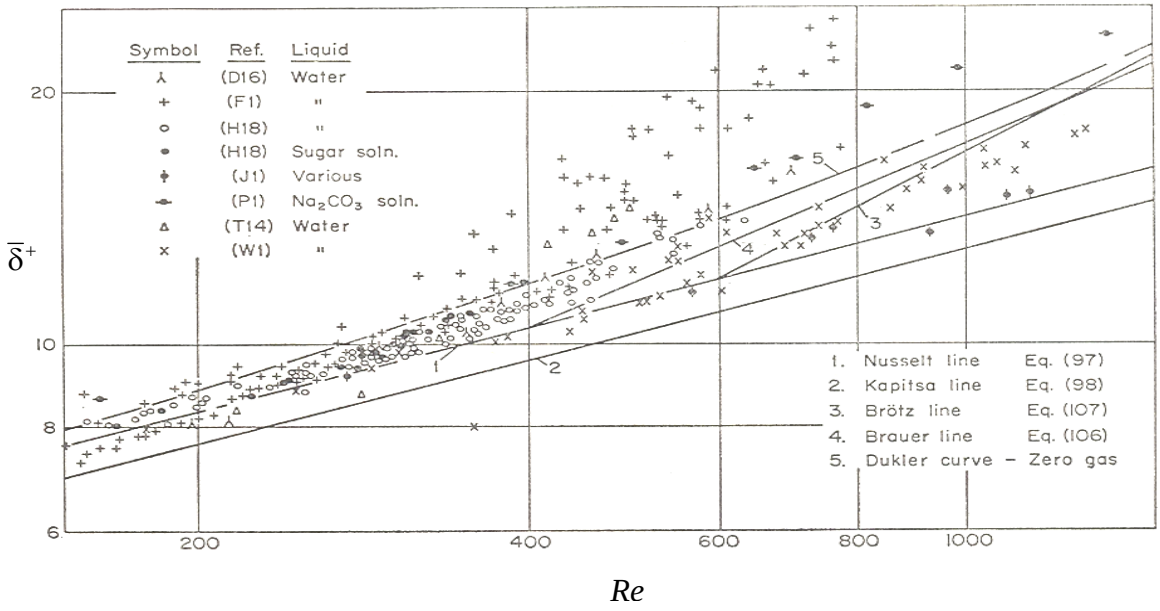

Figure 2.3: Sample of earlier film thickness data near the critical Reynolds number plotted in terms of the dimensionless mean film thickness parameter ($\overline{\delta}^+$) and the Reynolds number (*Re*), for the case of zero gas flow ("Reprinted from In: Advances in Chemical Engineering, Vol. 5, Fulford, G.D., The flow of liquids in thin films, 151-235, 1964, with permission from Elsevier")

m long) with and without concurrent gas flow. The test channel used was a brass cylinder with water as the working fluid. The mean film thickness data obtained were statistically processed. First, the probability distribution function was obtained by the needle contact method at different positions along the circumference of the tube. Then, the mean film thickness was evaluated from graphical integration of the probability distribution. It was found that at small Reynolds numbers of Re = 200 and longitudinal distance of z = 100 mm, $\overline{\delta}$ decreases only by 3% from its initial value at the inlet. On the other hand, at large Re = 997 and z < 500mm, $\overline{\delta}$ increases rapidly, but at larger longitudinal distances becomes constant. For intermediate Reynolds numbers between 200 and 997, $\overline{\delta}$ increases, decreases to a minimum level and then increases again. This peculiar behaviour may be due to transition from laminar to turbulent flow. The experimental results obtained were compared with the theories for laminar and turbulent flow (equation 2.16 and 2.18) and also with Brauner's (1956) empirical formula (equation 2.23). At $Re < 400$ the experimental results agree with those of Nusselt's theory (equation 2.16) and at $Re > 400$ the experimental results tend to coincide with Brauner's equation (equation 2.23) for turbulent flow. The lower value of critical Reynolds number Re is obtained at the intersection of the laminar and turbulent lines. Evaluation of critical Reynolds number leads to Re = 368 which agreed closely with the theory of smooth turbulent flow (equation 2.18). Although it provided useful statistical information about the distribution of film thickness; it could not give information about the continuous change of film thickness since only one depth is investigated at each needle setting. The other difficulty with the method is the problem of contact hysteresis; the film may tend to stick to the needle and the break of contact with the film may therefore be delayed. A further disadvantage of the method is that the flow must necessarily be disturbed in other parts of the channel in order to introduce the contact needle (Hewitt and Hall-Taylor, 1970). The mean film thickness in the turbulent regime was given by the following empirical formula:

$$\overline{\delta} = 0.473\left(\upsilon^2/g\right)^{1/3} Re^{0.526}. \qquad (2.29)$$

Zabaras (1985) carried out measurements of the film thickness in falling annular films using a flush-mounted probe. The method is based on the fact that the electrical conductance between two probes, placed flush on wall over which a liquid film is flowing, depends on the thickness of the film. The vertical test section was made of several segments of Plexiglas pipe with an inside diameter equal to 50 mm ± 20mm and the overall length was 6.5 m. The film thickness obtained at low Reynolds number and at short distances from the entry was found to be in good agreement with Nusselt's film thickness equation. At larger distances from the liquid entry (1.94 m and 4.0 m) the waves were developed. In particular, the waves at the 4.0 m location could be considered to be fully developed. At these distances, the values deviated from the Nusselt line indicating a transition to turbulence. The standard deviation of the film thickness was also found to increase with increasing liquid Reynolds number and longitudinal distance from the liquid inlet. This implies that at larger distances the waves have higher amplitudes. The probability density distribution curves also suggested the existence of high wave amplitudes at this location. The possible objections to the use of flush-mounted probes come from the perturbation induced in the flowing film of liquid and from a meniscus effect due to the wetting of the wires.

Koskie *et al*. (1989) used parallel-wire probes and determined film thickness in falling liquid films at Reynolds numbers in the range 250 to 18,750. The measuring technique consists of two parallel fine wires placed side by side in the pipe perpendicular to the direction of the flow. By using the liquid as a conductor it is possible to measure the resistance between the two wires and convert the resistance to a measure of the immersion of the wires. It is based on the fact that the resistance is inversely proportional to the length of the wires immersed in the liquid. They obtained continuous measurements of film thickness for thick films (> 1 mm), but the resulting probe yielded some error for thin liquid films (< 1 mm). Karapantsios *et al.* (1989) also studied characteristics of free falling films at Re = 126-3275 using a parallel wire conductance technique. In their experiments, water was used as the working fluid. It was found that at $Re > 375$, the random character of the film flow becomes more pronounced. The Reynolds number was found to correlate well with the characteristic film thickness parameters such as standard deviation, s and

coefficient of variation, $s/\overline{\delta}$. Information obtained on the film thickness fluctuations showed that they exhibit a stochastic character. The mean film thickness was given by the following empirical formula:

$$\overline{\delta} = 0.451\left(\upsilon^2/g\right)^{1/3} Re^{0.538}. \qquad (2.30)$$

Since spatial resolution and calibration have been typical problems in the practical use of traditional conductance probes such as flush-mounted probes and parallel-wire probes, Kang and Kim (1992) developed a flush-wire probe. It consists of an electrode which is flush with the wall and a wire electrode which is vertically inserted from the top side. This technique enhanced the spatial resolution and enabled continuous measurement of liquid film thickness up to a Reynolds number of 1500. Their measured mean film thickness was found to be 0.1 mm lower than those of Takahama and Kato (1980) and Karapantsios *et al*. (1989), but slightly larger than Salazar and Marschall (1978). Karimi and Kawaji (1998) carried out film thickness measurements in falling annular films at *Re* = 352 - 1637 with deodorised kerosene as the working fluid using the photochromic dye tracer technique. In this technique, the dye trace appears as a deep blue straight line along the path of the laser beam. The dye trace formed follows the motion of the liquid and thereby tracks the movements of the liquid elements. Large scatter in film thickness measurements were reported especially at high Reynolds numbers in the turbulent flow regime. Recently, Ambrosini *et al*. (2002) determined the statistical characteristics of freely falling films down a vertical plane (2 m long, 0.6 m wide and 0.022 m thick). Capacitance probes, consisting of two parallel conducting plates mounted vertically were used to collect discrete film thickness time series and to extract relevant statistical data. One of these plates was fixed in position while the second plate could be moved to vary the distance between the plates. The capacitance of this sensor was directly proportional to the dielectric constant of the fluid between the plates and the area of the plates. The mean film thickness data were in reasonable agreement with Nusselt's theory for low Reynolds numbers after which larger deviations appeared, possibly due to transition to turbulent flow. The standard deviation was also found to

be in good agreement with Karapantsios *et al.* (1989) in the range of Reynolds number, *Re* = 100-400.

2.3 Summary

The experimental, theoretical, and modelling methods along with conditions such as test geometry, measuring location relative to the inlet and the correlation for the film thickness obtained for the turbulent regime are summarised in Table 2.1.

Table 2.1: Summary of experimental, theoretical, and modelling methods used in the past for a vertical downward annular flow without air flow.

Researchers	Geometry	Reynolds number	Experimental/Model/ Theoretical	Film thickness correlation
Dukler and Bergelin (1952)	Flat plate/ Pipe inside	> 270	Theory	$\left(3.0+2.5\ln\bar{\delta}^{+}\right)\bar{\delta}^{+}=Re+64$
Brotz (1954)	Pipe inside	100 - 4300	Drainage technique	$\bar{\delta}=0.112\left(3\upsilon^{2}/g\right)^{1/3}Re^{2/3}$
Brauer (1956)	Pipe outside	20 - 1800	Feeler probe method	$\bar{\delta}=0.302\left(3\upsilon^{2}/g\right)^{1/3}Re^{8/15}$
Belkin *et al*. (1959)	Pipe outside	1200 - 7500	Photographic technique	Not available
Fiend (1960)	Pipe inside	-	Drainage technique	$\bar{\delta}=0.369\left(3\upsilon^{2}/g\right)^{1/3}Re^{1/2}$
Zhivaikin and Volgin (1961)	Pipe inside	150 - 3500	Not available	$\bar{\delta}=0.141\left(\upsilon^{2}/g\right)^{1/3}(4Re)^{7/12}$
Chu and Dukler (1975)	Pipe inside	150 -1500	Flush-mounted probe	Not available
Webb and Hewitt (1975)	Pipe inside	-	Conductance probe method	Not available
Salazar *et al*. (1978)	Flat plate	-	Laser scattering	Not available
Takahama and Kato (1980)	Pipe inside	150 - 2000	Needle contact and capacitance probe	$\bar{\delta}=0.473\left(\upsilon^{2}/g\right)^{1/3}Re^{0.526}$
Zabaras (1985)	Pipe inside	-	Wire conductance probe	Not available

Brauner (1987)	Flat plate	-	Model	$\overline{\delta} = 0.104\left(\upsilon^2/g\right)^{1/3} Re^{7/12}$
Koskie *et al*. (1989)	Pipe inside	250 – 18,750	Parallel wire conductance probe	Not available
Karapantsios *et al*. (1989)	Pipe inside	126 - 3275	Parallel-wire conductance probe	$\overline{\delta} = 0.451\left(\upsilon^2/g\right)^{1/3} Re^{0.538}$
Kang and Kim (1991)	Flat plate	150 -1500	Flush-wire probe	Not available
Ambrosini *et al*. (2002)	Flat plate	100 - 400	Capacitance probe	Not available

CHAPTER 3

APPARATUS AND MEASUREMENT TECHNIQUES

3.1 Introduction

The experimental and measurement procedures described in this chapter were undertaken to produce instantaneous measurements of film thickness in falling annular liquid films. The experiments were conducted in a 4 m long vertical tube of 25.48 mm (1 inch) inside diameter. Water was used as the working fluid. The tube was long enough to establish a fully developed flow in the test section. Flow visualisation studies in falling annular films were carried out using a non-intrusive digital photographic technique. The main instruments used were a digital camera and a pair of remote flash units to capture instantaneous images of a falling annular film. The flow loop, calibration procedures, image analysis techniques, and optical distortion correction techniques used in the experiments will be discussed in detail in this chapter.

3.2 Flow Loop

A schematic of the experimental apparatus is shown in figure 3.1. The flow loop was designed to produce a fully developed, gravity-driven liquid film in the test section. The test section consists of a 4 m long transparent vertical tube with an inside diameter of 25.48 mm suspended from the upper reservoir. In order to produce a uniform film, a bell-mouth entrance was fitted to the upper end of the tube. Marbles of diameter 19 mm (3/4 inch) were placed in the upper reservoir to break down the jets of water at the liquid inlet into the upper reservoir. This ensured a smooth entry

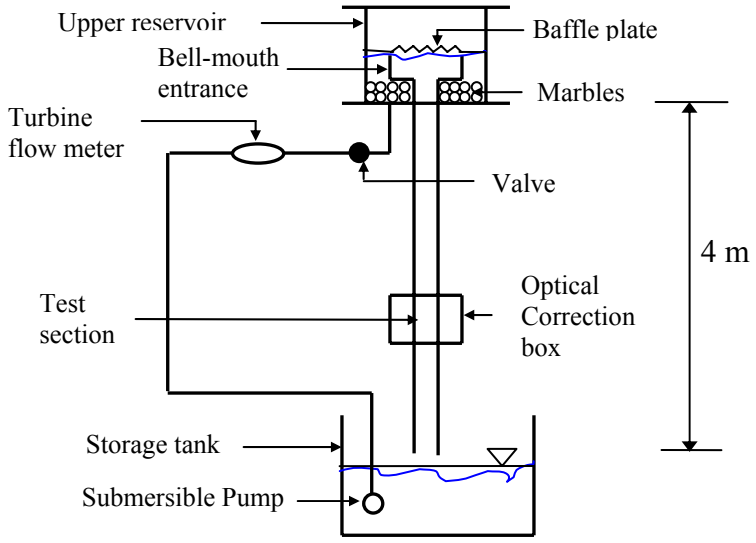

Figure 3.1: Experimental apparatus for the falling annular film studies

of the test liquid into the acrylic tube from the upper reservoir. An optical correction box was mounted on the tube at the film thickness measurement location and was used to partially correct the optical distortion created by the circular wall of the test section. This optical correction box was filled with the working fluid. After the test liquid passes through the vertical tube it is collected in the storage tank. For the lower flow rates, a submersible pump recirculates the water back to the upper reservoir. A larger centrifugal pump was used at higher liquid flow rates. A baffle plate was placed over the marbles to prevent them from falling out of the reservoir at high liquid flow rates. It also served to break-down the jets and allowed a more uniform flow at the test section inlet. A turbine flow meter measured the flow rate. A valve at the outlet of the flow meter was used to regulate the flow.

A calibration of the turbine flow meter was carried out. During the calibration, water was collected in a separate reservoir and then weighed using a scale. The time taken to collect the water was measured using a stop watch. Several measurements were taken to ensure repeatability of the calibration results and to reduce the uncertainties involved in the experiments. Figure 3.2 shows the relationship between the mass flow rate and the output voltage of the turbine flow meter. A third-order polynomial fit to this data was obtained. A thermometer was used to monitor the temperature of

the working fluid. During the course of experiments, it was found that the small rise or fall in temperature of the working fluid did not have any appreciable influence on the measured flow rate. The working fluid used in this study was water. Its physical properties at room temperature ($20 \pm 0.1\,^{\circ}C$) are dynamic viscosity $\mu = 0.001\,kg/ms$, density $\rho = 998\,kg/m^3$, and surface tension $\sigma = 72.8\,N/m$.

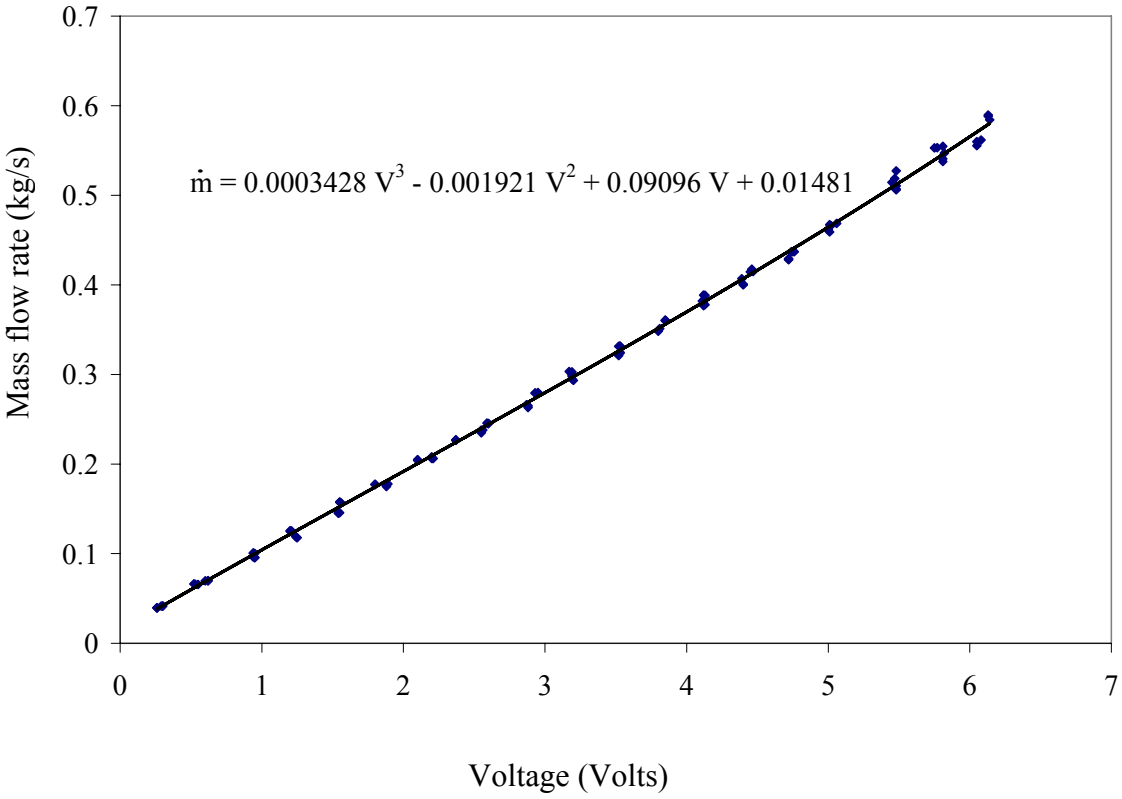

Figure 3.2: Calibration curve for the turbine flow meter

3.3 Instrumentation

A Nikon D70 digital SLR camera along with the two remote SB-600 AF flash units were used to capture images of the falling annular film. This section discusses the important features of a Nikon D70 digital SLR camera, spatial resolution, shooting and focus modes, and lighting techniques. The operating principle of a Nikon D70 digital SLR camera is similar to a 35 mm single-lens reflex (SLR) camera. SLR's are typically 35 mm film cameras and one can see directly through-the-lens (TTL) via a

mirror that reflects the image to the viewfinder. The mirror moves out of the way when the shot is taken.

3.3.1 Important features of a Nikon D70 Digital SLR Camera

The basic components of a Nikon D70 digital SLR camera are very important and there are many features not seen on conventional cameras. Figure 3.3 illustrates the location and some of the features on a Nikon D70 digital SLR camera.

Figure 3.3: Components of a Nikon D70 digital SLR camera

1. Battery Compartment: This is the slot for installing the camera's batteries. The batteries are rechargeable. It can hold multiple batteries.
2. Control Panel: The control panel is a small liquid crystal display (LCD) that displays the current settings, battery life, number of images remaining to be taken, and mode operation of the camera.
3. Lens: The lens is a piece of ground glass or plastic that focuses the light on the sensors. It is mounted in a cylindrical housing, which is attached to the front of the camera. The lens moves within the housing closer or nearer to the image sensors, which allows focussing of the image. The lenses are detachable and interchangeable.
4. Shutter Release: The shutter release is a multifunction button, found on the top right part of the camera. It is used in its half-pressed mode to set metering and focus. In its fully pressed mode, it releases the shutter to expose the electronic image sensors and capture the image.
5. Threaded Lens Barrel: The lens barrel is threaded and it can accept a wide variety of special-effects, and close-up filters. It can also adapt to wide-angle lenses. It can be spotted by looking at the screw threads at the inside rim of the metal that surrounds the front lens element.

3.3.2 Spatial resolution and image quality

The spatial resolution is the distance in the object plane represented by one pixel in the image plane. The factors affecting the spatial resolution are sensor pixel count, sensor size, lens and extension ring combination, and object distance. The Nikon D70 digital SLR camera has a sensor pixel count of 3008×2000. The lens of the camera focuses the light collected from the object on to the image plane. A 200 mm camera lens was used for this purpose. An extension ring attached to the camera lens served to allow closer object distances and thereby increase the resolution of the images. The object distance was then adjusted so that the tube diameter almost filled the image area.

3.3.3 Shooting and focus modes

The Nikon D70 digital SLR camera was operated in the manual shooting mode. The manual mode of operation allows for a higher degree of control over the exposure, giving options that automatic mode cannot offer in many situations. Exposure is controlled by the size of the aperture, the duration and intensity of the flash, the sensitivity of the CCD, the placement of the flash units, and the scene being photographed. To maximise the overall sharpness of the image from as close to the camera as possible, the smallest *f*-stop (largest number, *f*-22) was used to narrow the aperture as much as possible. This counterbalancing of aperture and flash settings allowed choosing between controlling depth-of-field (aperture) or stop action (external flash) while maintaining a level of exposure. Focus is the ability of the camera lens to bring to clarity the most important parts of an image's detail. Focus was achieved by manually adjusting the focus ring on the lens. Two remote SB-600 AF flash units were used to increase the level of exposure in the images. The SB-600 AF speedlights were connected to the camera via a hot shoe and a synchronous cord. The external flash has a zoom in the range 24-85 mm and an output power of M1-1/64. The external flash has a rotating head which made it possible to direct the illumination evenly over the object. The duration of the electronic flash unit was approximately 1/25,000 seconds at M1/64 output, which is faster than any shutter. This enabled freezing the rapid movements of the liquid film. Also, using a second flash dramatically increased the ability to control the contrast of the light in several areas of a photo at once.

3.4 Procedure for determination of the wall location

The correct position of the vertical tube wall was determined by taking pictures of the air-water meniscus with stagnant water in the tube. A spirit level was used to ensure that the tube was vertical. The wall position is shown by a thin vertical yellow line in figure 3.4. Among the most critical parameters needed was the pixel scale factor which relates a physical dimension to the pixel size. The pixel positions for the wall on both sides were recorded. This combined with the known inside diameter was used to determine the pixel scale factor (pixel to millimetre conversion). It was found

to be equal to 108.7 pixels/mm. The pixel scale factor needs to be determined only once for a given camera setup. The factor has been found to be very consistent, even after moving and remounting the camera apparatus several times. It is important, however, that the Nikon D70 digital SLR camera be mounted quite rigidly on the tripod stand with respect to the wall location of the test section to maintain a constant pixel scale factor and to reduce any noise due to movement of the camera. Possible movement of the camera is a potential source of a large systematic uncertainty. Measurements of the wall location were carried out before and after the film thickness measurements to eliminate this possibility. The difference was at most one pixel in magnitude. This corresponds to about 0.0091 mm.

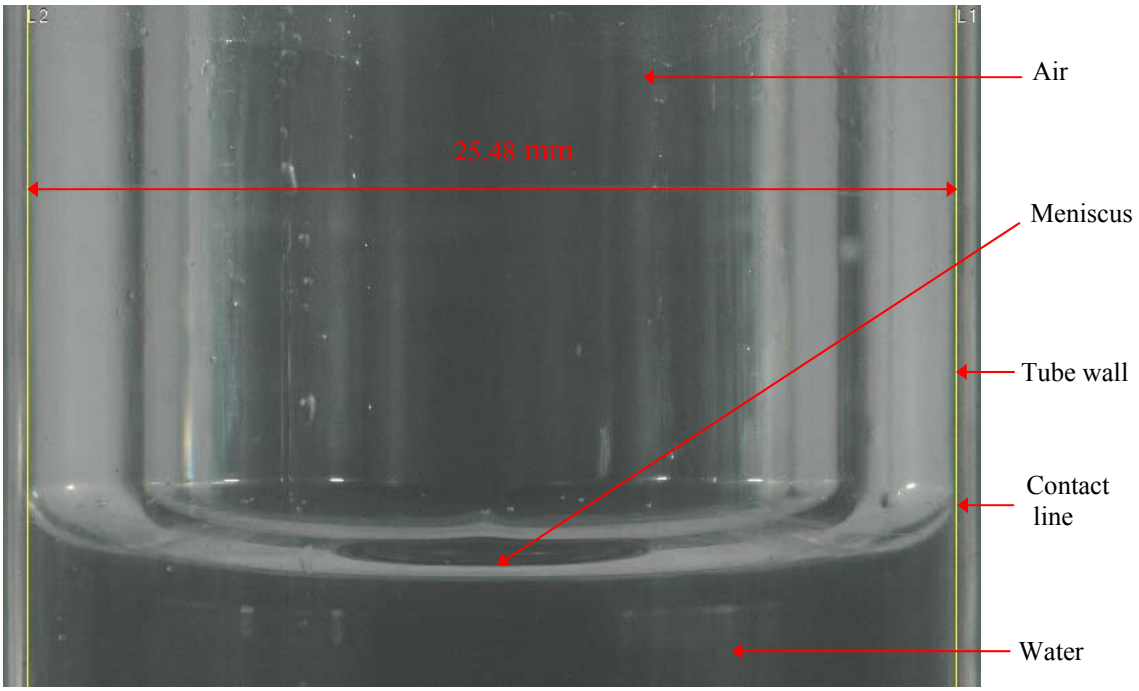

Figure 3.4: Static image of the water meniscus with the tube wall shown by a thin vertical line

3.5 Image processing

Images are two-dimensional representations of the visual world. Images are important sources of information for data interpretation and analysis. Image processing is a term used to describe operations carried out on images; the objective

might be to reduce noise or to extract information of particular interest to the observer (Pearson, 1991). The visual inspection process is time-consuming and is subject to inconsistency. Computers, on the other hand, are ideal for performing these tasks. For computers to process images, the images must be numerically represented. This process is known as image digitisation. Once images are represented digitally, computers can reliably automate the extraction of useful information using digital image processing. Digital image processing performs various types of image enhancements and measurements. Inspector® is a hardware-independent application designed for image capture, storage, and processing applications. Inspector® provides a comprehensive set of image processing operations. There are two main types of processing operations:

1. Those that enhance or transform an image;
2. Those that take measurements in an image, i.e., generate a numeric or graphical report that relates to specific image information.

3.5.1 Image enhancement and measurement operations

Inspector's® image enhancement and transformation operations improve the quality of the image and / or transform the image. Only the techniques used in this thesis will be discussed here. These include:

1. Point-to-point operations: These operations include brightness and contrast adjustment, and thresholding. Point-to-point operations compute each pixel result as a function of the pixel value at the corresponding location in the original image.
2. Spatial filtering operations: These operations are also known as convolution operations. They include operations that can enhance and smooth images, accentuate image edges, and remove noise from an image. Most of these operations compute results based on an underlying neighbourhood process: the weighted sum of a pixel value and its neighbour's values.

3. Morphological operations: These operations include opening, closing, erosion and dilation of images. These operations compute new pixel values according to geometric relationships and matches to known patterns in the input image.
4. Measurement operations: These operations include distance and angle measurements, as well as measurements using selected spatial positions (known as markers).

3.5.2 Flowchart representation of sequence of operations

Digital image processing operations such as image enhancements, transformations and extraction of measurements was performed using Inspector®. The typical application steps that were followed for the extraction of instantaneous film thickness measurements are represented as a flowchart in figure 3.5. The images were pre-processed to improve their quality before extracting information from them.

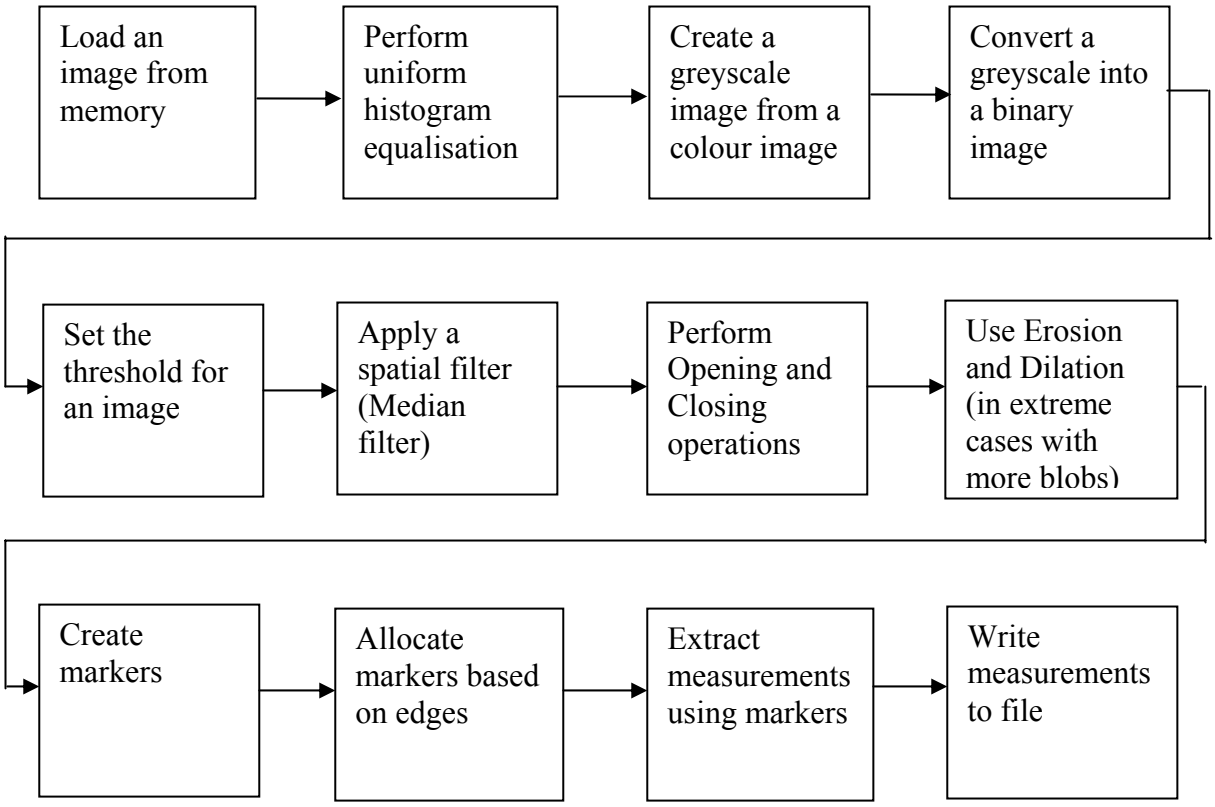

Figure 3.5: Flow chart of steps followed in digital image processing using Inspector®

3.5.3 Description of image processing operations

- First, the image was loaded from memory.
- All colour images were converted into grey scale images. A greyscale image was created because certain image processing operations such as measurement operations can be performed only on 8-bit unsigned greyscale images (pixel value 0 to 255).
- Then, the intensity distribution of the image was adjusted by performing a histogram equalisation operation. The process is spatially adaptive as histogram modification is applied to each pixel based upon the histogram of pixels within a moving window neighbourhood. This process resulted in a more uniform distribution of the image's pixel values.
- The thresholding operation was carried out to define a range of brightness values in the original image, selecting the pixels within this range as belonging to the foreground, and rejecting all other pixels to the background. Such an image was then displayed as a binarised or two-level image, using black and white colours to distinguish the regions (Russ, 1995). Since a thresholded image contains fewer pixel values than the original image, some operations can be performed more efficiently.
- The Gaussian random noise and systematic noise with small scale variations were reduced by applying a median filter to the image. The Gaussian random noise may be caused, for example, by the camera or digitiser because, in general, electronic devices tend to generate noise. This type of noise introduces pixels of arbitrary values that are generally noticeable because they are completely unrelated to the neighbouring pixels. Systematic noise can be predicted, appearing as a group of pixels that are not part of the actual image. It may be caused, for example, by the camera or digitiser, or by uneven lighting. If the image was magnified, microscopic dust particles, on either the object or a camera lens, may appear to be part of the image. Median filter operations were more suitable for removing such noise, since they replaced each pixel with a value from its neighbourhood rather than with a weighted sum of its neighbourhood. A median filter is a type of spatial filter that

replaces each pixel with the median of its operating neighbourhood. Inspector® provides a pre-defined median filter which operates on each pixel's 3×3 neighbourhood. It performs a non-linear filtering operation where a window moves over a signal and at each point the median value of the data within the window was taken as the output. Median filtering has some desirable properties that cannot be achieved with other filtering operations. The impulse response of the median filter is zero. This property makes it attractive in suppressing impulsive noise. Median filters are robust and are well suited for data smoothing when the noise characteristics are unknown. A stepwise change in a signal passes the median filter unaltered. This property is used in application such as image filtering, where data need to be smoothed, but blurring of the signal edges is not acceptable (Refer to Astola *et al*., 1990).

- A morphological opening operation was performed to remove small particles (e.g., bubbles in liquid films) or to break isthmuses or connections between touching objects. Inspector® provides the opening function to operate on 3×3 neighbourhoods taking all neighbourhood pixels into account. The closing operation is useful in filling holes in objects; however, in doing so, they also connect objects that are close to each other. The closing function also performs a standard 3×3 closing operation taking all neighbourhood pixels into account. Erosion and dilation operations were also used in some extreme cases with more blobs. Erosion peels layers from objects or particles, removing extraneous pixels and small particles from the image. On grey scale images, Inspector's® pre-defined erosion operation replaces each pixel with the minimum value in its 3×3 neighbourhood (if operating on bright objects) or with the maximum value (if operating on dark objects). Dilation adds layers to objects or particles, enlarging particles. On grey scale images, Inspector's® pre-defined dilation operation replaces each pixel with the maximum value in its 3×3 neighbourhood (if operating on bright objects) or with a minimum value (if operating on dark objects).
- Once the image had been pre-processed, film thickness measurements could be extracted by positioning markers at the gas-liquid interface using

Inspector's® edge detection features. The process of positioning these markers begins by specifying a search box. The size and position of the search box specifies the search area. Also the orientation of the search box has to be specified to ensure the proper search direction as shown in figure 3.8. The search box is positioned using the already-known wall location from the water meniscus pictures. The search takes place in the same direction as the search direction line. To obtain valid results, the box must include a portion of the edge and be completely inside the image. In addition, the edge should enter and leave by opposite sides of the box (occupy the entire box width). The box's location line can also be adjusted to indicate the expected position of the edge. To ensure the fastest possible search operation, the smallest possible search box is used; search time is roughly proportional to the area searched. In reality, the search box is just 1 pixel high. It is shown larger in figure 3.8 for more clarity. In addition to locating the edge and to measure its true width, the location line of the search box is set at approximately the same angle as the edge. This allows Inspector® to find the edges of the same orientation as the location line. However, the most accurate results are obtained when searching for an edge at 0° or 90°. The Inspector® finds the required edge using certain specified characteristics such as angle, polarity, strip width, reference position, edge strength, and contrast, etc.

- Figure 3.6 was taken at a flow rate Q = 4.678 L/min and Re = 974. Here, the liquid film is very thin and is characterised by small waves. The tube wall determined from the air-water meniscus pictures as discussed earlier is shown by a thin vertical yellow line on the extreme right- and left-hand sides. The features present in the falling annular film images are shown in figure 3.6. The object plane with the surface waves (viewed from the liquid side) is also depicted in figure 3.7. Figure 3.8 was taken at an even higher Reynolds number of Re = 4552. The search box, box width, search direction, and

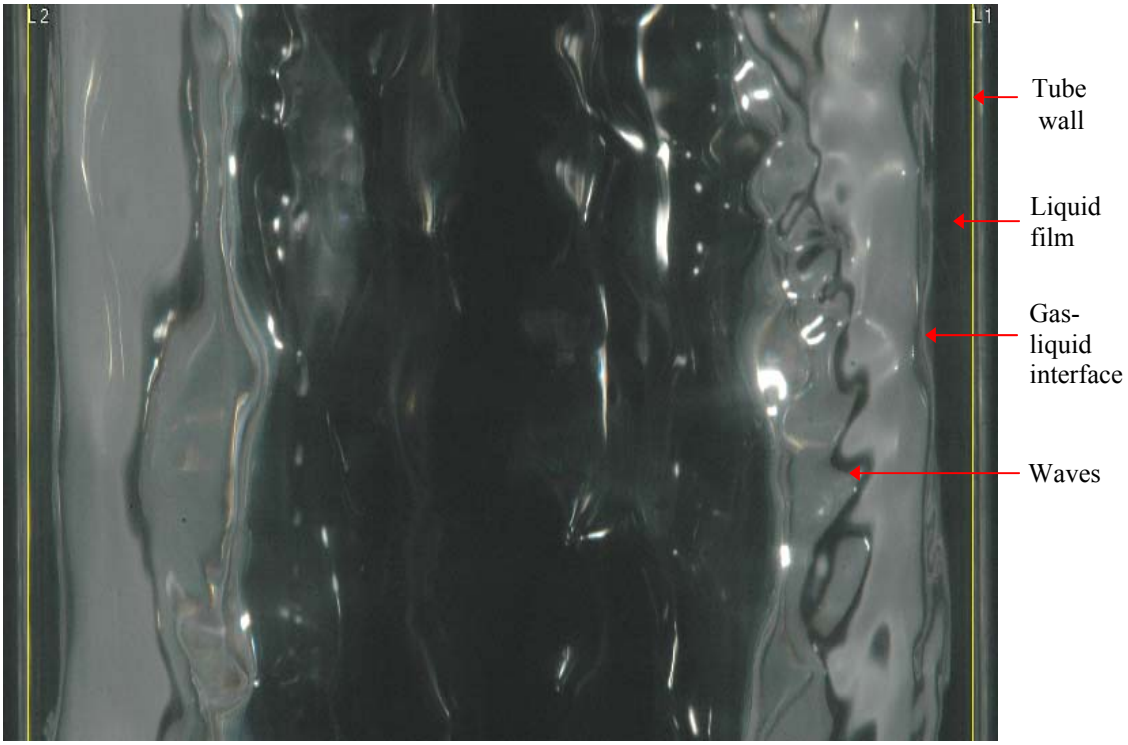

Figure 3.6: Falling annular film at Q = 4.68 L/min and Re = 974

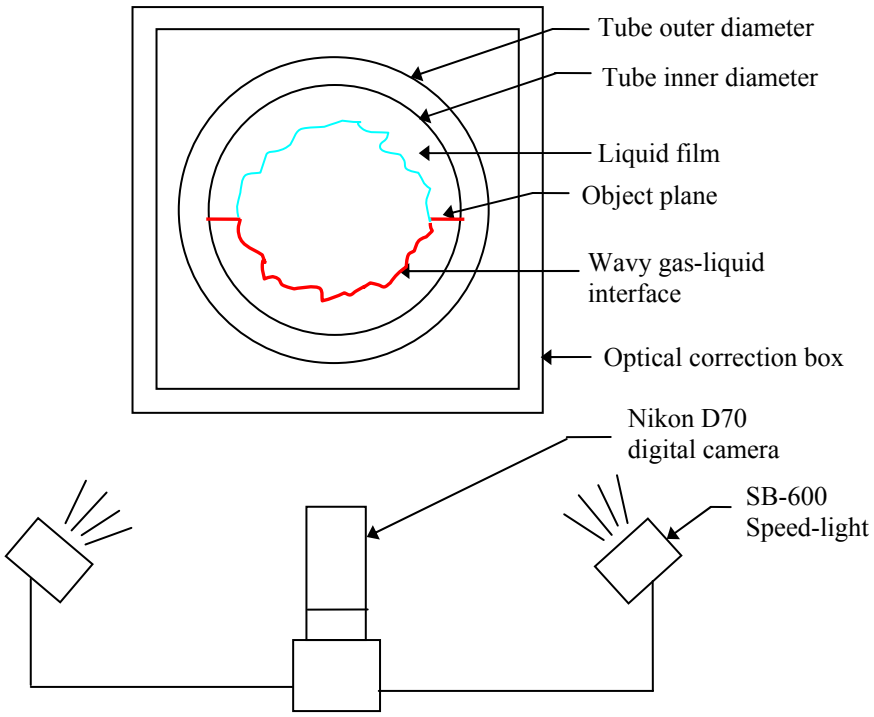

Figure 3.7: Cross-section view of a falling annular film

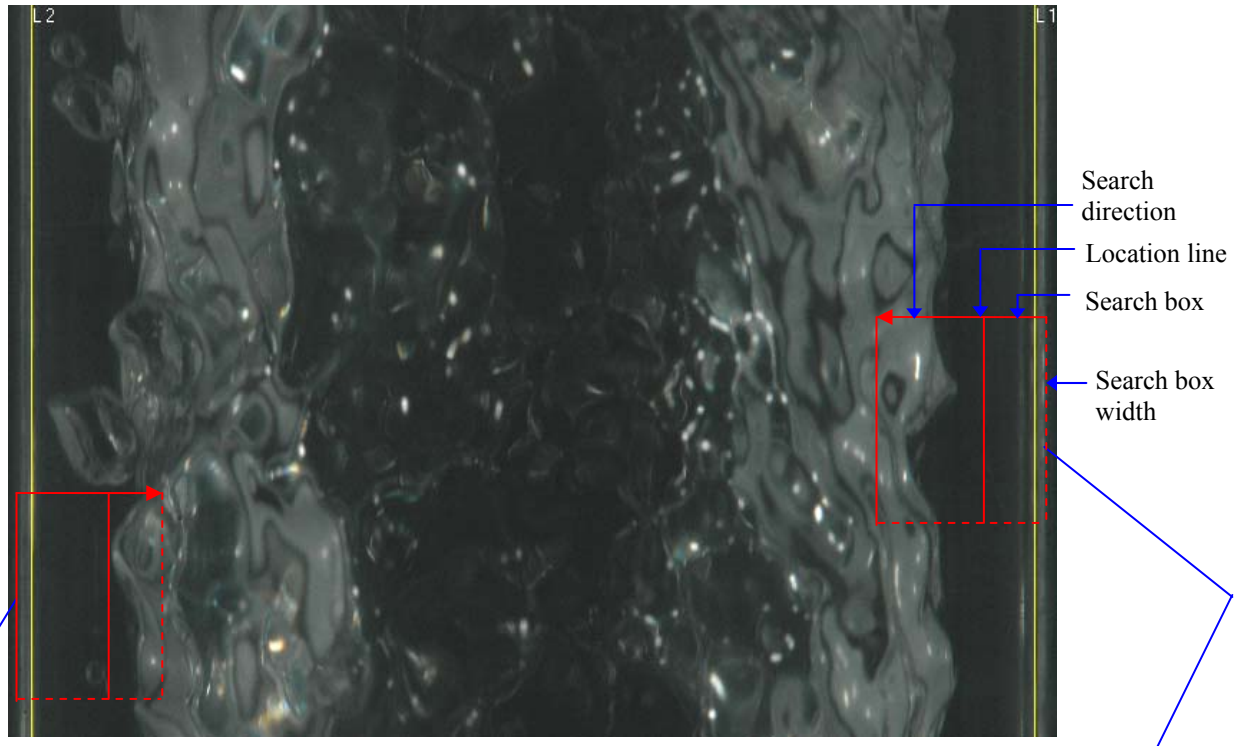

Figure 3.8: Falling annular film at Q = 21.86 L/min and Re = 4552

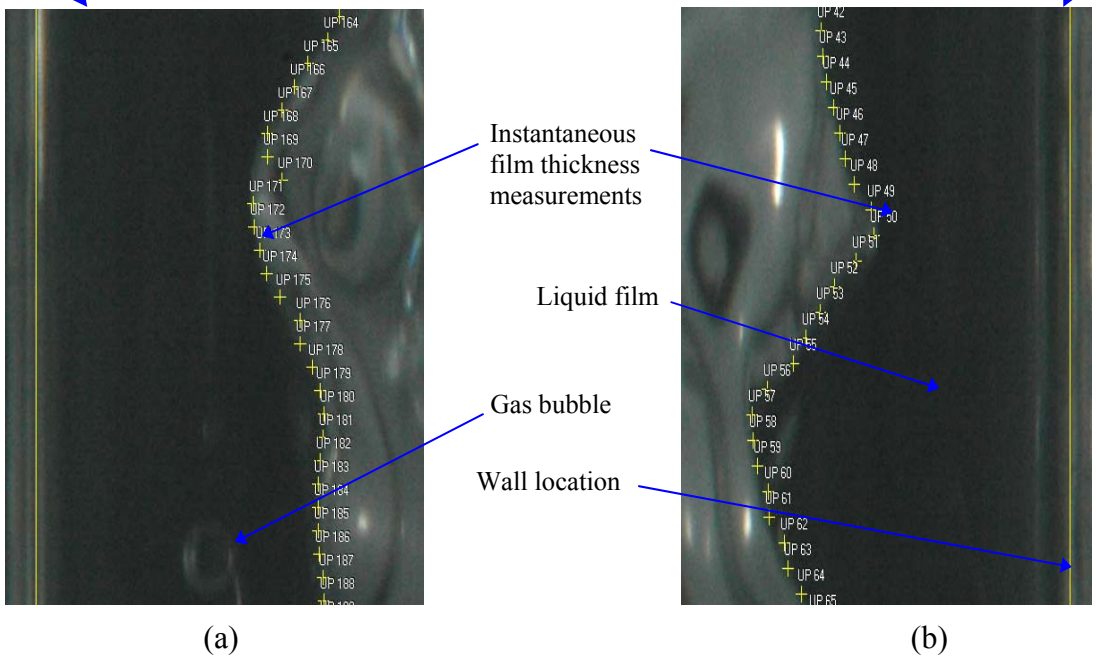

Figure 3.9: (a) Left side portion of the falling annular film with measurements, (b) Right side portion of the falling annular film with measurements

location line are also shown in figure 3.8. Figure 3.9a and 3.9b show a small portion of figure 3.8 with the measurements on the right- and left-hand sides extracted after carrying out all the image processing and analysis operations described. The vertical distance between each instantaneous film thickness measurement was equal to 20 pixels. Using edge detection techniques, Inspector® identifies the gas- liquid interface in these two-dimensional pictures as a characteristic of an edge. About 200 edge measurements were extracted from the left- and right-hand sides of each image.

- Finally, all of the operations just described were automated using the Inspector® scripting feature, allowing many instantaneous film thickness measurements to be made in a very short period of time. The script is recorded in Inspector® by performing the operations manually with the script recorder activated. Once the recording started, the sequence of operations was added to the script as a user-defined script function. A user-defined script function is simply a named group of script statements, which is referred to as a macro. To run the code autonomously, the script function was edited. A script can have several user-defined functions, as well as statements outside of these functions. Inspector® displays the script in a script window. The required modifications were typed directly in the script window, or the script was saved in a file and edited using a text editor. Later, powerful scripting constructs such as looping, comments, and macros were also manually added. These functions added more flexibility to the code during execution and enabled many quantitative instantaneous film thickness measurements to be extracted in a short period of time. The code for the measurement of instantaneous film thickness in annular falling liquid films was written using Inspector® (Refer to Appendix A.)

3.6 Correction of visual distortion

One of the most common problems in imaging flows in cylindrical tubes is the optical distortion caused by the wall curvature. To produce quantitative results using

photographic techniques, these optical distortions need to be minimised. This distortion occurs because of the combined effects of the curvature of the surfaces and differences in refractive indices of the interacting media. To minimise this problem the cylindrical tube must be surrounded by an optical correction box with flat walls filled with a matching fluid.

3.6.1 Arrangement of test section and optical correction box

For the case of internal flow through a tube, it is necessary to construct a box with flat walls (optical correction box) around the model. If the flowing liquid also has the same refractive index, the flow can now be viewed without refraction errors from directions perpendicular to each face of the view box. Bhatia *et al*. (1982) and Durst *et al*. (1988) used this method to conduct near-wall measurements in a turbulent pipe flow. In their experiments, the entire test section was submerged in a fluid with matched refractive index in a container with flat walls. Durst *et al*. (1988) also discussed methods for determining the laser Doppler velocimetry (LDV) measuring position relative to the wall when refractive index matching is employed. Duncan *et al*. (1988) used the optical-correction box method to study flow through elastic wall casts of aortic bifurcations where wall motions were present. Budwig *et al*. (1993) conducted flow studies through axisymmetric bulges in tubes using this method. The bulge models were machined from rectangular blocks of acrylic plastic. For external flows around solids with curved surfaces the view box becomes a fluid channel through which the matching fluid is pumped. Chen and Fan (1992) have used this method to investigate the flow structure in fluidised beds. Agrawal *et al*. (1978) and Bovendeerd *et al*. (1987) dealt with the refractive index problem by machining the circular tubes with rectangular outer walls and filling the tube with a fluid that matches the refractive index of the surrounding walls.

3.6.2 Properties of test section and correction box materials

Table 3.1 shows some of the common materials that are used to construct optical correction boxes and test sections. The important issues with regard to these materials are ease of model and test section construction, index of refraction, optical

clarity, scratch resistance, and price. Some projects might have special requirements such as models with flexible or porous walls. For this thesis, acrylic was chosen as the tube and correction box material due to its availability, price, and transparency.

Table 3.1: Properties of tube and correction box materials

Material	Model Construction methods	Index of Refraction	Scratch resistance	Comments
Glass				
Pyrex glass	glassblowing fusing	1.47 to 1.49	+ + +	Available in sheets, tubes, rods and special fittings
Optical glasses	grinding polishing	1.45 to 1.96	+ to + + +	Available in flats and lenses-expensive to purchase and to work with, Durst *et al*. (1988)
Plexiglas	moulding and extrusion	1.51		Exceptional optical clarity, chemical resistance, Gupta and Kaplan (1942)
Plastic				
Pre-cast or extruded	machining, bonding, bending, and polishing			Available in sheet, tubes, and rods
Acrylic		1.49	+	Less expensive, transparent and easy to fabricate
Polycarbonate (Lexan)		1.58	+ +	
Casting resins	can be machined after casting (except silicon)			
Silicon elastometer		1.43	+	Elastic walls, Duncan *et al*. (1990)
Urethane based		1.49	+ +	Cure at 65 ° C
Acrylic based		1.49-1.53	+	

3.6.3 Properties of matching fluids

Some of the considerations for successful use of matching fluids include index of refraction, optical clarity, density, viscosity, material compatibility, chemical

stability, safety, and price. Handbooks are very useful for selecting the matching fluids (Perry and Green, 1984). However, care must be taken because some of the liquids might be unsafe to work with or incompatible with typical flow loop materials. As seen from table 3.2, the closest match to acrylic (1.491) other than water (1.33) is glycerine (1.33-1.47), 80% sugar solution (1.490), mineral oil (1.490) and some organic liquids. Liu *et al*. (1990) used a mixture of turpentine and tetraline

Table 3.2: Properties of some fluids

	n	ρ/ρ_0	μ/μ_0	References and comments
Aqueous solutions				
glycerine	1.33-1.47	1-1.26	1-1.490	
Ethyl alcohol	1.36	0.79		
Sugar solution (80%)	1.49			
sodium iodide	1.5			Chen and Fan (1992)
Organic liquids				
Kerosene	1.45	0.82		Bovendeered *et al*. (1987)
Mixture of oil of turpentine and tetrahydronaphthalene (Tetraline)	1.49	~1	~1	Liu *et al*. (1990)
Mineral oil	1.48	0.85		
Turpentine	1.47	0.87	1.49	Budwig (1994)
Solvent naphtha	1.50	0.67		
Soybean oil	1.47	0.93	69	
Olive oil	1.47	0.92	84	
Vegetable oil	1.49			
Solvent				
Water	1.33		1	

(Note: ρ_0 and μ_0 are the density and viscosity of water at 20°C).

(1.490) whose density and viscosity were similar to those of water and that matched the refractive index of acrylic used in fabrication of the test section. Flows with variable refractive index have similar problems. While these methods may simplify the image analysis by reducing distortion, they also restrict the range of experimental exploration. For this thesis, water was chosen to be the working fluid because of its availability and other physical and chemical characteristics. Once the index of refraction problem was fixed, there was a need to eliminate the visual distortions.

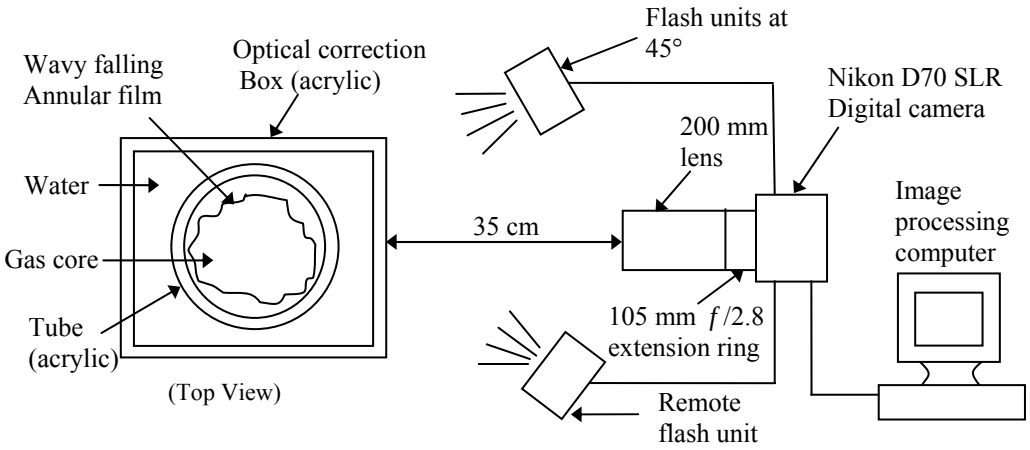

Figure 3.10: Arrangement of test section and optical correction box

After the test section material, correction box material, and the matching fluid were chosen, the test section and optical correction box were arranged as shown in figure 3.10. In this research, an optical correction box was placed around the tube and was made of the same material as the tube (acrylic). It was filled with the same liquid (water) as the test liquid. Since the index of refraction of the test liquid did not match the tube material exactly, further correction was required. A ray tracing model was developed for this purpose and will be discussed in detail in the next section.

3.7 Optical correction using ray tracing

In this section, the general purpose of the ray tracing diagram will be explained. Then a brief review of the work done by past researchers in this field will be discussed. Finally, the technique will be discussed in detail using ray tracing

diagrams and detailing all equations involved in the calculations. The experimental validation of the ray tracing procedure will be explained in detail later in section 3.8.

3.7.1 Ray tracing

An accurate determination of the shapes and positions of objects within a cylindrical tube requires an analysis of the bending of light rays at various interfaces. This process is governed by Snell's law of refraction which is as follows:

$$n_1 \sin \alpha_1 = n_2 \sin \alpha_2 . \qquad (3.1)$$

where, n is the index of refraction of the medium and α is the angle between a ray and the surface normal. The subscripts 1 and 2 refer to the two substances. Since it was difficult to track the rays close to the tube wall, a ray tracing approach had to be adopted. The specifics are given in detail in the next section. The ray tracing problem has been studied by Boadway and Karahan (1981) and Bicen (1982) in fluid flow investigations using laser-Doppler anemometry (LDA). Their analysis was limited to determining the intersection of two laser beams entering the tube from various angles. Durret *et al*. (1985) used ray tracing techniques to reduce the optical distortion and design corrective lenses to facilitate alignment of the laser beams. Later, Lowe and Kutt (1992) reconstructed the three-dimensional trajectories of particles in fluid flows and developed a method for measuring the co-ordinates of particles located inside a straight cylindrical tube by viewing it from two directions using cameras and digital imaging techniques. They showed that refraction through a cylindrical tube wall can generate phenomena such as hidden regions and multiple images.

In this thesis, both a theoretical and experimental approach to correct for the visual distortion was used. The imaging system was modelled as a simple pinhole camera for this purpose. The main objective was to map points on the image plane to points on the object plane. A backward ray-tracing method was adopted in which the rays were traced from the image plane to the object plane. The details of all the ray tracing equations and calculations will be described in the next section.

3.7.2 Ray tracing equations and calculations

The ray tracing geometry is shown in figure 3.11 for a typical ray passing from the pin hole camera through an optical correction box and finally entering the cylindrical tube. The pin hole aperture is situated at a distance of L_a from the optical correction box and the image plane is at a distance L_i from the pin hole. The tube has an inner radius R_w and outer radius R_0 and is constructed from a material (acrylic) with an index of refraction $n_2 = n_4 = 1.49$. The tube and optical correction box are filled with the working fluid (water) with index of refraction $n_1 = n_3 = 1.33$. The optical correction box around the test section is placed at a distance of L_w from the outside of the tube. The optical correction box is surrounded by air with index of refraction $n_5 = 1.00$.

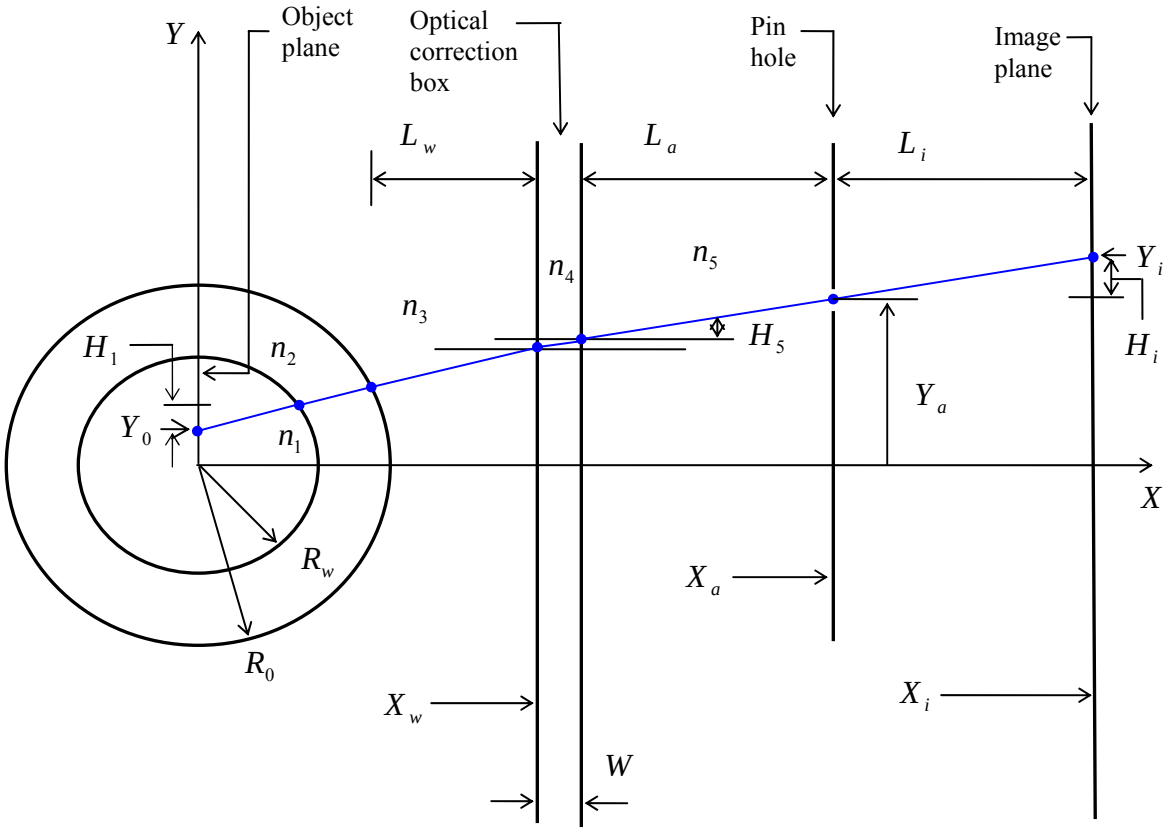

Figure 3.11: Ray tracing geometry for a straight cylindrical tube with an optical correction box and a pin hole camera

Horizontal distances are measured along the *X* coordinate and vertical distances are measured along the *Y* coordinate. The ray tracing procedure begins by selecting a point on the image plane at a position Y_i . The objective is to determine the corresponding location Y_0 on the object plane.

From figure 3.11 it can be seen that,

$$H_i = Y_i - Y_a \ . \tag{3.2}$$

This ray passes through the pin hole aperture and strikes the outside surface of the optical correction box.

Now consider only the wall of the optical correction box as shown in figure 3.12.

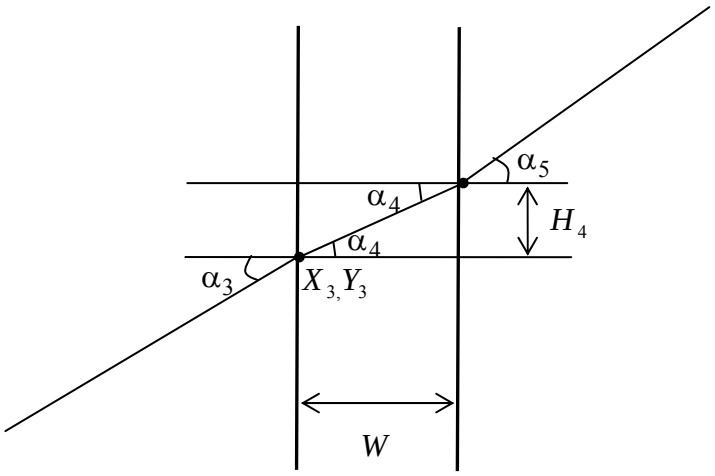

Figure 3.12: Ray-tracing through the optical correction box wall

The angle α_5 can be calculated from,

$$\tan(\alpha_5) = \frac{H_i}{L_i} . \tag{3.3}$$

The ray refracts as it enters the optical correction because of the change in the refractive indices. From Snell's law of refraction (see figure 3.12), one obtains:

$$n_5 \sin(\alpha_5) = n_4 \sin(\alpha_4) \qquad \text{(Outer boundary).} \tag{3.4}$$

$$\alpha_4 = \arcsin\left(\sin(\alpha_5)\left(\frac{n_5}{n_4}\right)\right) \tag{3.5}$$

As the thickness W of the optical correction box is known, H_4 is calculated as follows:

$$H_4 = W\tan(\alpha_4). \tag{3.6}$$

Then, applying Snell's law for the outer surface of the tube, the following result is obtained:

$$n_3 \sin(\alpha_3) = n_4 \sin(\alpha_4) \qquad \text{(Inner boundary).} \tag{3.7}$$

Knowing the values of the refractive indices n_3 and n_4 and the angle of refraction α_4, the value of α_3 can be determined.

Now, knowing the slope m_3 and the point on the left surface of the optical correction box (X_3, Y_3), the intersection point with the outer tube (X_2, Y_2) can be determined. The intersection between the ray and the outer surface of the tube (point 2) is as shown in figure 3.13.

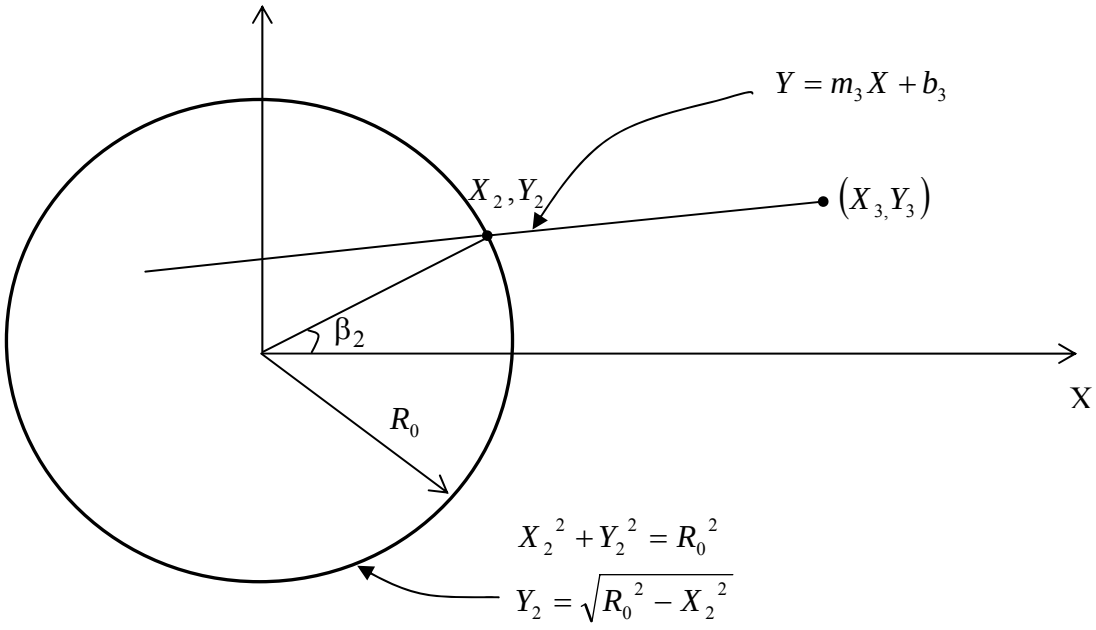

Figure 3.13: Intersection between a ray and the outer surface of the tube

The equation for the intersection point between a straight line and a circle can be found from,

$$m_3 X_2 + b_3 = \sqrt{\left(R_0{}^2 - X_2{}^2\right)}. \tag{3.8}$$

This equation can be re-arranged to the following form,

$$m_3{}^2 X_2{}^2 + 2 m_3 X_2 b_3 + b_3 - R_0{}^2 = 0\,. \tag{3.9}$$

Therefore,

$$X_2 = \frac{-m_3 b_3 \pm \sqrt{m_3{}^2 b_3{}^2 - \left(m_3{}^2 + 1\right) \times \left(b_3{}^2 - R_0{}^2\right)}}{\left(m_3{}^2 + 1\right)}\,. \tag{3.10}$$

where the greater solution of X_2 is of interest.

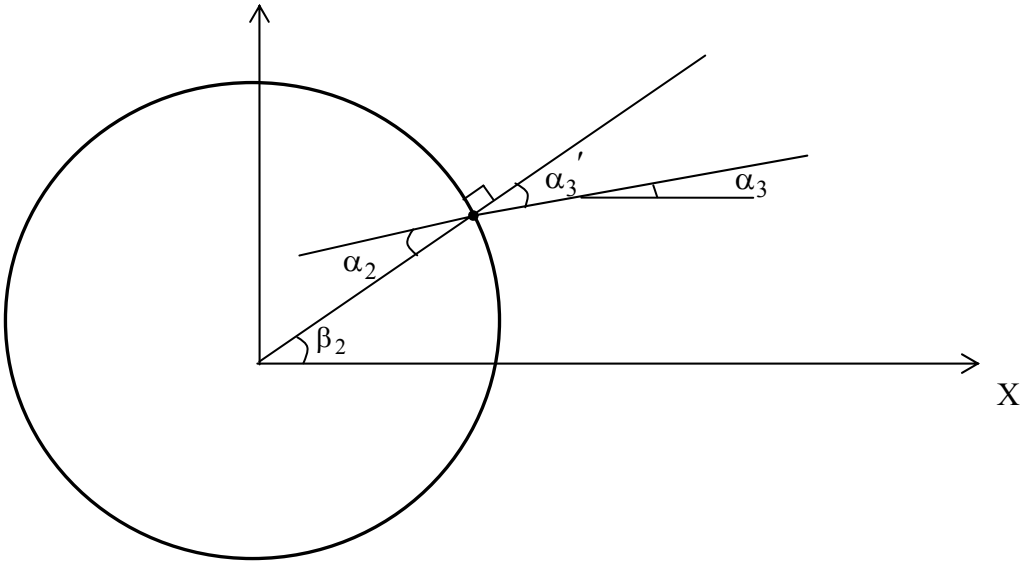

Figure 3.14: Snell's law for the outer surface of the tube

Knowing the values of the refractive indices n_2 and n_3 and the angle of refraction $\alpha_3{}' = \beta_2 - \alpha_3$, the value of α_2 can be determined.

Applying Snell's law of refraction for the outer surface of the tube (figure 3.14) gives

$$n_2 \sin\left(\alpha_2\right) = n_3 \sin\left(\alpha_3'\right) \text{ and} \tag{3.11}$$

$$\alpha_2 = \arcsin\left(\sin\left(\alpha_3'\right)\left(\frac{n_3}{n_2}\right)\right). \tag{3.12}$$

The same procedure is repeated for the inner radius of the tube as shown in figure 3.15. Knowing the slope m_2 and the intersection point with the outer tube (X_2, Y_2), the intersection point with the inner tube (X_1, Y_1) can be determined. Then, applying Snell's law again for the inner surface of the tube, the following result is obtained:

$$n_1 \sin(\alpha_1) = n_2 \sin(\alpha_2'). \qquad (3.13)$$

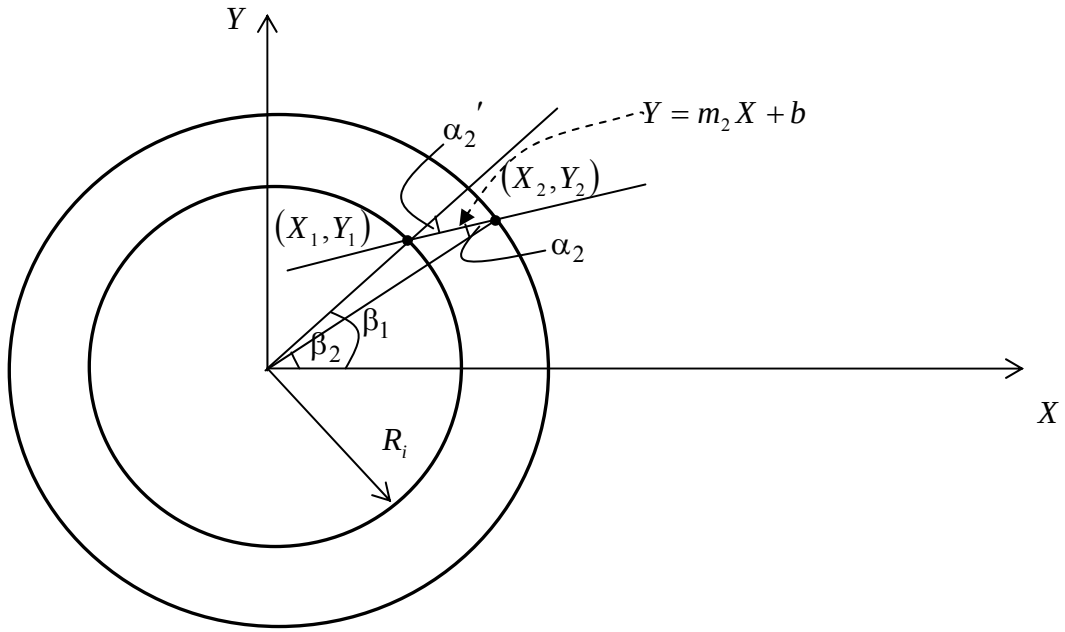

Figure 3.15: Intersection of a ray with the inner surface of the tube

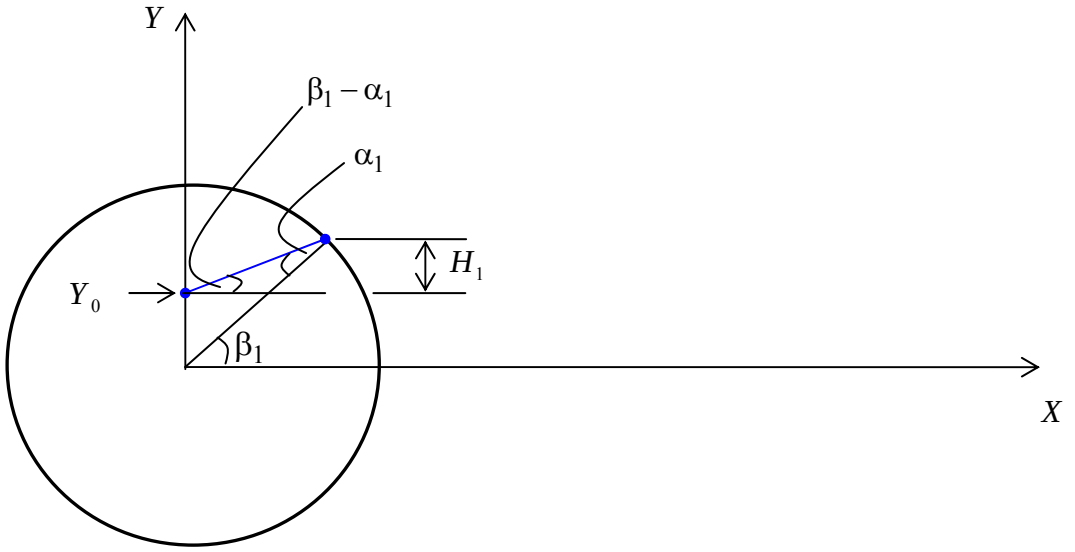

Figure 3.16: Ray refracted inside the inner surface of the tube

Knowing the values of the refractive indices n_1 and n_2 and the angle of refraction α_2', the value of α_1 can be determined.

Finally from figure 3.16, H_1 is calculated as follows,

$$H_1 = X_1 \tan(\beta_1 - \alpha_1). \qquad (3.14)$$

Using the value of H_1, the object distances Y_0 can be calculated. This process is repeated for many points on the image plane.

3.7.3 Computer-generated ray tracing diagrams

The ray tracing equations were programmed and solved using Microsoft® Excel. Computer-generated ray tracing diagrams are shown in figure 3.17a, 3.17b and 3.17c for three cases at different locations from the edge of the tube towards the tube centre. For simplicity, only a portion of the vertical tube and the optical correction box is shown. The geometry and refractive indices correspond to the experimental conditions of this thesis. Some of the fixed parameters involved in the calculations are given below in Table 3.3. The ray was automatically traced from the image plane back to the object plane from where it originated. It is seen that the refractive angles become larger near the edges of the tube (figure 3.17a). In practice, points near the edge become difficult to observe partly because of distortion but also because of irregularities in the surface of the acrylic tube. Towards the centre, the refractive angles become smaller (figure 3.17b).

Table 3.3: Some fixed parameters involved in ray-tracing calculations

Parameter	Distance (mm)
Y_a	15
R_0	15.82
R_w	12.74
L_w	15.93
L_a	1000
L_i	100
W	3.175

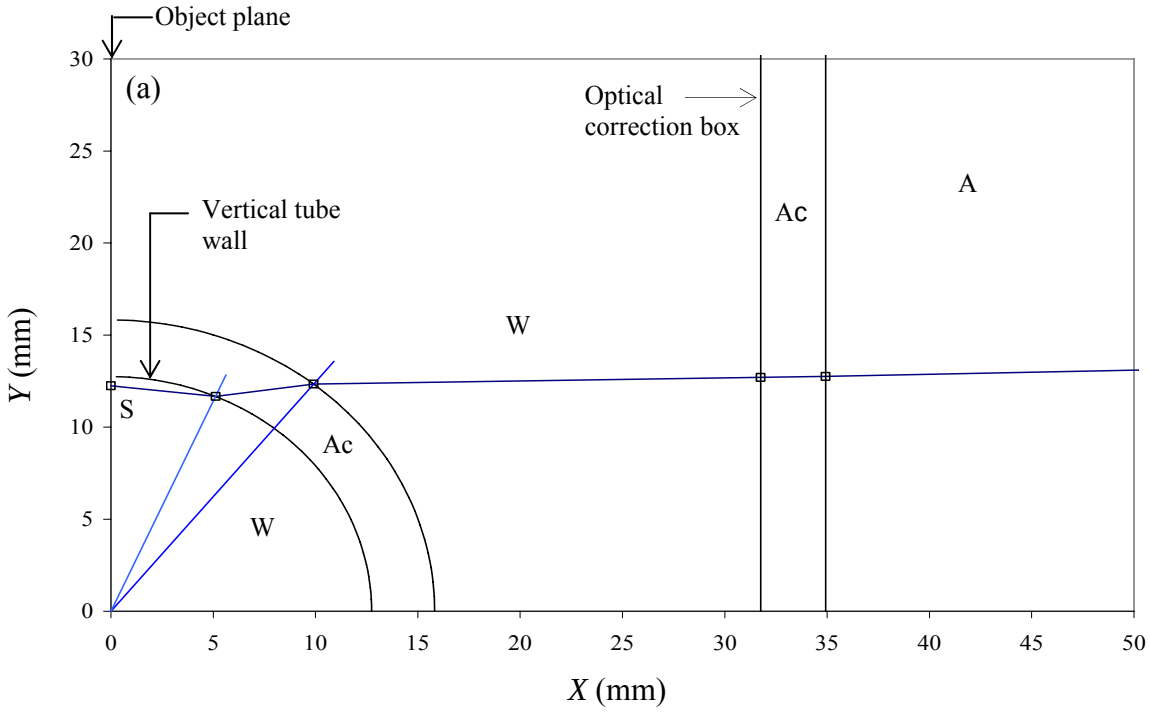

S = Point source A = Air (n =1.00)

W = Water (n=1.33) Ac = Acrylic (n =1.491)

Figure 3.17 (a): Ray traced very close to the tube wall

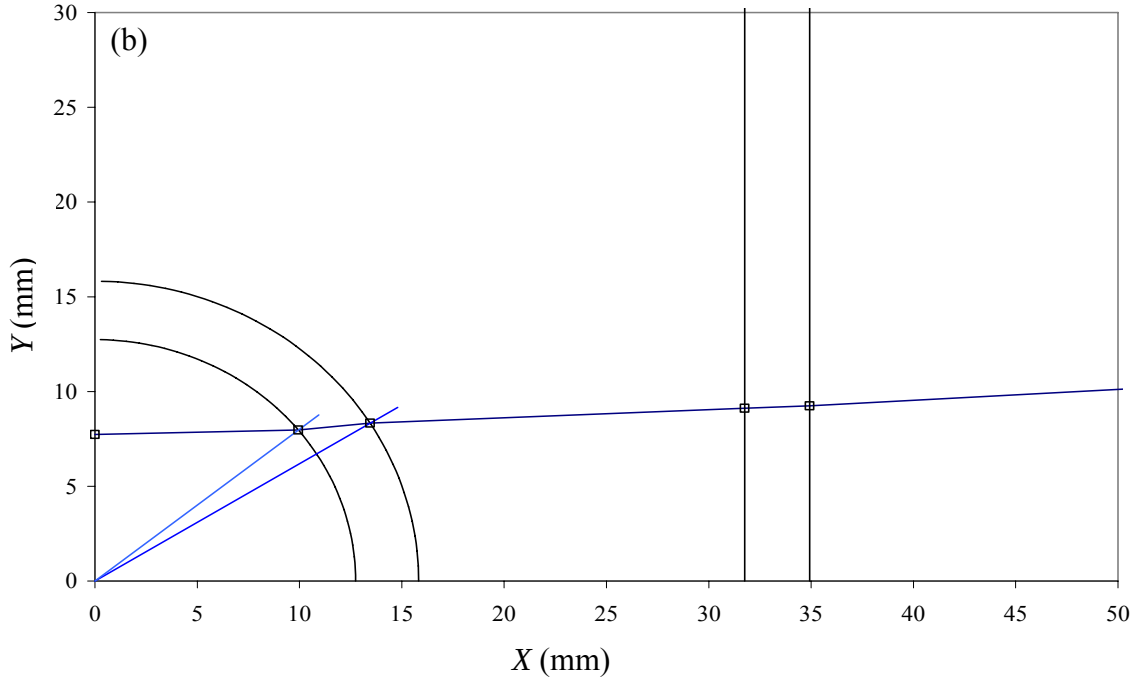

Figure 3.17 (b): Ray traced mid-way between the tube wall and the centre of the tube

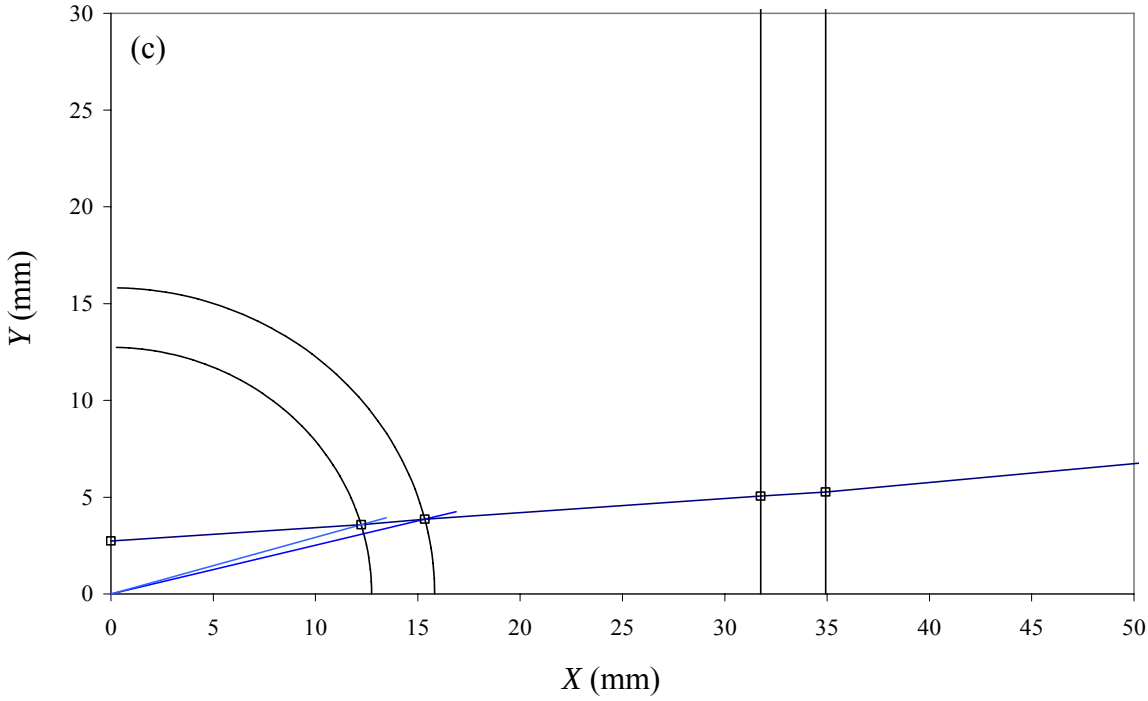

Figure 3.17 (c): Ray traced close to the tube centre

Finally, near the middle of the tube, the image distance is almost proportional to the object distance (figure 3.17c). Thus an object located in the middle would appear to be relatively undistorted when viewed from the outside.

The individual ray tracing results can be used to develop a relationship between the actual and apparent film thickness. The film thickness in the object plane is the actual film thickness. The apparent film thickness is obtained from the image plane using a simple image calibration. The film thickness (in pixels) is determined from the wall location and gas-liquid interface markers. This is converted to mm using a scale factor determined from the two wall locations (in pixels) and the known inner diameter of the tube. One consequence of this procedure is that, regardless of the distortion near the wall, the optical distortion error in the film thickness measurement goes to zero as the film thickness goes to zero. This is because the wall position in the images is explicitly used in the measurement procedure. Also, the distortion is

zero at the tube centreline because the rays are normal to all surfaces. This case, however, is of no practical importance since the films are never that thick.

Figure 3.18 shows the distortion error as a function of the apparent film thickness. Without the optical correction box, there is substantial distortion near the edge of the tube. The distortion reaches a maximum of 0.6 mm for 3 mm thick films. However, when liquid (water in this case) is put in the optical correction box; the distortion greatly reduces. The distortion near the edge of the tube means that film thicknesses appear smaller than they actually are. The distortion is reduced even though the index of refraction of water is much different than acrylic. Experimental data is required to validate that this method could effectively correct for distortion.

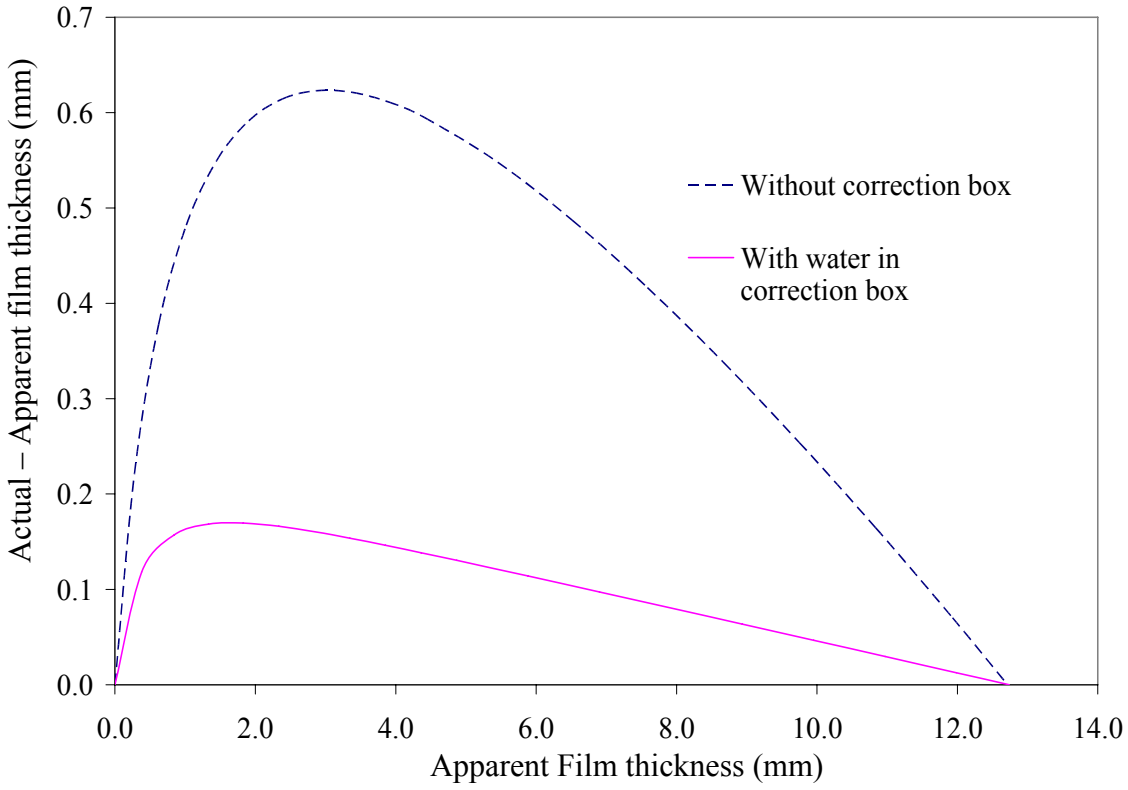

Figure 3.18: The effect of using water in the optical correction box as determined by the ray tracing model

3.8 Experimental confirmation of ray tracing procedure

The experimental investigations of optical distortion carried out in the test section are presented here. The in-situ calibration procedures that were carried out to determine the effect of distortion caused by the tube wall when light rays get refracted near the edges are explained. Finally, the experimental results obtained were compared with the ray tracing model.

3.8.1 Description of the calibration stylus and holder

A picture with the calibration stylus and the stylus holder flushed with the tube wall can be seen in figure 3.19. The tube wall is shown by a thin vertical line on right side of the picture. The calibration stylus and stylus holder were designed to position a calibration target in the object plane inside the water-filled tube (see figure 3.20). An enlarged view of the stylus used in the calibration is also shown in figure 3.21. The

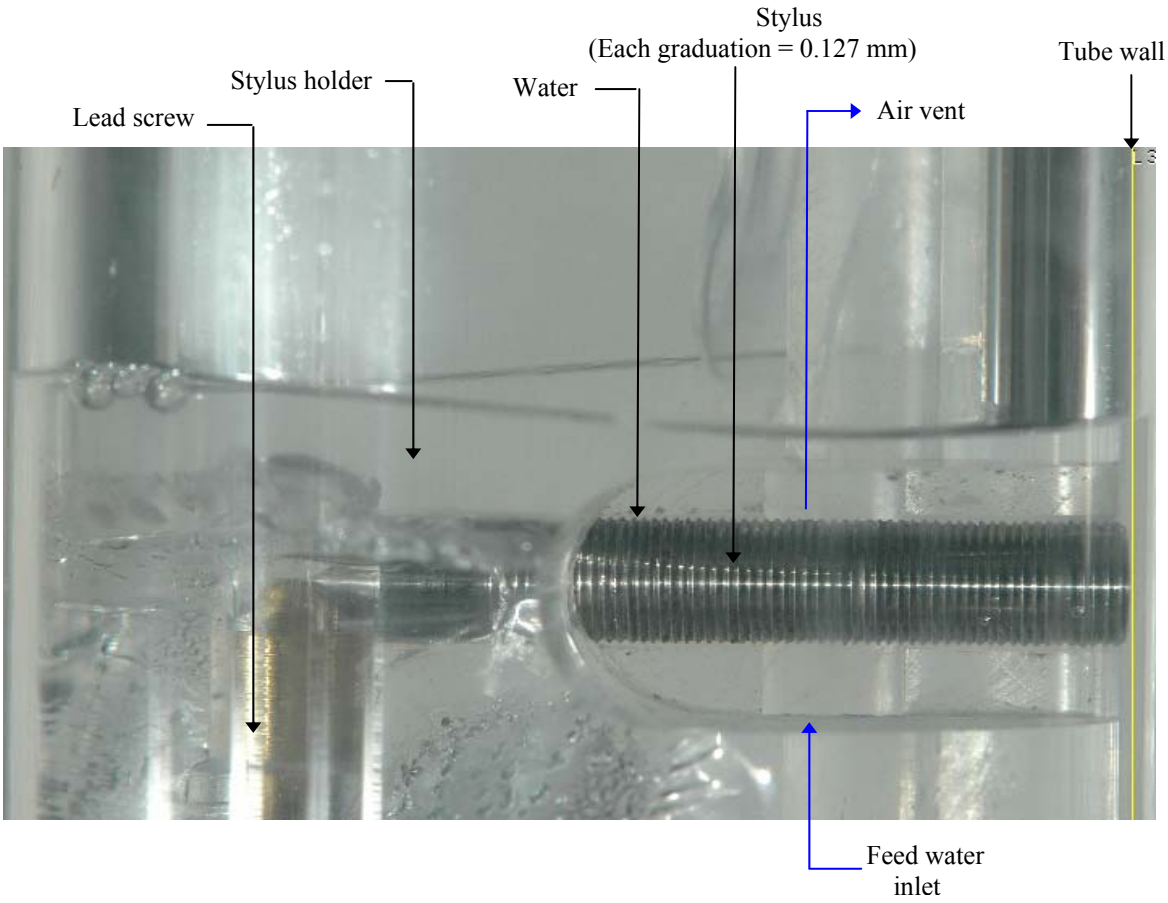

Figure 3.19: Picture of the stylus flush with the vertical tube wall

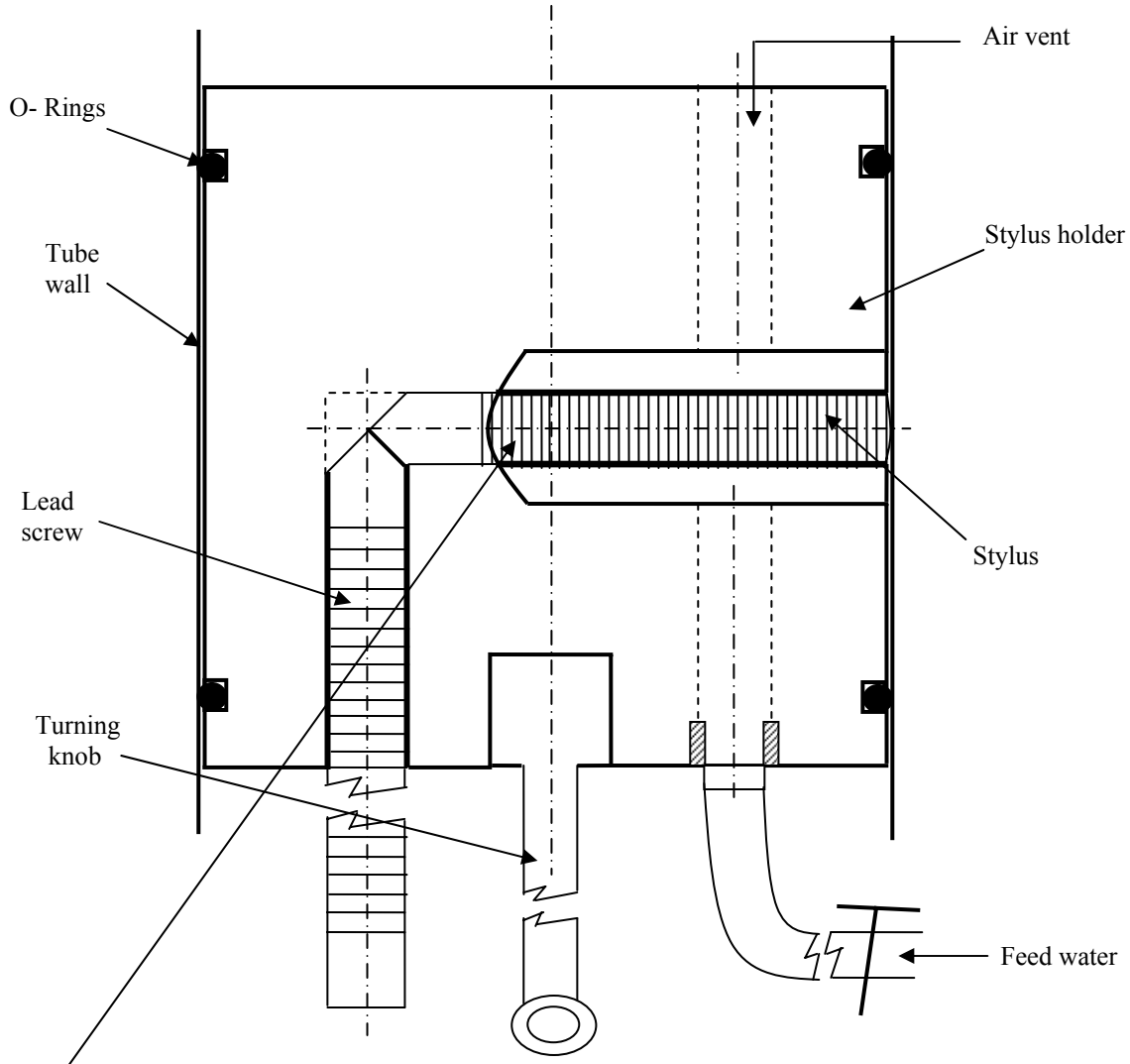

Figure 3.20: Front view of the in-situ calibration setup

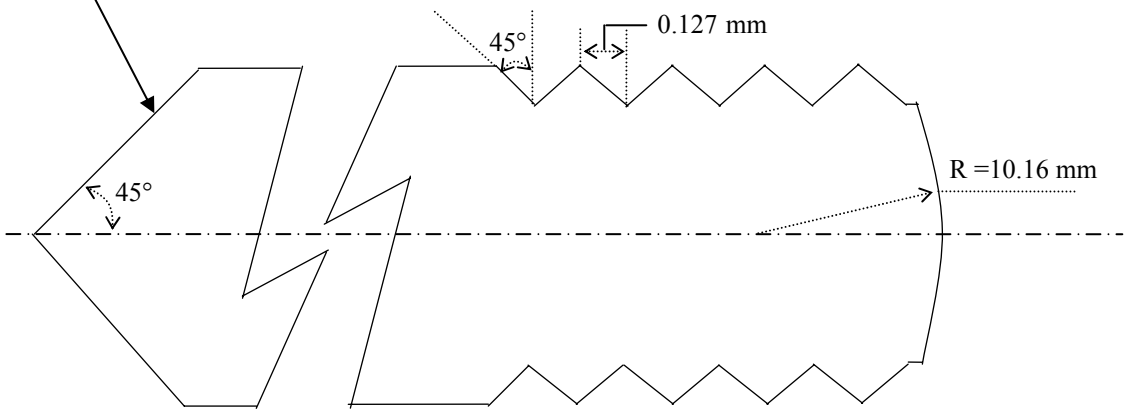

Figure 3.21: Enlarged view of the stylus

stylus was made of brass with fine grooves cut in it. The distance between the crest and the trough of each groove is 0.127 mm. The stylus holder was made of acrylic and it contains the stylus, the lead screw, turning knob, and the feed water circuit. As the lead screw is advanced in the slot, it moves the stylus to contact the inner tube wall. The small region containing the stylus is flooded with water. The region around the stylus was flooded to mimic the actual conditions during testing. Air was vented through the top to remove any unwanted bubbles in the region.

3.8.2 Comparison of experimental results to ray tracing model

The pixel number corresponding to each graduation (i.e., the crest and the trough of each groove) in the stylus was recorded. As per the ray tracing theory, the distances between graduations near the centre of the tube should not be deformed when viewed through the correction box filled with water. Therefore, if there was no visual distortion, the pixel to stylus graduation ratio was constant throughout the whole picture, meaning that the near wall graduations were not deformed. But very near to the wall, it was found that the stylus graduations seemed to be deformed or closer to one another. This observation near the wall was consistent with the ray tracing theory.

Figure 3.22 shows the (Actual - Apparent film thickness) as a function of apparent film thickness. The experimental results appear to be in reasonable agreement with the theoretical results near the tube wall and up to a film thickness of about ~ 6 mm. This value of film thickness is thicker than the expected films of 1 ~ 2 mm. The reason for the slight deviation from the theoretical curve beyond these points could not be determined. Small variations in the wall thickness of the acrylic tube may have contributed to this error. Figure 3.23 shows the relationship between the percentage error and the apparent film thickness. As predicted by the theory, there is distortion as the light rays get refracted near the tube wall. But the percentage error goes to zero as apparent film thickness goes to zero. This is because the deviation between the actual film thickness and the apparent film thickness approaches zero near the tube centre. The experimental results for film thickness agree closely to

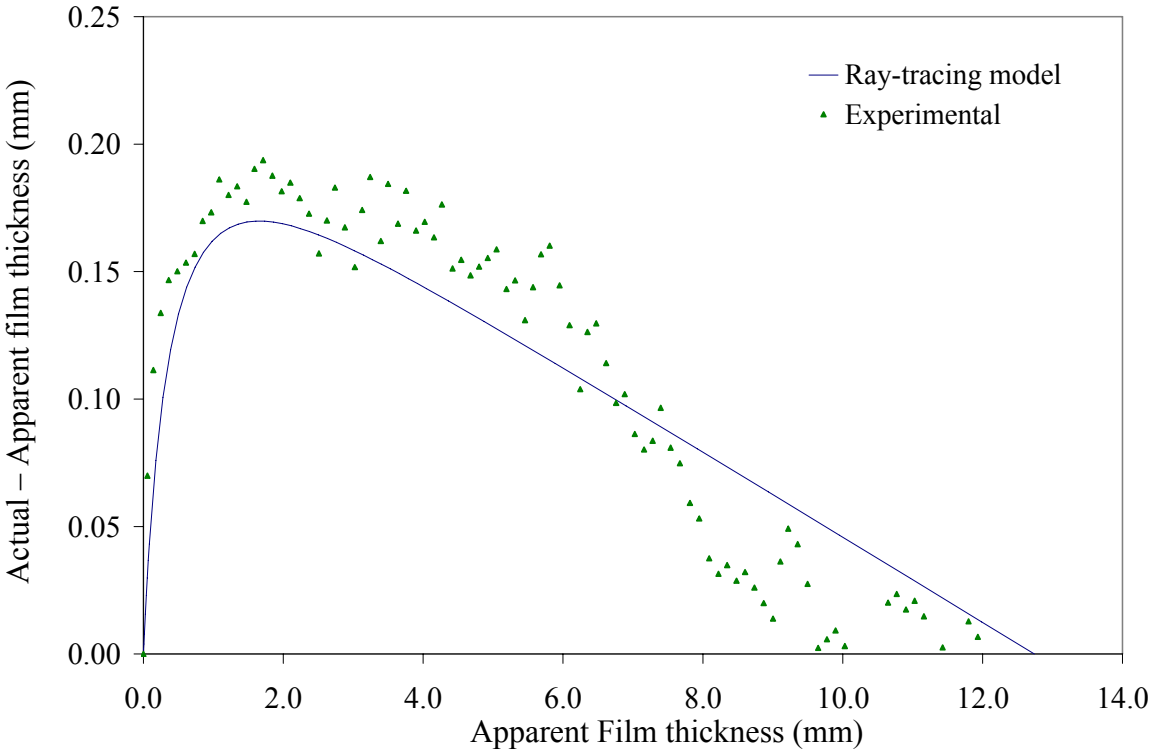

Figure 3.22: Comparison of experimental and theoretical results for ray-tracing

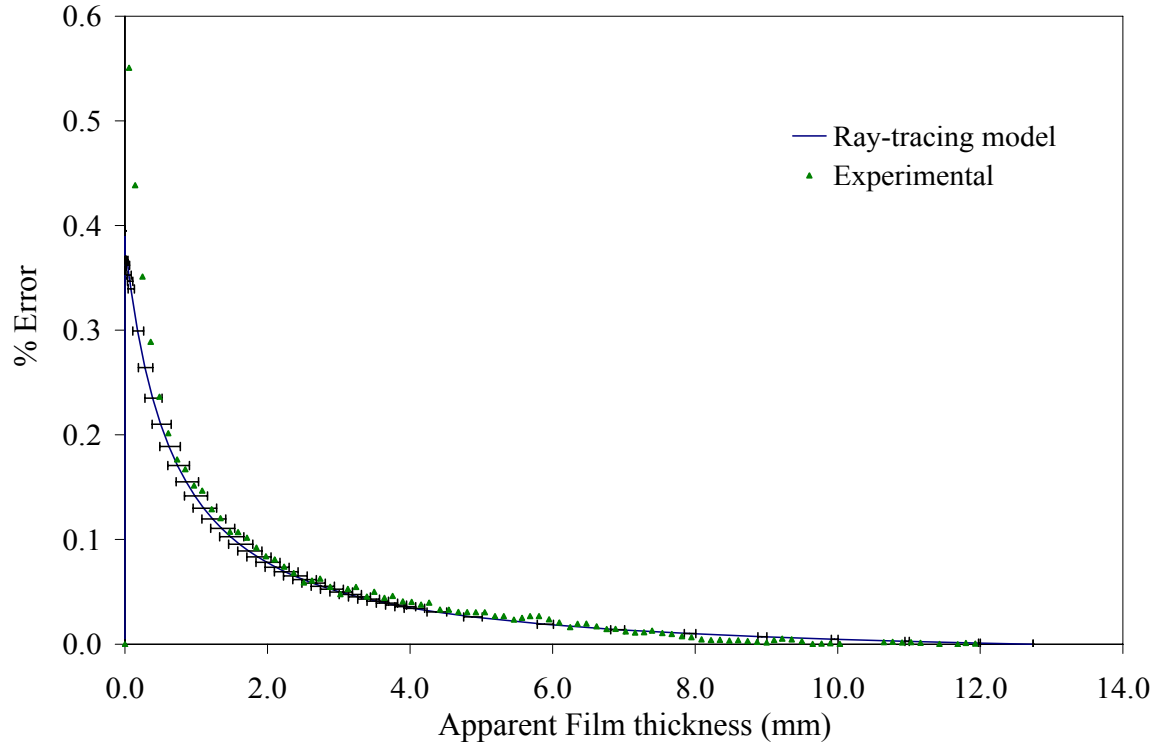

Figure 3.23: Percentage error versus apparent film thickness

within ~ ±1% with theoretical results for thinner and thicker films. Thus, it was concluded that ray tracing techniques and the calibration procedures employed here would increase the accuracy of the non-intrusive imaging technique and yield quantitative film thickness measurements inside the cylindrical tube. This method can be applied to any optical apparatus involving containers with cylindrical walls.

CHAPTER 4
RESULTS AND DISCUSSION

4.1 Introduction

In this chapter, qualitative observations on falling annular films are made. The instantaneous film thickness data and the dependence of statistical properties of the film thickness on liquid Reynolds number will be presented. The statistical parameters will be compared with other investigators' work.

The non-intrusive imaging technique described in Chapter 3 was successfully implemented to make localised film thickness measurements in a falling annular film at high Reynolds numbers. Some of the digital images will be presented here. These images provide quantitative film thickness measurements and also a qualitative picture of the turbulent characteristics of the falling annular film. The main advantages of this technique are that it leaves the flow undisturbed and is independent of elusive factors such as liquid hold-up and contact hysteresis which influence other techniques. The instantaneous film thickness data used the ray tracing technique described in the previous chapter to reduce the optical distortion. This technique improved the accuracy of the film thickness measurements.

4.2 Qualitative observations of falling films

In this section, some very interesting qualitative observations of turbulent wavy film flow are presented. Perhaps, one of the most interesting features of film flow is the wavy patterns which appear at free surface of the flowing film.

The flow cannot be continuously examined because the framing rate is not high enough. Many features of the flow may be present in one image, but not in the subsequent image. However, the images did provide a general indication of the gas-liquid interface structure. The images presented here are typical for the flow rates indicated. Figure 4.1 and 4.2 are examples of images taken at Reynolds numbers of Re = 2111 and Re = 3337. These figures clearly indicate the general trends in liquid film thickness variations with Reynolds number. The degree of waviness in the falling liquid film increases as the Reynolds number is increased. The random nature of falling liquid films evident in these images is a result of the three-dimensional gas-liquid interface characterised by waves of different sizes. Some observations on waves were also made by Taylor *et al*. (1963) for the case of upward co-current annular two-phase flow of air-water mixtures. Coincidentally, they also used a photographic technique to study the motion and frequency of the large disturbance waves. The wave crests slowly showed a tendency to split or overtake each other.

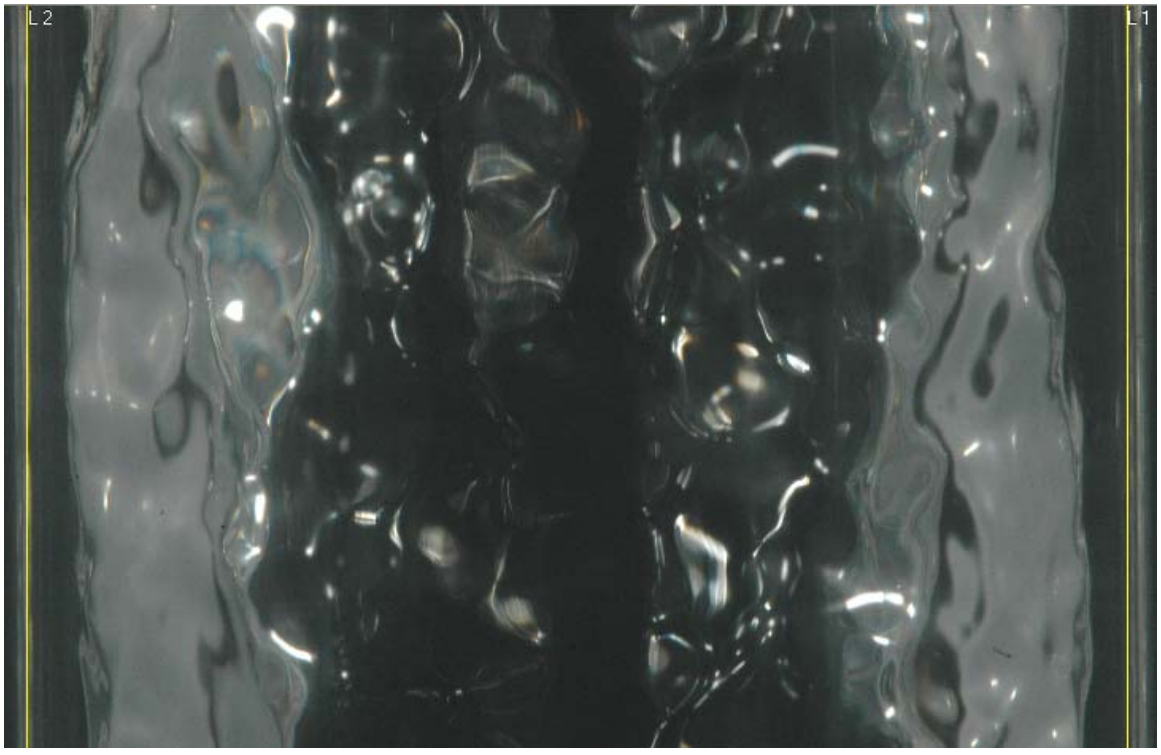

Figure 4.1: Falling annular film at Q = 10.68 L/min and Re = 2111

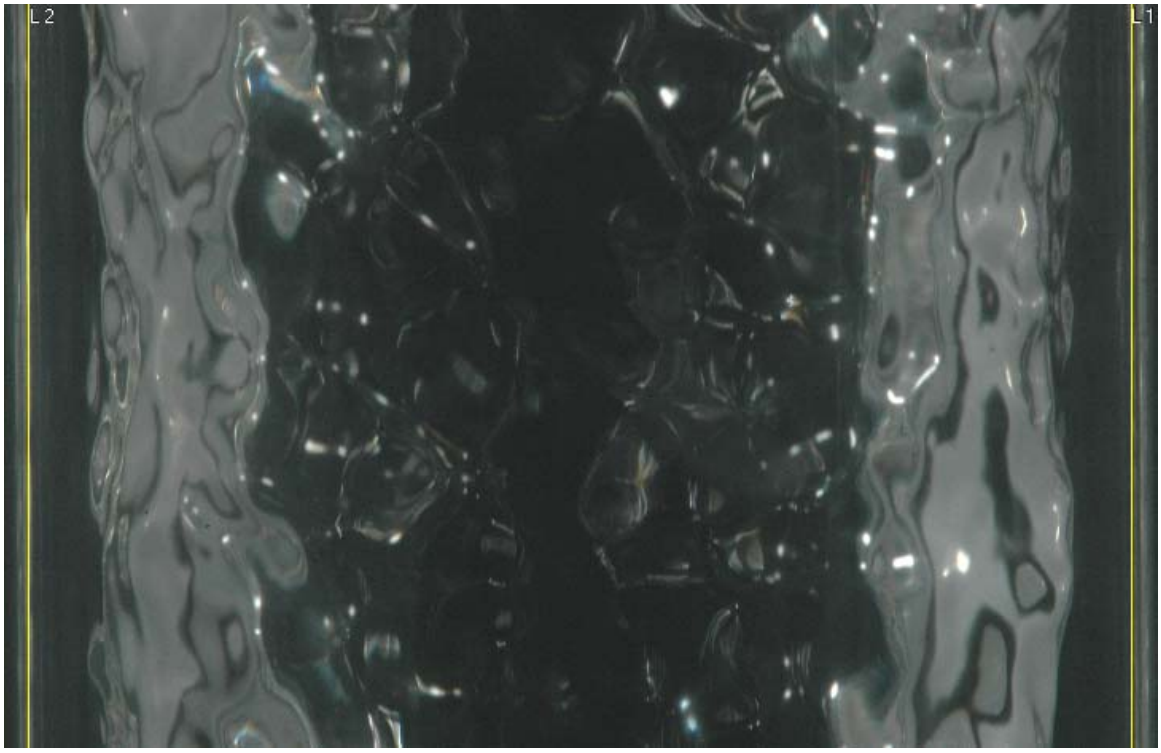

Figure 4.2: Falling annular film at Q = 16.03 L/min and Re = 3337

However, no comparisons can be made since they studied upward co-current gas-film flow. Also, they could have obtained such observations at lower Reynolds numbers, because the presence of a gas stream could have increased the size and randomness of the waves on the film surface (Fulford, 1964). Figure 4.3 was taken at a higher Reynolds number of Re = 4552. The waves become very irregular, and the wave cross section is very non-symmetrical. Bubbles begin to appear in the liquid film at these higher flow rates as seen in figure 4.3. In other words, the transitional flow can be termed as a 'bubbly' falling annular film. These bubbles could enhance convective heat transfer between the liquid film and the walls of the tube and can be important in two-phase heat transfer applications. The bubbles certainly represent an interesting feature of the falling annular film. Since the study was confined only to the liquid films, no attempt was made to make measurements of the mean bubble diameter or the rate at which they occurred inside the liquid film. Also there may be liquid droplets entrained in the gas-core region observed in these

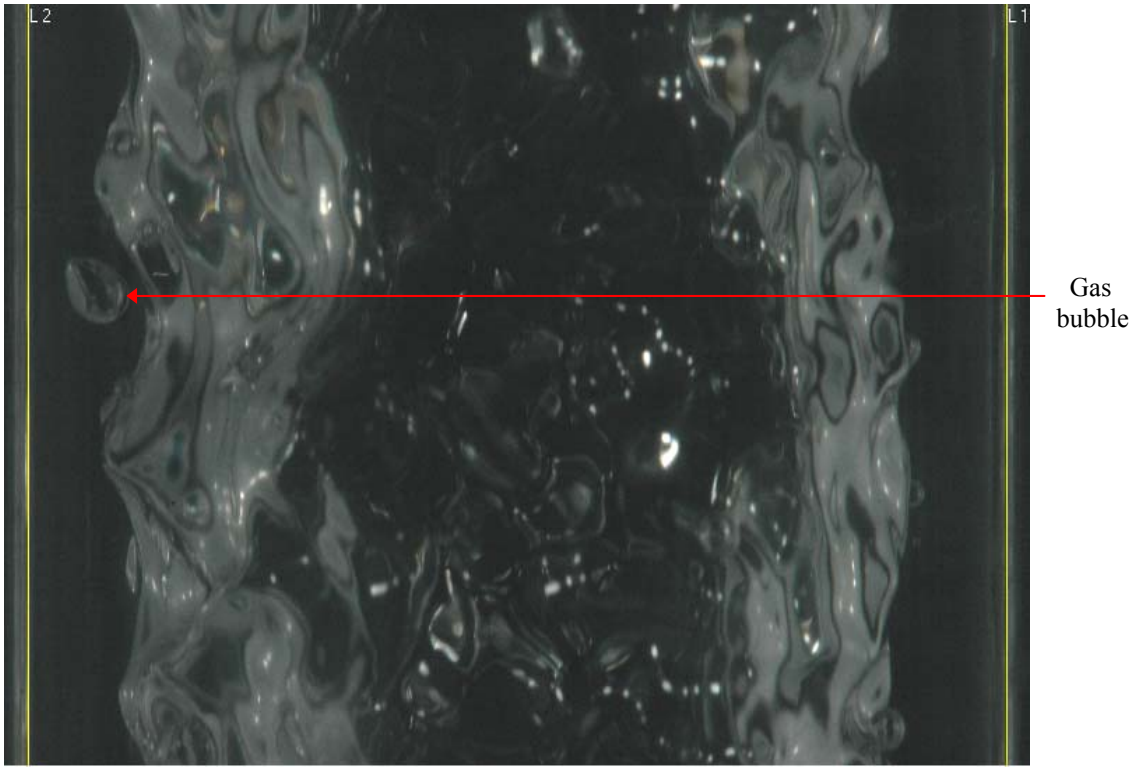

Figure 4.3: Falling annular film at Q = 21.86 L/min and Re = 4552

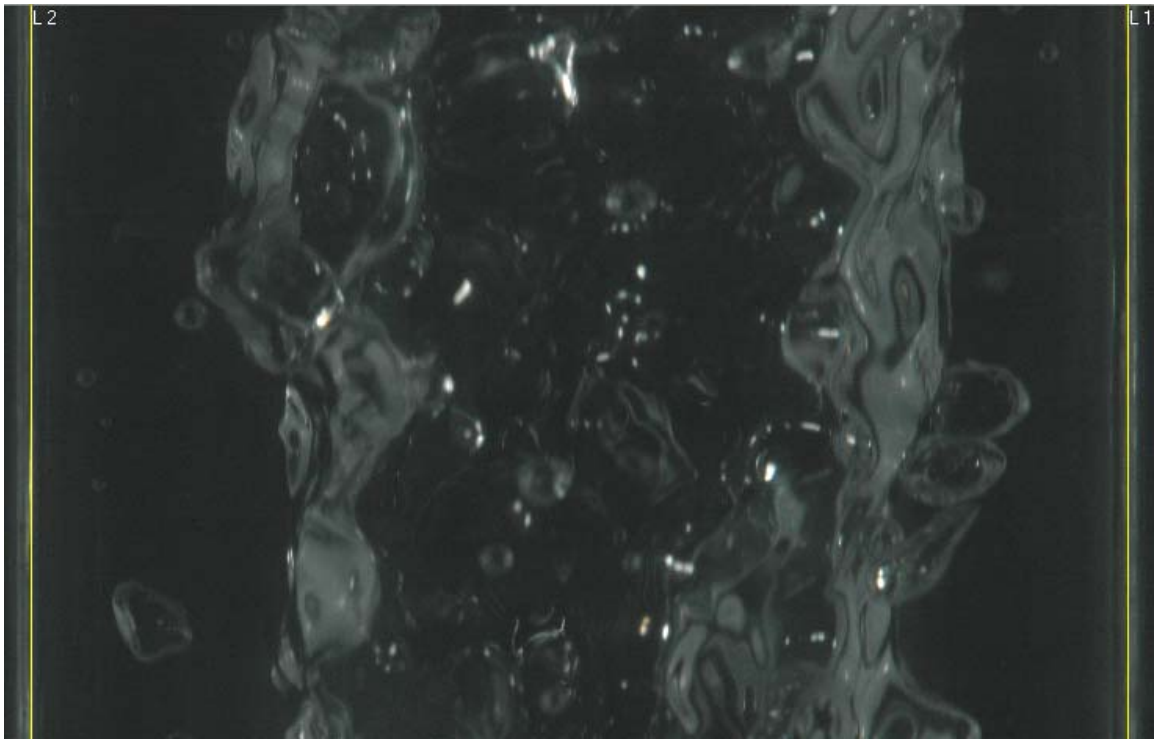

Figure 4.4: Falling annular film at Q = 21.86 L/min and Re = 4552

regimes. Figure 4.4 again shows another picture of a falling annular film taken at *Re* = 4552. The gas-liquid interface is extremely wavy and the film also looks very thick at these flow rates. The waves become so randomly mixed that the individual wave fronts can scarcely be distinguished. The surface waves appear to be covered with a mass of jagged turbulent waves. It is worth mentioning here that some flash photographs of this type of wave pattern for flow over a vertical plate have been published by Dukler and Bergelin (1952) in the lower turbulent regimes (*Re* = 400).

Generally thicker films occur at a Reynolds number of *Re* = 5924 as seen in figure 4.5 and 4.6. They indicate more intense turbulence but the same overall type of flow. Such observations were also made by Belkin *et al*. (1959). No definite wave patterns could be established, but the turbulent waves appeared to be similar in appearance to very large breaking ocean waves driven by cyclonic storms or strong winds. Belkin *et al*. (1959) referred to these waves as trochoidal waves generated by wind on large bodies of water. The rates of occurrence of these waves increased with increasing

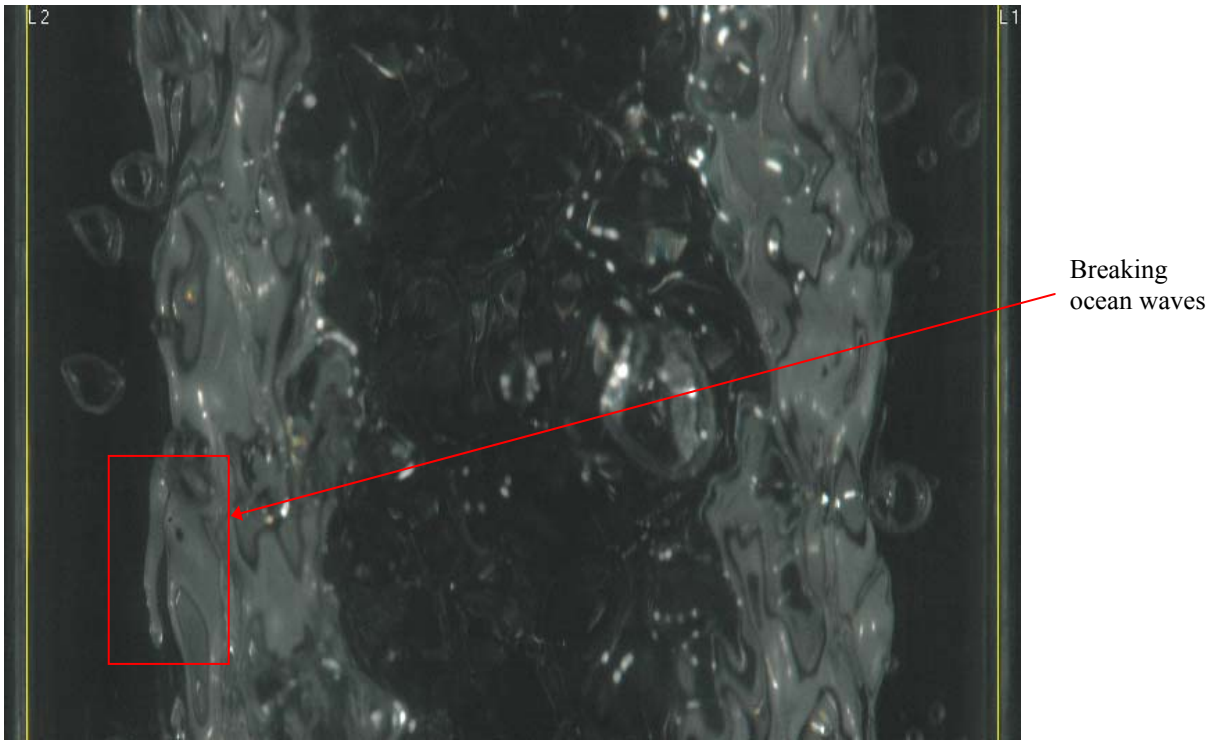

Figure 4.5: Falling annular film at *Q* = 28.45 L/min and *Re* = 5924

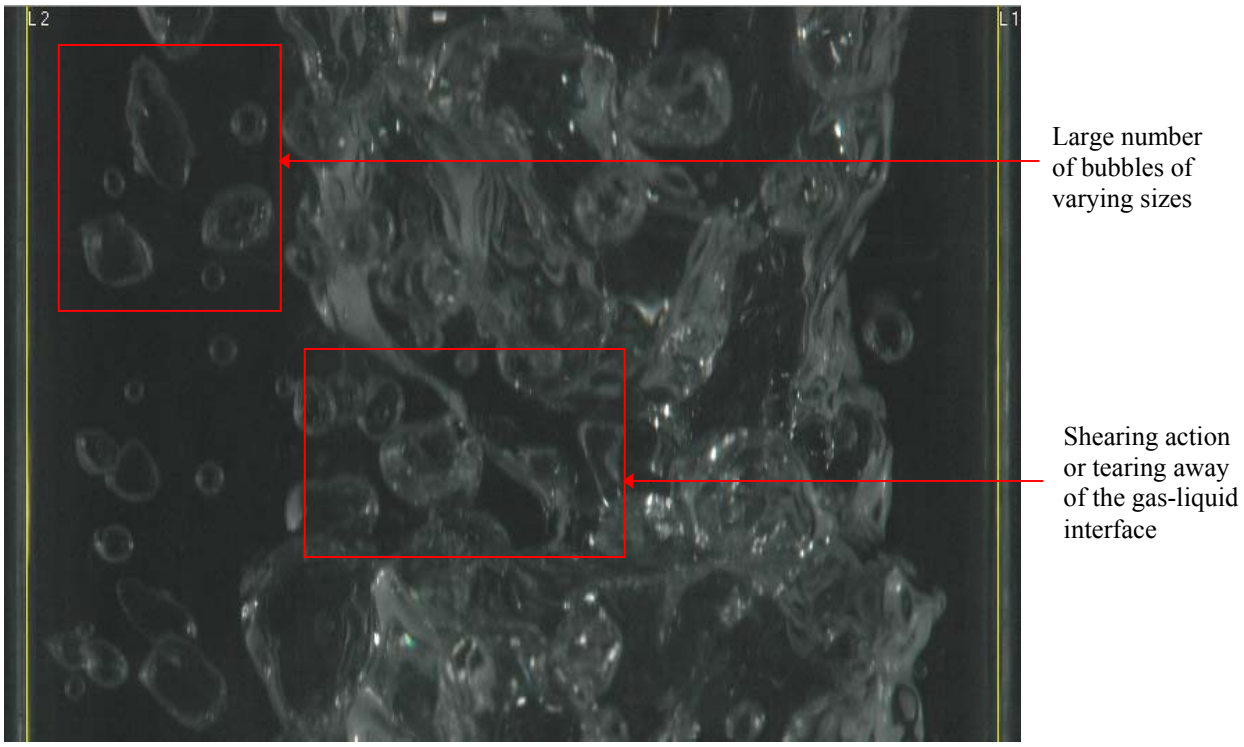

Figure 4.6: Falling annular film at Q = 28.45 L/min and Re = 5924

Reynolds numbers. Large numbers of bubbles with varying sizes were also present in the liquid film. Sometimes the bubbles were large enough that they seemed to occupy a major portion of the liquid film thickness. There is clear evidence that the effects of these bubbles on the walls and on the large waves can no longer be neglected at these Reynolds numbers. The shearing action or the tearing away of the waves can also be clearly seen in figure 4.6. This tearing away of the gas-liquid interface is due to very large disturbance waves that occasionally occurred at Re = 4552 and Re = 5924. From visual observation, the rates of occurrence of this shearing action or tearing away of gas-liquid interface were observed on an average in 10 ~ 20 pictures for each of the 200 pictures analysed at these higher flow rates. Due to this shearing effect and the extremely chaotic nature of the waves, the gas-liquid interface was not clearly discernible. The troughs of the surface waves were sometimes masked by the crests of waves closer to the camera. Also the bubbles occupying a major portion of the liquid film tried to form bridges or isthmuses between tube walls and the gas core. This led to some difficulties in the image

processing and determining the exact liquid film thickness in some of these high Reynolds number pictures.

4.3 Instantaneous film thickness measurements

The Nikon D70 digital SLR camera was located 35 cm from the test section (see Figure 3.10). The camera was operated in the manual focus mode and two remote flash units provided illumination. Measurements of the wall location were carried out before and after taking images at each flow rate (as discussed in the Chapter 3). Both sides of the tube were in the field of view so data could be obtained from both sides. Two hundred high-resolution images were obtained at each of five different flow rates. The images captured were analysed using the image processing techniques discussed in Chapter 3. About 40,000 instantaneous film thickness measurements were extracted at each Reynolds number at longitudinal distances of z = 3.80 m to 3.90 m from the liquid inlet. All the experimental runs were conducted in the facility described in Chapter 3. The present experiments used water at 27ºC and covered a range of liquid Reynolds numbers from 1000 to 6000 in the fully developed turbulent regime. Due to the automated nature of the measurement technique, several hundred instantaneous film thickness measurements may be taken in a few minutes.

In general, the film thickness measurements at the right- and left-hand sides of the tube showed good agreement with each other. A *t*-test was performed to determine whether there is any significant difference between the mean film thicknesses at the right- and left-hand sides. The *t*-test assesses whether the means of two groups are statistically different from each other. The test is applied to the null hypothesis which states that "if the two mean film thicknesses (right-and left-hand sides) being compared belong to the same population, their variance estimates must not be significantly different". The significance of the difference is measured by the ratio of the difference in the means to its standard deviation, and is denoted by t_c, so that

$$t_c = \frac{\left|\overline{\delta}_r - \overline{\delta}_l\right|}{s_d} \qquad (4.1)$$

where $\bar{\delta}_r$ and $\bar{\delta}_l$ are the mean film thicknesses on the right-and left-hand sides, and s_d is the standard deviation of the difference of the two means. The standard deviation of the difference of the two means s_d is obtained from the estimated variance s_c^2. The estimated variance is weighted by the number of degrees of freedom available for its calculation. The estimated variance is calculated as follows:

$$s_c^2 = \frac{s_r^2(n_r - 1) + s_l^2(n_l - 1)}{(n_r - 1) + (n_l - 1)} \qquad (4.2)$$

where

s_c^2 is the estimated variance

n is the number of sample image sets (Here, $n = n_r + n_l$)

subscript r denotes a parameter measured for the right side of the tube

subscript l denotes a parameter measured for the left side of the tube

The standard deviation of the difference of means is:

$$s_d = s_c \sqrt{\frac{n_r + n_l}{n_r n_l}} \qquad (4.3)$$

The level of significance at which the null hypothesis is rejected is usually 5% or 1%. For this thesis, a 1% level of significance was used. If the calculated t_c is greater than the tabulated t_t value (from t-chart) at the specified level of significance, the null hypothesis is rejected, and the conclusion is that the difference is significant. If the calculated t_c is not greater than the tabulated t_t at 1% level of significance, the null hypothesis is accepted and the conclusion is that the difference is insignificant. Table 4.1 shows the t-test results obtained for mean film thicknesses obtained on both sides. As seen from Table 4.1, the calculated t_c values were always found to be less than the tabulated t_t (from t-chart) which was equal to 1.645 for $(n_r + n_l - 2) \approx \infty$ degrees of freedom. Thus, it can be concluded that the differences in the mean film thicknesses between the right- and left-hand sides of the tube are insignificant.

Table 4.1: *t*-test results for raw (uncorrected) mean film thickness data

n	Re	$\overline{\delta}_r$ (mm)	$\overline{\delta}_l$ (mm)	s_r (mm)	s_l (mm)	t_c
200	974	0.748	0.730	0.451	0.475	0.382
200	2111	1.168	1.142	0.640	0.675	0.394
200	3337	1.540	1.511	0.788	0.820	0.369
200	4552	1.920	1.877	0.908	0.913	0.477
200	5924	2.318	2.263	1.024	1.050	0.526

Note: Here *n* represents only the number of sample image sets at each *Re*

Later, the ray tracing model described in Chapter 3 was used to correct for the visual distortion near the tube wall. Thus, the optical distortions were minimised and qualitative film thicknesses measurements were obtained. The details of the experimental results are summarised in Table 4.2. The data for the corrected mean film thickness and standard deviation presented in Table 4.2 for the first three flow rates had an image resolution of 108.7 pixels/mm. The last two flow rates had a

Table 4.2: Summary of experimental results for film thickness

N	Q (L/min)	Re	$\overline{\delta}$ (mm)	s(mm)	$\overline{\delta}^+$
40000	4.679	974	0.891	0.531	19.078
40000	10.139	2111	1.321	0.736	28.287
40000	16.026	3337	1.695	0.892	36.295
40000	21.860	4552	2.068	1.059	44.276
40000	28.453	5924	2.457	1.273	52.599

Note: Here *N* represents the total number of instantaneous film thickness measurements at each Reynolds number.

resolution of 109.9 pixels/mm. The first column represents the total number of instantaneous film thickness measurements *N*. The data in column 4 and column 5 represent the mean film thickness and standard deviation of film thickness fluctuations, respectively. The data in the last column represent the dimensionless mean film thickness obtained by dividing the mean film thickness $\overline{\delta}$ by $\left(\upsilon^2/g\right)^{1/3}$.

In light of the general observations, the instantaneous film thickness δ can be considered to be a randomly fluctuating quantity. The mean film thickness $\overline{\delta}$, standard deviation s, probability density function $P(\delta)$, and the coefficient of variation $s/\overline{\delta}$, were obtained from the data.

4.3.1 Mean film thickness

The mean film thickness $\overline{\delta}$ was determined by averaging the 40,000 instantaneous film thickness measurements for each of the five different flow rates. The dimensionless experimental mean film thickness $\left(\overline{\delta}^{+}\right)$ data were plotted against Reynolds number (*Re*) in figure 4.7. It was found that as the Reynolds number was increased from *Re* = 974 to *Re* = 5924, the mean film thickness increased non-linearly from $\overline{\delta} = 0.891$ mm to $\overline{\delta} = 2.457$ mm. The mean film thickness in the turbulent flow regime is approximately given by the empirical formula in equation 4.4 and shown by dashed line in figure 4.7. Here, the parameters namely kinematic viscosity ν and acceleration due to gravity *g* are constants. With water as the working fluid, the superficial liquid Reynolds number (*Re*) was determined from density ρ (kg/m^3), liquid dynamic viscosity μ (kg/ms), superficial liquid velocity u_l (m/s), and diameter of the vertical tube *D* (m).

$$\overline{\delta} = 0.402\left(\upsilon^2/g\right)^{1/3} Re^{0.558} \qquad (4.4)$$

The measured values were compared with six experimental relationships, i.e., Brotz, 1954 (refer to Fulford, 1964), Brauer, 1956 (refer to Fulford, 1964), Fiend, 1960 (refer to Fulford, 1964), Zhivaikin and Volgin, 1961 (refer to Fulford, 1964),

Takahama and Kato (1980), Karapantsios *et al.* (1989), and also with a theoretical prediction of turbulent film flow (i.e., Dukler and Bergelin 1952). It is worth mentioning here that the actual experimental points for other investigators were not generally available. In their place, figure 4.7 shows points generated from the correlations given in the various papers evaluated at the Reynolds numbers studied in this thesis. It is clear from figure 4.7 that the empirical relationship for the dimensionless mean film thickness obtained in the turbulent film flow regime is in reasonable agreement with the other correlations. The mean film thickness data in the lower turbulent zones (i.e., at Re = 974, Re = 2111 and Re = 3337) lie very close to the experimental results of Karapantsios *et al*. (1989) and Takahama and Kato

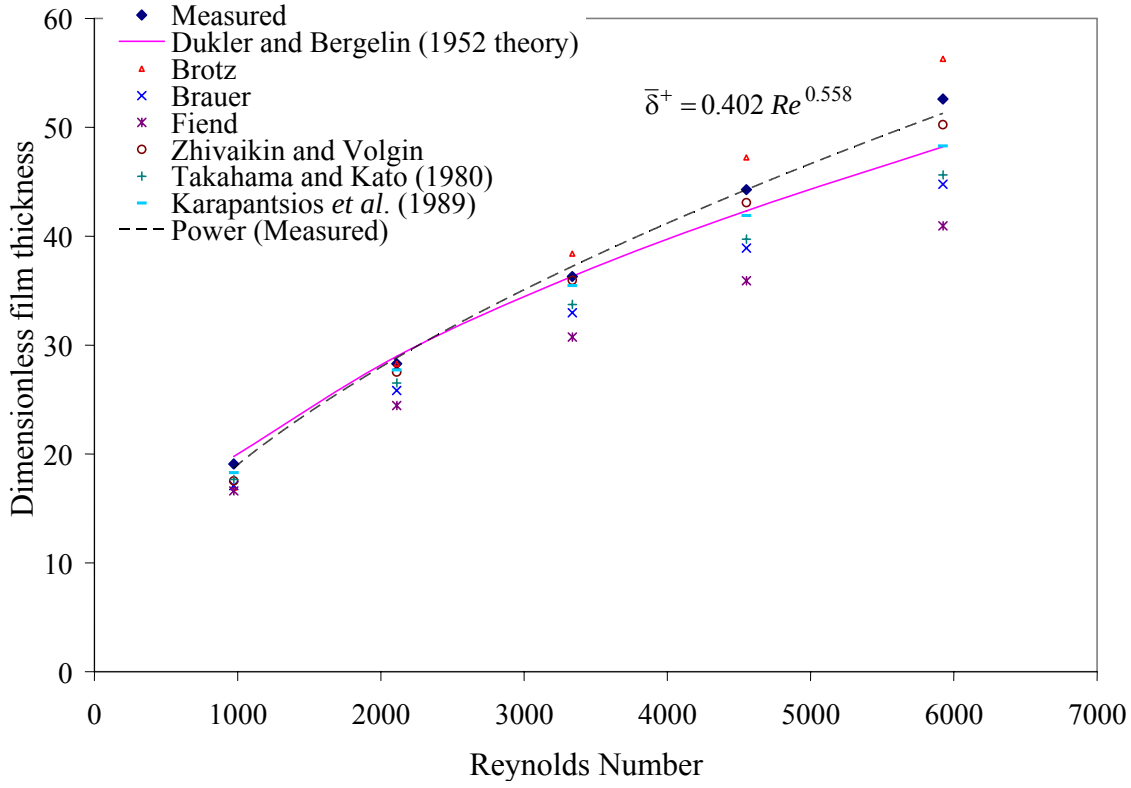

Figure 4.7: Influence of Reynolds number on the dimensionless mean film thickness $\overline{\delta}^{+}$ for the turbulent flow regime

(1980). Dukler and Bergelin (1952) theory also lies close to the experimental data points in the lower turbulent zones. The data sets of Brauer and Fiend are quite low,

especially above *Re* = 2000 where the flow starts to be become more turbulent. At higher Reynolds numbers, there is more scatter in the mean film thicknesses reported in the published data. At *Re* = 4552, the mean film thickness of this work is about 0.08 mm ~ 0.1 mm larger than those of Karapantsios *et al*. (1989) and Dukler and Bergelin (1952), but slightly lower than the data obtained by Zhivaikin and Volgin. At an even higher Reynolds number of *Re* = 5924, the mean film thickness is close to 0.2 mm larger than Karapantsios *et al*. (1989) and Dukler and Bergelin (1952). Karapantsios *et al*. (1989) did not carry out experiments at the higher Reynolds numbers. The deviation of mean film thickness from Dukler and Bergelin (1952) theory could be attributed to the fact that the underlying theory was developed by Nikuradse in 1933 for a full pipe flow. It could be open to discussion as to whether Dukler and Bergelin (1952) theory would still be applicable to the liquid layer in two-phase film flow at these high Reynolds numbers. Telles and Dukler (1970) compared their experimental film thickness measurements (not available here) with the values predicted from Dukler and Bergelin (1952) theory and their analysis showed significant deviations. At high interfacial shear, the agreement was satisfactory, but the discrepancy between Telles's (1970) experiments and Dukler and Bergelin (1952) theory increased at lower gas flow rates. Telles and Dukler (1970) pointed out that the original development of Dukler and Bergelin (1952) does not produce the correct average film thickness for a film with large interfacial waves.

4.3.2 Standard deviation

Waves are observed on falling annular films (see figure 4.8) even when the gas flow rate is zero. A visual observation suggests that the waviness of the film flow increases with increasing Reynolds number in the turbulent flow regime. Post processing of the digital images showed random fluctuations in the instantaneous film thickness δ. Further analysis was carried out to determine the standard deviation s.

The data obtained support this observation, showing an increase in the standard deviation *s* as the Reynolds number, *Re* is increased. As the Reynolds number was

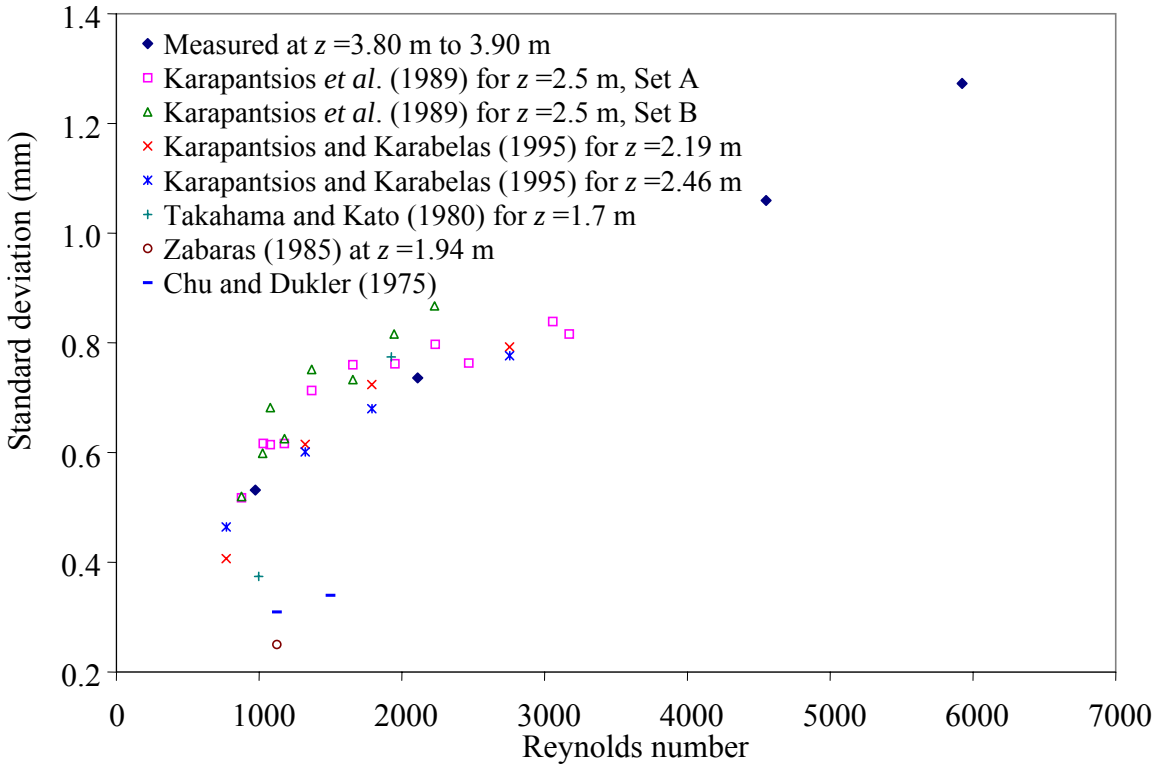

Figure 4.8: The influence of Reynolds number on the standard deviation *s* of film thickness fluctuations

increased from *Re*= 974 to 3337, the standard deviation *s* increased from 0.531 mm to 0.892 mm. The data obtained here clearly show that at a distance *z* = 3.80 m to 3.90 m from the liquid entry, the standard deviation values are very large which implies that at a large distance from the liquid inlet, the waves have higher amplitudes. The results obtained were compared with two sets of experimental data (Set A, Set B) obtained by Karapantsios *et al*. (1989) at a longitudinal distance of *z* = 2.5 m as shown in figure 4.8. It is worth mentioning that Karapantsios *et al.* (1989) also observed a similar trend in his experiments showing an increase in standard deviation as the Reynolds number is increased and at a large distance from the liquid entry. The data compared reasonably well, although Karapantsios *et al*. (1989) reported slightly higher standard deviation values in the lower turbulent zones. The standard deviation results obtained in this thesis were also compared with two other experimental sets of data obtained by Karapantsios and Karabelas (1995) for *z* = 2.19 m and *z* = 2.46 m in the lower turbulent zones. In general, the data agreed well with

the standard deviation values of both Karapantsios and Karabelas (1995) and Karapantsios *et al*. (1989). Takahama and Kato's (1980) data on standard deviation *s* also displayed an increasing trend up to *Re* = 2000. Relatively large standard deviation values, such as those obtained in this thesis, were also reported by Takahama and Kato (1980) for *z* = 1.7 m. From the standard deviation values obtained here and their comparison with other established experimental results, the liquid film can be considered to be fully developed at a longitudinal distance of *z* = 3.80 m to 3.90 m from liquid inlet. However, the standard deviation values presented by Zabaras (1985) were small, e.g., *s* ~ 0.25 mm at 1.94 m from the inlet and *Re* = 1125. He reported that, above *Re* = 1250, there is little increase in the standard deviation. The reasons for such a large deviation might be due to the fact that Zabaras (1985) employed a different technique for measuring the film thickness and also used different test fluids in most of the runs. Chu and Dukler (1975) also reported standard deviation values for falling liquid films with and without gas flow. For the case of zero gas flow, the standard deviation values were *s* ~ 0.3093 mm at *Re* = 1125 and *s* ~ 0.3398 mm at *Re* = 1500. Again the values reported by Chu and Dukler (1975) were small compared to the present study. The reasons could be because Chu and Dukler's (1975) experiments were limited only to transition and lower turbulent regimes up to a Reynolds number of $Re \leq 1500$.

New values of standard deviation have been reported here at Reynolds numbers of *Re* = 4552 and *Re* = 5924 in the higher turbulent zones. There is no indication that the standard deviation values have reached an upper limit or an asymptotic value. The waviness of the falling annular films continues to increase with increasing mean film thickness $\overline{\delta}$ and increasing Reynolds numbers. The standard deviation *s* reaches a value of *s* ~ 1.273 mm at Reynolds number *Re* = 5924 and mean film thickness $\overline{\delta} = 2.457$ mm. The falling films become very thick and the gas-liquid interface tends to be extremely wavy at these very high Reynolds numbers. Thus, it can be concluded that thin films are characterised by small waves that are less wavy and the thicker films are characterised by large disturbance waves that are wavier in nature.

4.3.3 Coefficient of variation

To evaluate the relative degree of variation in the instantaneous film thickness data, the ratio of the standard deviation s to the mean film thickness $\overline{\delta}$, also known as the coefficient of variation, was plotted as a function of Reynolds number. Figure 4.9 shows the influence of Reynolds number on the coefficient of variation. As the Reynolds number is increased from 974 to 5924, the coefficient of variation decreases moderately from 0.5963 to 0.5180. These values are in general agreement with the data presented by Karapantsios *et al*. (1989), although the coefficient of variation in Karapantsios *et al*. (1989) data reduced more rapidly with increasing Reynolds number. Karapantsios *et al.* (1989) observed a maximum value of the coefficient of variation, $s/\overline{\delta}$ between $Re \approx 1000$ and $Re \approx 1250$. Furthermore, Karapantsios *et al*. (1989) also observed a substantial reduction in the ratio of $s/\overline{\delta}$ for $Re \geq 1250$ and suggested that at this Reynolds number, a possible upper limit had been reached for the growth or amplification of waves. Although it is apparent that the data obtained

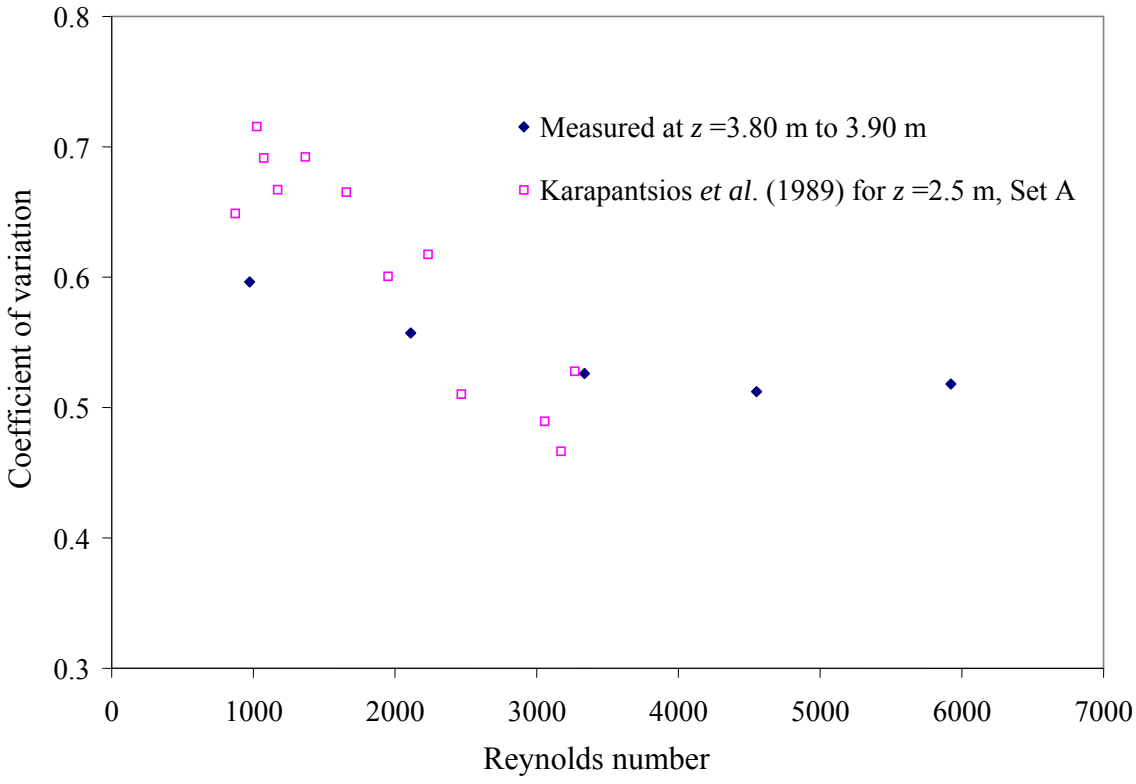

Figure 4.9: The influence of Reynolds number on the coefficient of variation, $s/\overline{\delta}$

in the present study do not make it possible to fix the exact Reynolds number at which the maximum upper limit for amplification of waves has been reached, a similar decreasing trend to those obtained by Karapantsios *et al*. (1989) had been observed in the data at $Re \geq 1000$. Karapantsios and Karabelas (1995), Karapantsios *et al*. (1989) and Takahama and Kato (1980), all observed a limiting value of the coefficient of variation, $s/\overline{\delta} \approx 0.3$ to 0.7 in their experimental range. The values obtained here are in general agreement with those results.

4.3.4 Probability density function

The probability density function was introduced to illustrate the detailed statistical distribution of the instantaneous film thickness. The mean film thickness and standard deviation discussed earlier are properties of the probability density function. The probability density functions for the five different Reynolds numbers are shown in Figure 4.10.

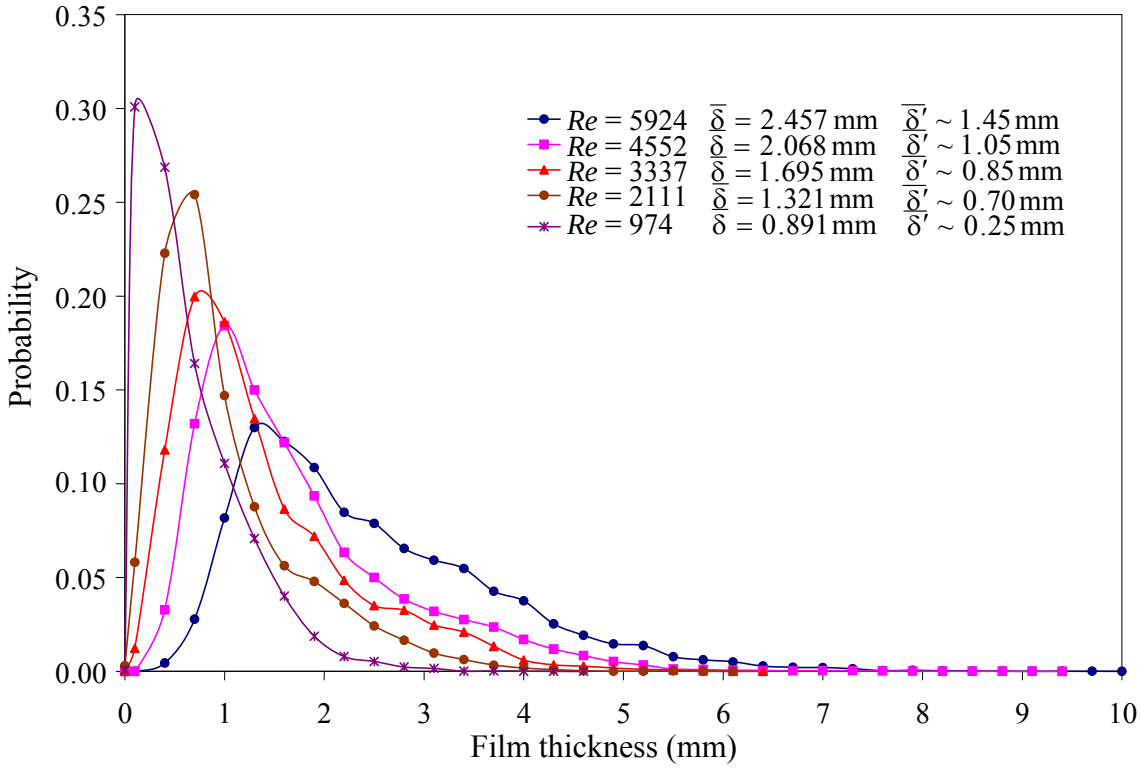

Figure 4.10: The influence of Reynolds number on the probability density function, P

Points on this figure were produced by binning the film thickness measurements into intervals of $\Delta\delta = 0.3$ mm for each of the Reynolds numbers. The probability density function of the film thickness describes the likelihood of the film assuming a value within a given interval. As has already been observed by other investigators, the probability density function is highly asymmetrical and the height of the peak decreases with increasing liquid Reynolds number. The maximum peak or the main peak can be considered to represent the modal value of film thickness or the substrate film thickness. It is very interesting to note that the deviation between the mean film thickness $\overline{\delta}$ and the substrate film thickness $\overline{\delta'}$ increases as the Reynolds number is increased, but the substrate film thickness $\overline{\delta'}$ is always below the mean film thickness $\overline{\delta}$. This suggests that the liquid film may assume a defined film thickness and the waves ride on top of the substrate. All the probability distributions obtained here have a maximum peak and are skewed to the right hand side with a long tail that stretches to over 6 times the peak or modal value of film thickness. The increase in skewness and the decrease in the height of the peak with liquid Reynolds number can be attributed to presence of large disturbance waves which ride on the substrate film. This enhances the waviness of the film. As the waviness is increased, the probability that the film thickness will fall within a particular interval is decreased and the skewness is increased. Thus, it is very clear that the probability density distributions that describe the statistical characteristics of film thickness are non-Gaussian in nature. It is worth mentioning here that similar observations were also made by Telles and Dukler (1970), Chu and Dukler (1975), Zabaras (1985) and Karapantsios *et al.* (1989).

4.3.5 Sensitivity analysis

To determine whether 200 images are sufficient to get accurate measurements of mean film thickness and standard deviation, a sensitivity analysis was performed. Sensitivity plots check for the convergence of statistical parameters such as the film thickness and standard deviation. Figures 4.11 to 4.15 show the sensitivity plots obtained at different Reynolds numbers. At first, the 40,000 instantaneous film thickness measurements were grouped into eight independant sets of 5000

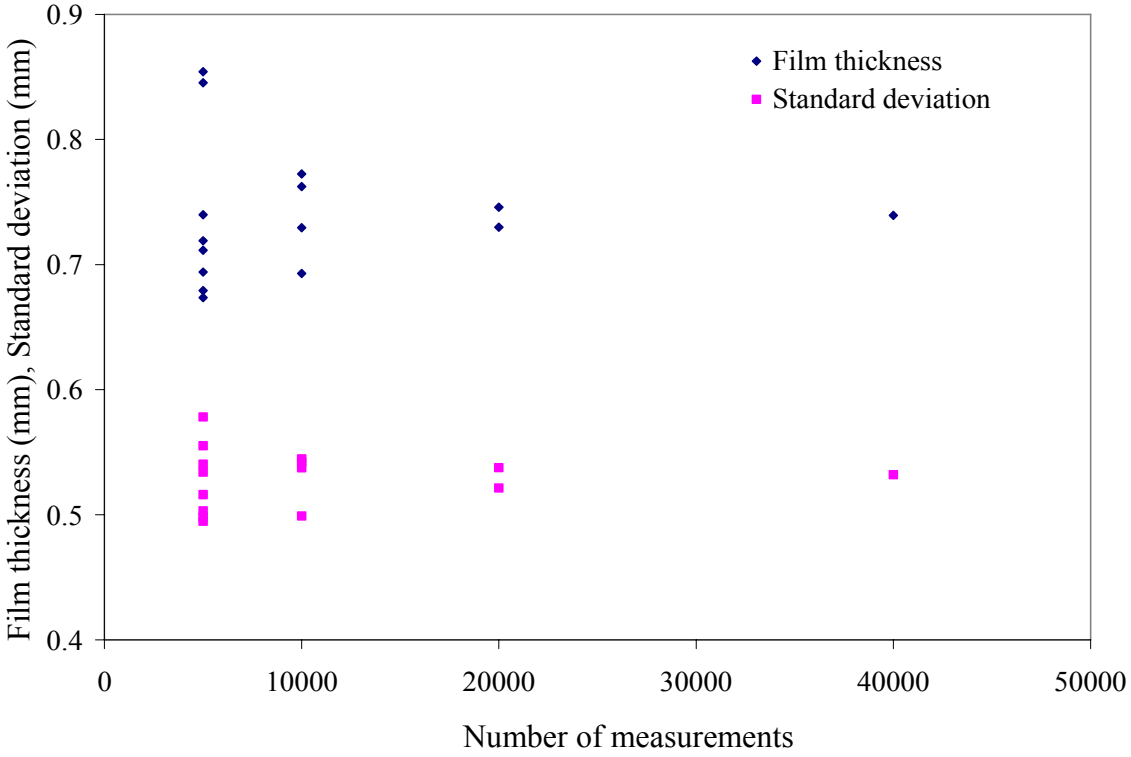

Figure 4.11: Sensitivity plot for *Re* = 974

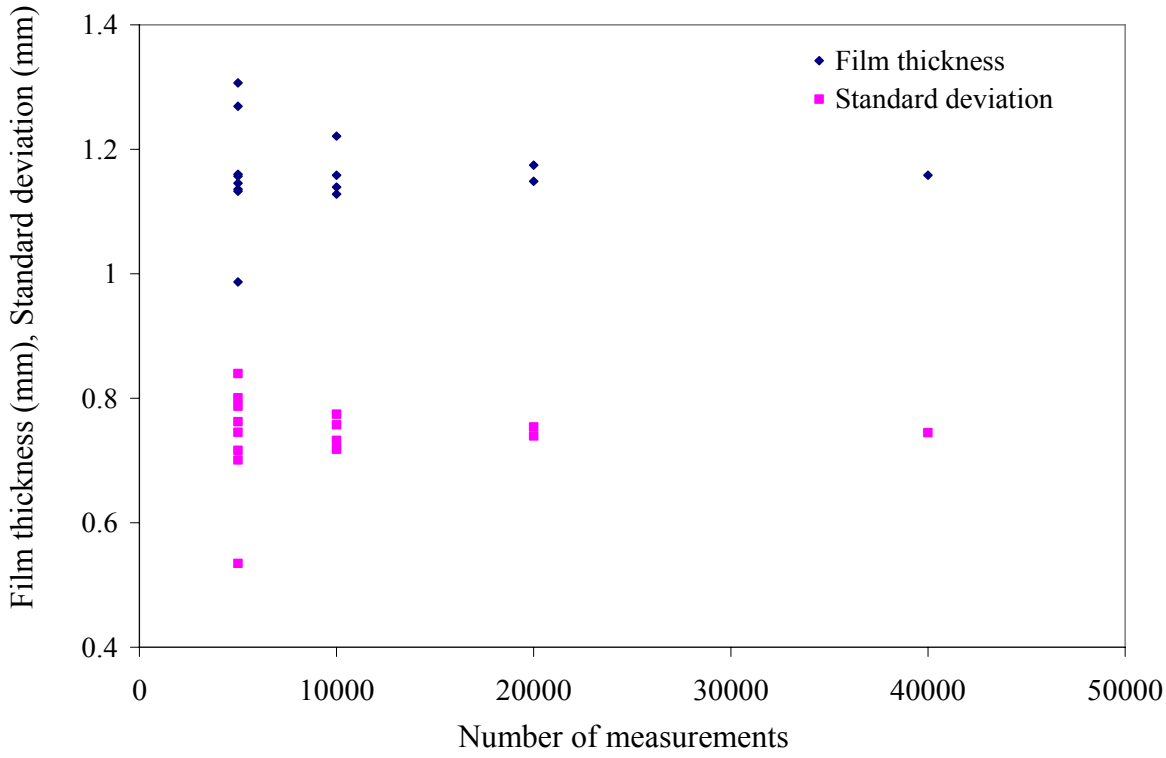

Figure 4.12: Sensitivity plot for *Re* = 2111

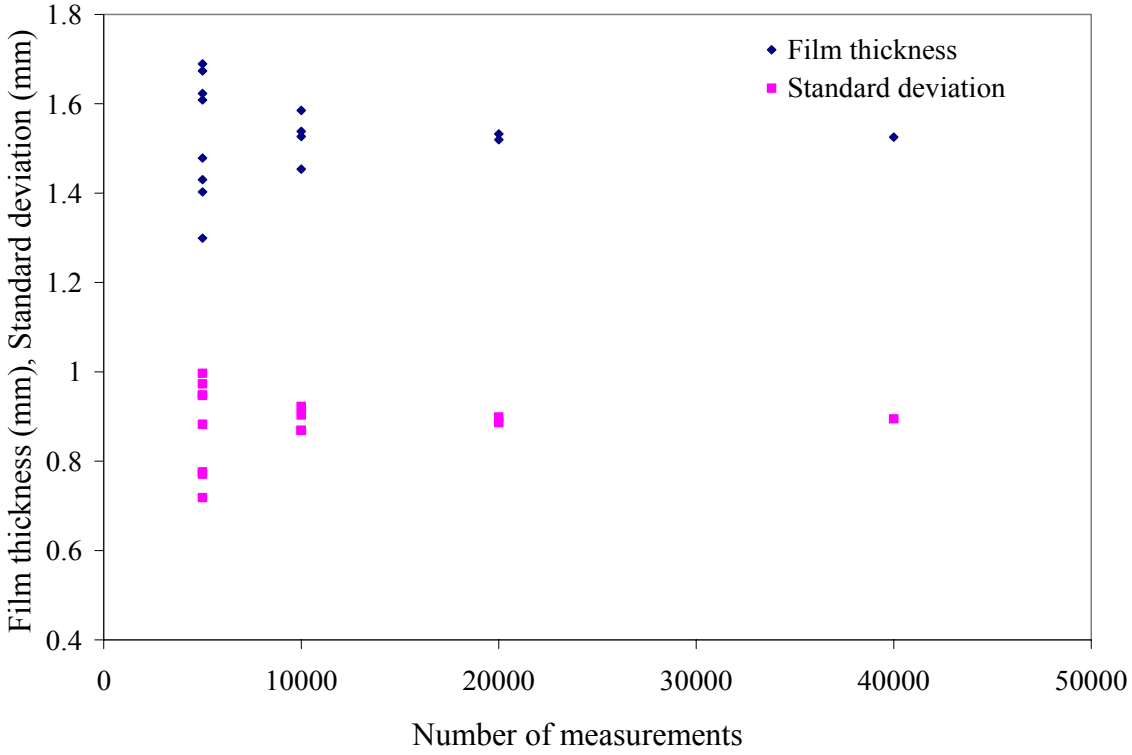

Figure 4.13: Sensitivity plot for *Re* = 3337

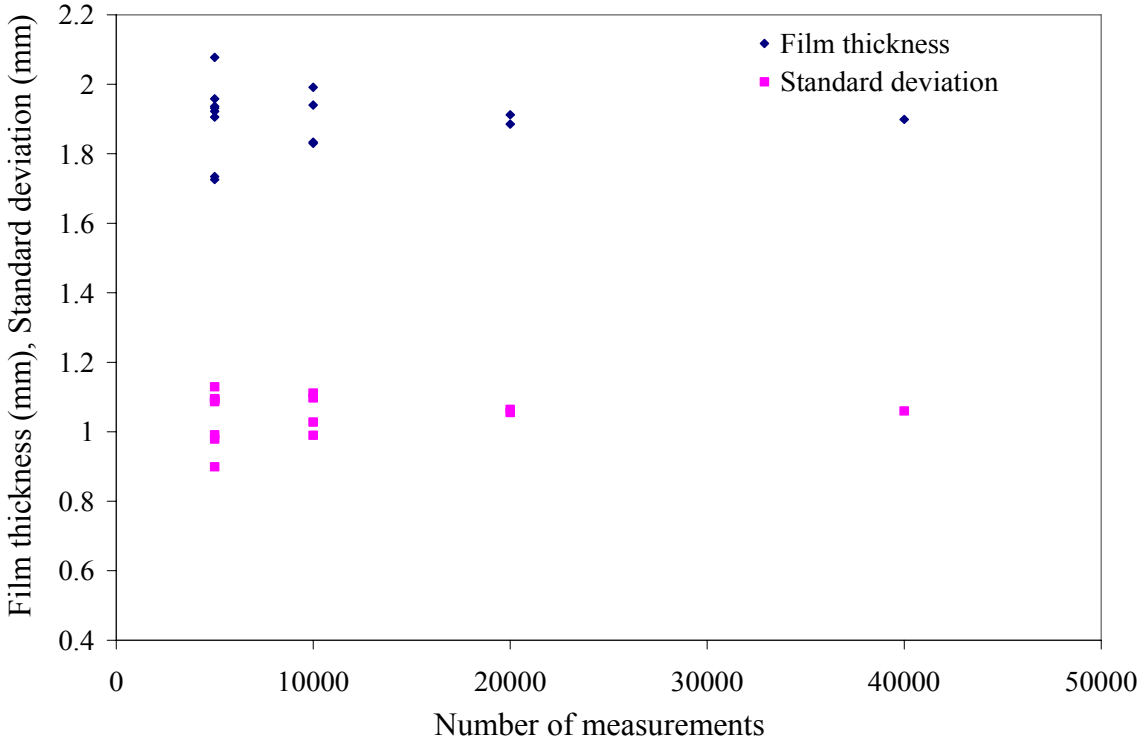

Figure 4.14: Sensitivity plot for *Re* = 4552

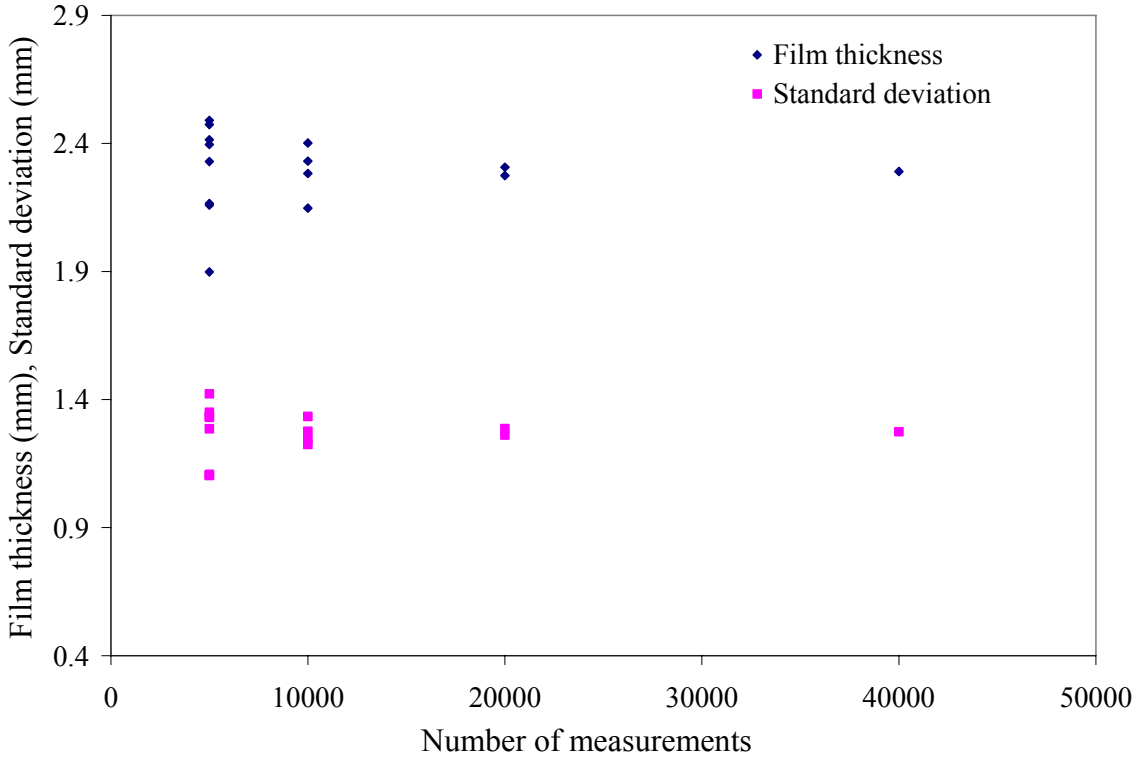

Figure 4.15: Sensitivity plot for Re = 5924

measurements each and then the mean film thickness and the standard deviations of the eight sets were calculated. In a similar way, the measurements were grouped into four sets of 10,000, two sets of 20,000 and one set of 40,000 and the same steps were repeated. The film thickness $\overline{\delta}$ and standard deviation s were plotted against number of measurements in a set N. It was found that when the measurements were grouped into eight sets of 5000 measurements each, the scatter observed in the data was large for all Reynolds numbers. The scatter in the data was reduced when 10,000 measurements were grouped together and the data converged even further for 20,000 measurements. Finally, all the 40,000 instantaneous measurements were taken together at once. The sensitivity plots show that 40,000 instantaneous film thickness measurements are adequate to provide a good estimation of the film thickness and standard deviation measurements made at these Reynolds numbers.

4.4 Summary

An experimental study of falling annular films was conducted at five different Reynolds numbers in the turbulent regime. Film thickness measurements were obtained at a longitudinal distance of z = 3.80 m to 3.90 m from the liquid inlet. One of the main objectives of the study was to characterise the film thickness at high Reynolds numbers. The experiments involved the use of flow visualisation techniques that yield information regarding the turbulent characteristics in falling liquid films. 40,000 instantaneous film thickness measurements of falling annular films at Reynolds numbers in the range Re = 1000 ~ 6000 were extracted using a non-intrusive imaging technique. A ray tracing model was employed to reduce optical distortion effects in cylindrical tubes. This technique increased the accuracy of the imaging technique and enabled quantitative measurements of film thickness to be made. From visual observation of the images obtained, no definite wave patterns could be established at these Reynolds numbers. However, the turbulent waves appeared to be similar in appearance to very large breaking ocean waves driven by strong winds. The random nature of these falling annular films was subjected to statistical analysis and qualitative observations were made at these Reynolds numbers.

The experiments conducted here enabled the determination of the some statistical characteristics of falling annular films. A correlation for dimensionless mean film thickness $\overline{\delta}^+$, obtained in the turbulent flow regime was found to be in reasonable agreement with the other established experimental and theoretical studies. It was shown that the Reynolds number influences the statistical characteristics of film thickness such as standard deviation s and coefficient of variation $s/\overline{\delta}$. Results obtained at higher Reynolds numbers show that the standard deviation continues to increase in proportion to the mean film thickness in the turbulent regime. In other words, in the lower turbulent zones the films are thin and less wavy, whereas in the higher turbulent zones the films are thicker and extremely wavy. In addition, the

measured probability density distributions $P(\delta)$ were also studied. The probability distributions obtained were asymmetric. All the measured probability distributions had a maximum peak and were skewed to the right hand side with a long tail that stretches to over six times the peak value. The maximum peak represents the modal value of the film thickness or the substrate film thickness. The increase in skewness and the decrease in the height of the peak with liquid Reynolds number could be attributed to presence of large disturbance waves which ride on the substrate film that tends to enhance the waviness of the film.

CHAPTER 5
CONCLUSIONS AND RECOMMENDATIONS

5.1 Conclusions

A non-intrusive imaging technique was used to extract 40,000 instantaneous film thickness measurements of falling annular films at each of five different Reynolds numbers in the range *Re* = 1000 ~ 6000 for the fully developed turbulent regime. The conclusions drawn from this study are outlined below.

1. Digital images of the falling annular films obtained with a spatial resolution of 3008×2000 pixels have been presented here. In general, the waves are not axisymmetric, i.e., there is a lot of azimuthal variation in the film thickness. The turbulent waves appeared to be similar in appearance to very large breaking ocean waves driven by strong winds.
2. A correlation for dimensionless mean film thickness $\overline{\delta}^+$ was obtained in the turbulent flow regime. The dimensionless mean film thickness $\overline{\delta}^+$ obtained here was found to be in reasonable agreement with the other established experimental and theoretical studies. It was shown that the Reynolds number influences the statistical characteristics of film thickness such as standard deviation s and coefficient of variation $s/\overline{\delta}$. Results obtained at higher Reynolds numbers show that the standard deviation continues to increase in proportion to the mean film thickness in the turbulent regime. In other words, in the lower turbulent zones the films are thin and less wavy, whereas in the higher turbulent zones the films are thicker and extremely wavy in nature.

3. The probability density distributions $P(\delta)$ were also obtained. It was found that the measured probability density distributions were asymmetric. They all had a maximum peak and were skewed to the right hand side with a long tail that stretches to over six times the peak value. The maximum peak could be considered to represent the modal value of the film thickness or the substrate film thickness. The increase in skewness and the decrease in the height of the peak with liquid Reynolds number could be attributed to the presence of large disturbance waves which ride on the substrate film that tends to enhance the waviness of the film.
4. In addition, an advanced ray tracing model was employed to reduce the optical distortions caused by the tube wall curvature. Experimental studies and calibration procedures were also conducted in the laboratory to confirm the validity of the ray tracing model. The ray tracing model and the calibration procedures employed here increased the accuracy of this imaging technique.

5.2 Recommendations for future work

A more detailed study of the statistical characteristics of waves is required. The measurement of probability distributions makes it possible to make accurate determination of the moments. The second and the third moments will reveal more information regarding the structure of these large waves and their contribution to the gas-liquid interface. Moreover the frequency of large waves occurring at these high flow rates can also be measured from their spectral density functions. It is a measure of how much of the motion is assignable to wavelengths around a certain value. This can be achieved by using an accurately timed camera shutter with higher framing rates. By using a combination of different parameters such as the frequency of the surface waves, the influence of other dimensionless numbers such as the Strouhal number can also considered. The Strouhal number is formed from the frequency of the surface waves, and various geometrical ratios.

Further experimental work is also required to determine the hydrodynamic characteristics of falling annular films such as instantaneous velocity fields and wall shear stress. This is very challenging since the thickness of falling annular films are usually of the order of one millimetre. To enable these quantitative measurements, a refractive index matching fluid should be used in the optical correction box and in the test section. Particle image velocimetry (PIV) can be used to accurately measure the complex instantaneous velocity field in falling annular films. It involves the use of whole field techniques based on imaging the light scattered by small particles in the flow illuminated by a laser. The two-dimensional or three-dimensional time dependant velocity fields might yield more information regarding the structure of large waves in the turbulent region. Studies can also be undertaken to investigate the mechanisms governing wave growth and wave-to-wave interactions at the gas-liquid interface. It may be of interest to examine the velocity profiles to generate streamlines to describe the flow field completely in falling annular films in the turbulent regime. The local wall shear stress can also be estimated by measuring the velocity gradient near the wall.

References

Agrawal, Y., Talbot, L., Gong, K., 1978. Laser anemometer study of flow development in curved circular pipes. Journal of Fluid Mechanics. **85**, 497-518.

Alekseenko, S.V., Nakoryakov, V.E., and Pokusaev, B.G., 1985. Wave formation on vertical falling liquid films. International Journal of Multiphase Flow. **11**, 607-627.

Alekseenko, S.V., Nakoryakov, V.E., Pokusaev, B.G., 1994. In: Fukano, T. (Ed.), Wave flow of liquid films. Begell House, New York.

Ambrosini, W., Forgione, N., Oriolo, F., 2002. Statistical characteristics of a water film falling down a flat plate at different inclinations and temperatures. International Journal of Multiphase Flow. **28**, 1521-1540.

Astola, J., Haavisto, P., and Neuvo, Y., 1990. Vector median filters. Proceedings of the Institute of Electrical and Electronic Engineers. **78**, 678-689

Bach, P., and Villadsen, J., 1984. Simulation of the vertical flow of a thin, wavy film using a finite element method. International Journal of Heat and Mass Transfer. **27**, 815-827.

Bankoff, S.G., 1971. Stability of liquid flow down a heated inclined plate. International Journal of Heat Transfer. **14**, 377-385.

Bathia, J.C., Durst, F., Jovanovic, J. 1982. Correction of hot-wire measurements. Journal of Fluid Mechanics. **122**, 411-431.

Belkin, H.H., McLeod, A.A., Monrad, C.C., and Rothfus, R.R., 1959. Turbulent liquid flow down vertical walls. American Institute of Chemical Engineers Journal. **5**, 245-248.

Bendat, J.S., and Piersol, A.G., 1971. Random Data: Analysis and Measurement Procedures. Wiley, New York.

Bicen, A.F. 1982: Refraction correction for LDA measurements in flows with curved optical boundaries. TSI Quarterly. **8**, 10-12.

Bird, R.B., Stewart, W.E., and Lightfoot, E.N. 1960. Transport Phenomena. Wiley, New York. 3-179.

Blass, E., 1979. Gas/film flow in tubes. International Chemical Engineering. **19**, 183-195.

Boadway, J.D.; Karahan, E. 1981. Correction of laser Doppler anemometer readings for refraction at cylindrical interfaces. DISA Information. **26**, 4-6.

Bovendeerd, P.H.M.; Van Steenhoven, A.A.; Van de Vosse, F.N.; Vossers, G. 1987. Steady entry flow in a curved pipe. Journal of Fluid Mechanics. **177**, 233-246.

Brauner, N., 1987. Roll wave celerity and average film thickness in turbulent wavy film, flow. Chemical Engineering Science. **42**, 265-273.

Brown, R. A. S., 1965. The mechanics of large gas bubbles in tubes. Canadian Journal of Chemical Engineering. **43**, 217-223.

Budwig, R. 1994. Refractive index matching methods for liquid flow investigations. Experiments in Fluids. **17**, 350-355.

Chang, H.C., 1994. Wave evolution on a falling film. Annual Review of Fluid Mechanics. **26**, 103-136.

Chen, R.C.; Fan, L.S. 1992. Particle image velocimetry for characterizing the flow structure in three-dimensional gas-liquid-solid fluidized beds. Chemical Engineering Science. **47**, 3615-3622.

Chu, K.J., and Dukler, A.E., 1974. Statistical characteristics of thin, wavy films: part II. Studies of the substrate and its wave structure. American Institute of Chemical Engineers Journal. **20**, 695-705.

Chu, K.J., and Dukler, A.E., 1975. Statistical characteristics of thin, wavy films: part III. Structure of the large waves and their resistance to gas flow. American Institute of Chemical Engineers Journal. **21**, 583-593.

Dukler, A.E., Bergelin, O.P., 1952. Characteristics of flow in falling films. Chemical Engineering Progress. **48**, 557-563.

Duncan, D.D.; Bargeron, G.B.; Borchardt, S.E.; Deters, O.J.; Gearhart, S.A.; Mark F.F. 1990. The effect of compliance on wall shear in casts of a human aortic bifurcation. ASME Journal of Biomechanical Engineering. **112**, 183-188.

Durret, R.P.; Gould, R.D.; Stevenson, W.H.; Thompson, H.D. 1985. A correction lens for laser Doppler velocimeter measurements in a cylindrical tube. American Institute of Aeronautics and Astronautics Journal. **23**, 1387-1391.

Durst, F.; Muller, R; Jovanovic, J. 1988. Determination of the measuring positioning laser-Doppler anemometry. Experiments in Fluids. **6**, 105-110.

Fulford, G.D., 1964. The flow of liquids in thin films. In: Advances in Chemical Engineering, edited by Drew, T.B., Hoopes, J.W., and Vermeulen, T., **5**, Academic Press, 151-235.

Gupta, A.K. and Kaplan, R.E. 1972. Statistical characteristics of Reynolds stress in turbulent boundary layer. Physics of Fluids. **15**, 981-985.

Hewitt, G.F., and Hall-Taylor, N.S., 1970. Annular two-phase flow. Pergamon Press, Oxford.

Jackson, M.L. 1955. Liquid films in viscous flow. American Institute of Chemical Engineers Journal. **1**, 231-240.

Kang, H.C., Kim M.H., 1992. The development of a flush-wire probe and calibration method for measuring liquid film thickness. International Journal of Multiphase Flow. **18**, 423-437.

Kapitza, P.L., 1947. Wave flow of thin layers of a viscous fluid, English translation in collected papers of P.L. Kapitza, II, Macmillan, New York.

Kapitza, P.L., 1965. In: Ter-Haar, D. (Ed), Collected papers of Kapitza 1938-1964,. Pergamon Press, New York. **2,** 662-709.

Karapantsios, T.D., Paras, S.V., and Karabelas, A.J., 1989. Statistical characteristics of free falling films at high Reynolds numbers. International Journal of Multiphase Flow. **15**, 1-21.

Karapantsios, T.D., and Karabelas, A.J, 1995. Longitudinal characteristics of wavy falling films. International Journal of Multiphase flow. **21**, 119-127.

Karimi, G., and Kawaji, M., 1998. An experimental study of freely falling films in vertical tube. Chemical Engineering Science. **53**, 3501-3512.

Kheshgi, H.S., and Scriven, L.E., 1987. Distributed film flow on a vertical plate. Physics of Fluids. **30**, 990-997.

Kokamustafaougullari, G., 1985. Two- fluid modelling in analyzing the interfacial stability of liquid film flows. International Journal of Multiphase flow. **15**, 1-21.

Koskie, J.E., Mudawar, I., and Tiederman, W.G., 1989. Parallel – wire probes for measurement of thick liquid films. International Journal of Multiphase flow. **15**, 521-530.

Liu, C.H.; Vafidis, C.; Whitelaw, J.H. 1990. Flow in the coolant passages of an internal combustion engine cylinder head. Experiments in Fluids. **10**, 50-54.

Lowe M.L.; Kutt, P.H. 1992. Refraction through cylindrical tubes. Experiments in Fluids. **13**, 315-320.

Neal, L.G., and Bankoff, S.G., 1963. A high resolution resistivity probe for determination of local void properties in gas-liquid flow. American Institute of Chemical Engineers Journal. **9**, 490.

Nguyen, L.T., Balakotaiah, V., 2000. Modelling and experimental studies of wave evolution on free falling liquid films. Physics of Fluids. **12**, 2236-2256.

Pearson, D.E., 1991 Image Processing, McGraw-Hill, New York.

Perry, R.H.; Green, D.W. 1973. Perry's Chemical Engineering Handbook (ISBN 0-0704-9578-9). 6th edition, New York, McGraw-Hill.

Portalski, S., 1963. Studies of falling liquid film flow: film thickness on a smooth vertical plate. Chemical Engineering Science. **18**, 787-804.

Russ, J.C., 1995 The image processing Handbook, CRC Press.

Salamon, T.R., Armstrong, R.C., Brown, R.A., 1994. Travelling waves on inclined films: numerical analysis by the finite-element method. Physics of Fluids. **6**, 2202-2220.

Salazar, R.P. and Marschall, E., 1978. Time average local thickness measurement in falling liquid film flow. International Journal of Multiphase flow. **4**, 408-412.

Spindler, B., 1981. Linear stability of liquid films with interfacial phase change. International Journal of Heat and Mass Transfer. **25**, 161-173.

Stuhltrager, E., Miyara, A., Uehara, H.., 1995. Flow dynamics and heat transfer of a condensate film on a vertical wall-part II. Flow dynamics and heat transfer. International Journal of Heat and Mass Transfer. **38**, 2715-2722.

Takahama, H. and Kato, S., 1980. Longitudinal flow characteristics of vertically falling liquid films without concurrent gas flow. International Journal of Multiphase Flow. **6**, 203-215.

Taylor, N.H., Hewitt, G.F., and Lacey, P.M.C., 1963. The motion and frequency of large disturbance waves in annular two-phase flow of air-water mixtures. Chemical Engineering Science. **18**, 537-552

Telles, A.S., Dukler, A.E., 1970. Statistical characteristics of thin, vertical, wavy, liquid films. Industrial and Engineering Chemistry Fundamentals. **9**, 412-421.

Wasden, F.K. and Dukler, A.E., 1989. Insights into hydrodynamics of free falling liquid films. American Institute of Chemical Engineers Journal. **35**, 187-195.

Webb, D.R., and Hewitt, G. 1975. Downwards co-current annular flow. International Journal of Multiphase Flow. **2**, 35-49.

Yih, C.S., 1963. Stability of liquid flow down an inclined plane. Physics of Fluids **6**, 321-334.

Yu, L.Q., Wasden, F.K., Dukler, A.E., Balakotaiah, V., 1995. Nonlinear evolution of waves on falling films at high Reynolds number. Physics of Fluids. **7**, 1886-1902.

Zabaras, G.J., 1985. Studies of vertical annular gas-liquid flows. Ph.D Thesis in Chemical Engineering, University of Houston, Texas, U.S.A.

Appendix A: Script for the measurement of instantaneous film thickness

This macro performs the image processing operations using Inspector® and extracts the instantaneous film thickness measurements and stores them in a text file.

```
/Description: Measurement of instantaneous film thickness
Def ScrRec2()
{
        // Attach the dll file that is required to write results to a text file.
        UtilLoadLib("c:\insptr\UtilSI32.ldf", "userdll");

        // Set up the base name for the images.
        base_name="C:\Documents and Settings\anp483\Desktop\";

                file_name=base_name;
                result_file_name=base_name;

                file_name=file_name+"DSC_"+file_number+".JPG";
                result_file_name=result_file_name+"DSC_"+file_number+".txt";

// Open a text file to recieve the results.
  userdll.SetLogFileName(result_file_name);

I_DSC_0691=ImgLoad(file_name);

//Create a grayscale image from a colour image.
ImgSetCurrent(I_DSC_0691, R_Def, ALL_BANDS);
I_IMAGE1=ImgNewDisp(3008, 2000, 1, IMG_MONO, IMG_8U, PAL_SOURCE,
0, IMG_AUTOSCALE, 8);

//Convert the gray scale image to a binarized image
ImgConvert();
ImgSetCurrent(I_IMAGE1, R_Def, ALL_BANDS);
I_IMAGE2=ImgNewDisp(3008, 2000, 1, IMG_MONO, IMG_8U, PAL_SOURCE,
0, IMG_AUTOSCALE, 8);

//Perform Uniform histogram equalization mapping
MapHistogramEqualize(MAP_UNIFORM, 0, 128, 255);

//Set the threshold for the binarized image
MapClipGeneral(25, NOT_USED, 0, 255, NOT_USED, LEVEL_BUFFER);
ImgSetCurrent(I_IMAGE2, R_Def, ALL_BANDS);

// Applying a Rank filter
FiltMedian();
```

```
//To perform open and a close operation
MorphCloseEx(2, 1);
MorphOpenEx(15, 1);

//To perform erosion and dilation operation/ Morphological operation
MorphErodeEx(1, 1);
MorphDilateEx(1, 1);

//Initialize the constants
right_wall_position=2875;
left_wall_position=105;
search_box_height=2000;

x1_position=right_wall_position-30;

ImgSetCurrent(I_DSC_0691, R_Def, ALL_BANDS);
MeasNewRefLine(right_wall_position, 0, right_wall_position, 2000);
ImgSetCurrent(I_IMAGE2, R_Def, ALL_BANDS);


//To loop through every 20 j positions on the righthand side of the binarized image

for(j=1;j<=2000;j=j+20)
{
      // to find an edge on the right right hand side and allocate a point and/or line
marker based on this edge (note:set width of search box to 1 pixel)

 MeasSetEdgeStripeAngle(MEAS_NEAREST_NEIGHBOR, 360, 360, 5, 5);
 MeasNewEdgeEx(270, MEAS_POL_AUTO, right_wall_position-70, j,
1,search_box_height, right_wall_position-50,j+0.5, MEAS_MARKER_POS,
MEAS_ANY, MEAS_ANY);

        x1_position=MeasGetResult(MeasGetLastID(),MEAS_X1);

        userdll.LogInteger(j,0);                // Write the j position to a file.
        userdll.LogString("  ",0);              // Write a space between j and x1 positions
        userdll.LogFloat(x1_position,1);        // Write the x1 position to a file.

ImgSetCurrent(I_DSC_0691, R_Def, ALL_BANDS);
MeasNewRefPoint(x1_position,j);
ImgSetCurrent(I_IMAGE2, R_Def, ALL_BANDS);

}

//To loop through every 20 j positions on the left hand side of the binarized image
```

```
x2_position=left_wall_position+30;

ImgSetCurrent(I_DSC_0691, R_Def, ALL_BANDS);
MeasNewRefLine(left_wall_position, 0, left_wall_position, 2000);
ImgSetCurrent(I_IMAGE2, R_Def, ALL_BANDS);

for(j=2;j<=2000;j=j+20)
{
      // to find an edge on the left hand side and allocate a point and/or line marker
based on this edge (note:set width of search box to 1 pixel)

MeasSetEdgeStripeAngle(MEAS_NEAREST_NEIGHBOR, 360, 360, 5, 5);
MeasNewEdgeEx(90, MEAS_POL_AUTO, left_wall_position+40, j, 1,
search_box_height, left_wall_position+50, j+0.5, MEAS_MARKER_POS,
MEAS_ANY, MEAS_ANY);

        x2_position=MeasGetResult(MeasGetLastID(),MEAS_X1);
        userdll.LogInteger(j,0);                  // Write the j position to a file.
        userdll.LogString("  ",0);                // Write a space between j and x2 positions
        userdll.LogFloat(x2_position,1);          // Write the x2 position to a file.

ImgSetCurrent(I_DSC_0691, R_Def, ALL_BANDS);
MeasNewRefPoint(x2_position,j);
ImgSetCurrent(I_IMAGE2, R_Def, ALL_BANDS);

}
```

Note: The threshold values used to create a binarized image at five different Reynolds numbers are given below.

Table A.1: Threshold values at different Reynolds numbers

Reynolds number	Threshold
974	50
2111	50
3337	50
4552	30
5924	25